

DISS. ETH NO. 19103

**Novel States in Magnetic Materials under Extreme  
Conditions: A High Pressure Neutron Scattering Study of the  
Shastry-Sutherland compound  $\text{SrCu}_2(\text{BO}_3)_2$**

A dissertation submitted to

ETH ZURICH

for the degree of

Doctor of Sciences

presented by

MOHAMED ZAYED

Dipl. Ing. Phys. EPFL

born 22.06.1974

citizen of Bern (BE)

accepted on the recommendation of

Prof. Dr. M. Sigrist, examiner

Prof. Dr. H. M. Rønnow, co-examiner

Dr. Ch. Rüegg, co-examiner

Prof. Dr. J. Mesot, co-examiner

2010



# Contents

<b>Abstract</b>	<b>v</b>
<b>Résumé français</b>	<b>vii</b>
<b>1 Introduction</b>	<b>1</b>
1.1 Quantum magnetism and frustrated magnetism . . . . .	1
<b>2 Models and materials</b>	<b>5</b>
2.1 Models . . . . .	5
2.1.1 The Shastry-Sutherland Model . . . . .	6
2.2 Materials . . . . .	13
2.2.1 $\text{SrCu}_2(\text{BO}_3)_2$ . . . . .	13
2.2.2 Other Shastry-Sutherland compounds . . . . .	17
<b>3 Methods</b>	<b>19</b>
3.1 Neutron scattering . . . . .	19
3.1.1 Neutron scattering cross section . . . . .	21
3.1.2 Neutron scattering instruments . . . . .	28
3.2 High pressure in neutron scattering . . . . .	31
<b>4 Unusual temperature damping in <math>\text{SrCu}_2(\text{BO}_3)_2</math></b>	<b>39</b>

4.1	Time of flight measurements on $\text{SrCu}_2(\text{BO}_3)_2$ powder . . . . .	39
4.2	Damped Harmonic oscillator . . . . .	42
4.3	High field triple axis measurements on single crystals . . . . .	44
4.4	Triple axis measurements at zero field . . . . .	48
4.5	A phenomenological model for the temperature damping . . . . .	53
4.6	Conclusion on the temperature dependence of $\text{SrCu}_2(\text{BO}_3)_2$ . . . . .	56
<b>5</b>	<b>Pressure induced quantum phases in <math>\text{SrCu}_2(\text{BO}_3)_2</math></b>	<b>59</b>
5.1	Previous experimental and theoretical results . . . . .	60
5.2	Magnetic susceptibility up to 10 kbar. . . . .	61
5.3	Inelastic neutron scattering up to 22 kbar . . . . .	63
5.4	Identification of the new phase . . . . .	73
5.5	Neutron and X-ray diffraction . . . . .	75
5.6	Conclusion on the pressure induced quantum phases in $\text{SrCu}_2(\text{BO}_3)_2$ . . .	77
<b>6</b>	<b>Crystallographic study of <math>\text{SrCu}_2(\text{BO}_3)_2</math></b>	<b>81</b>
6.1	Temperature dependance of the crystal lattice . . . . .	81
6.2	High pressure crystal structure . . . . .	85
6.3	Conclusion on the crystallographic study . . . . .	91
<b>7</b>	<b>Conclusion and Outlook</b>	<b>93</b>
<b>A</b>	<b>The isolated dimer model</b>	<b>95</b>
<b>B</b>	<b>Four spins plaquette</b>	<b>101</b>
	<b>Acknowledgement</b>	<b>109</b>
	<b>Curriculum Vitae</b>	<b>119</b>

# Abstract

This thesis is at the crossing point of different fields: Quantum Magnetism which studies the collective properties of low spin systems, Neutron Scattering a powerful technique that enables to probe the microscopic properties of matter, and High Pressure where the use of ultra hard materials allows discoveries in a previously unexplored range. Combining these, we shall search for novel states in magnetic materials under extreme conditions. The extreme conditions are the quantum spin  $s=1/2$ , the low dimensionality, the low temperatures, and the high pressures. The material is the Shastry-Sutherland compound  $\text{SrCu}_2(\text{BO}_3)_2$ , a model quantum magnet which has attracted considerable interest over the last decade.

Three main results will be presented:

- 1) An unusual temperature dependence observed in  $\text{SrCu}_2(\text{BO}_3)_2$  where the excitation spectrum measured by inelastic neutron scattering disappears into a flat continuum at surprisingly low temperatures. We will quantify the damping of the triplet excitations and give a microscopic picture which involves the simultaneous presence of two triplets in the same region for the decay to occur.
- 2) The tuning of  $\text{SrCu}_2(\text{BO}_3)_2$  out of its ‘exact dimer’ ground state by application of hydrostatic pressure to a new gapped phase, which we identify as a ‘plaquette’ singlet. This occurs around  $\sim 18$  kbar and brings a decisive experimental evidence to a long debated question concerning the existence and the nature of the ‘intermediary phase’ in the Shastry-Sutherland model. Increasing the pressure even further leads the compound to order antiferromagnetically at 40 kbar with a high Neel temperature  $T_N=118$  K.
- 3) The study of the crystal structure of  $\text{SrCu}_2(\text{BO}_3)_2$  as a function of pressure and tem-

perature. We will present the temperature dependence of the structure down to  $T=1.6$  K. It will be shown that the magnetic properties affect the structure upon entering the spin gap regime. The crystal structure will also be solved at 37 kbar and 66 kbar. At the higher pressure the compound is in a monoclinic phase that brings it beyond the original Shastry-Sutherland model.

Finally this thesis also provides a brief overview of the high pressure neutron scattering technique.

# Résumé français

Cette thèse se situe au croisement de différents domaines: le magnétisme quantique qui étudie les propriétés collectives de systèmes à petit spin, la diffusion de neutrons, une technique puissante qui permet de sonder les propriétés microscopiques de la matière et les hautes pressions par lesquelles, grâce à l'emploi de matériaux ultra durs, l'on peut accéder à des domaines encore inexplorés. En les combinant, nous allons rechercher de nouveaux états dans les matériaux magnétiques sous conditions extrêmes. Les conditions extrêmes sont le spin quantique  $s=1/2$ , la basse dimensionalité, les basses températures et les hautes pressions. Le composé étudié est  $\text{SrCu}_2(\text{BO}_3)_2$ , un modèle d'aimant quantique, réalisation du réseau de Shastry-Sutherland, qui a reçu un attrait considérable au cours de cette dernière décennie.

Les trois résultats principaux qui seront présentés sont:

1) Une dépendance en température inhabituelle du  $\text{SrCu}_2(\text{BO}_3)_2$  où l'excitation mesurée par diffusion inélastique de neutrons disparaît dans un continuum sans structure à des températures étonnamment basses. Nous allons quantifier l'amortissement des triplets et en donner une image microscopique qui implique la présence simultanée de deux triplets dans une même région pour que l'amortissement se produise.

2) Le 'tunning' des couplages magnétiques du  $\text{SrCu}_2(\text{BO}_3)_2$  par l'application de pression hydrostatique. L'état fondamental de dimer 'exact' est perdu aux alentours de  $\sim 18$  kbar au profit d'une nouvelle phase que nous identifions comme un état singulet sur une plaquette. Ce résultat apporte une contribution décisive à la question longuement débattue de l'existence et de la nature d'une phase intermédiaire dans le modèle de Shastry-Sutherland. À plus haute pression, 40 kbar, le système entre finalement dans une phase d'ordre antiferromagnétique avec une haute température de Néel  $T_N=118$  K.

3) L'étude de la structure cristalline du  $\text{SrCu}_2(\text{BO}_3)_2$  en fonction de la pression et de la température. Nous présentons la dépendance en température de la structure jusqu'à  $T=1.6$  K. Les propriétés magnétiques affectent la structure dans le régime du gap de spin. La structure cristalline est également résolue à 37 kbar and 66 kbar. À 66 kbar le système est dans une phase monoclinique qui ne peut plus être décrite par le modèle de Shastry-Sutherland.

Finallement cette thèse présentera également une introduction à la technique de diffusion de neutron sous haute pression.



# Chapter 1

## Introduction

### 1.1 Quantum magnetism and frustrated magnetism

Magnetism in condensed matter is the manifestation of the interaction of electronic and nuclear magnetic moments in bulk solid and liquid materials. Magnetism originating from the nucleus leads to effects orders of magnitude smaller than its electronic counterpart, and is usually studied at ultra low temperatures or by resonant techniques such as Nuclear Magnetic Resonance. Electronic moments have two origins: the intrinsic spin and the orbital angular momentum of the charged particle. Often, the orbital moments are quenched due to crystal fields or can be combined with the intrinsic spin to form a total spin angular momentum.

Magnetism in condensed matter studies these *interacting spin systems*. The spins influence each other, not so much through a direct magnetic interaction, but through the electrostatic repulsion of electrons combined with the quantum mechanical requirements, in particular the Pauli exclusion principle. As a result, the interacting spins arrange themselves to minimize the energy in simple or complex patterns, ranging from ferromagnets, antiferromagnets, helices with uncommensurate order, disordered singlets, to more exotic crystal and resonating valence bond states. The quantum mechanical effects are enhanced for small values of the spin, the archetype of quantum magnetism being the *spin  $s = 1/2$  systems*. In real materials the spin  $s = 1/2$  systems are often realized in crystals containing  $\text{Cu}^{2+}$  ions connected through oxygen. The  $\text{Cu}^{2+}$  carries the  $s = 1/2$  spin from

its  $3d^9$  electronic configuration, and the oxygen orbitals provide the paths for the  $\text{Cu}^{2+}$  ions to interact with each other; this is known as indirect exchange interaction. These copper oxides are also the fundamental units in high temperature superconductor (HTC cuprates). Some less frequent realization of  $s = 1/2$  quantum magnets are obtained with  $\text{Ti}^{3+}$  or  $\text{V}^{4+}$  ions.

Additional interesting effects are obtained when reducing the dimensionality of the quantum magnet by synthesizing materials in which the magnetic ions form well isolated planes (2D magnets), chains (1D magnets) or ladders ('between' 1D and 2D). As hinted by the Mermin-Wagner theorem, thermal fluctuations in lower dimensions will prevent long range ordering and favor disordered arrangement. Very generally speaking, 1D systems will tend to have no magnetic long range order (LRO) even at  $T=0$  K while in 3D systems, LRO is often achieved at finite temperature. For 2D, the existence of LRO is strongly dependent on the details of the lattice and the relative values of the interactions. The calculation of the ground state energy, and of the excitation spectrum as well as the understanding of the role of quantum fluctuations remain quite challenging. The  $s = 1/2$  square lattice, for instance, is strongly believed to exhibit an antiferromagnetic ground state but the order parameter, the staggered magnetization, is reduced by about 40% compared to the classical case [1].

The situation described above is further complicated when the individual requirements for the magnetic couplings, as having the spins parallel or anti-parallel for ferromagnetic or antiferromagnetic interactions, cannot be simultaneously satisfied on a given lattice geometry. The system is then said to exhibit frustration. One very simple example involves three classical Ising spins on the corners of a triangle interacting antiferromagnetically so that the elementary interaction tends to bring them anti-parallel to each other. At least one of the bonds cannot be anti-parallel and is therefore frustrated, not satisfying the local magnetic constraint. From the 8 possible spin configurations, 6 have the minimal energy<sup>1</sup> and are thus ground states. The high ground state degeneracy, caused by the competition among the interactions, is an essential feature in the physics of frustrated magnetism. The Kagome lattice, where triangles share corners but not edges, so that

---

<sup>1</sup>They are two possibilities for the energies: all spins pointing in the same direction (2 cases) and one spin anti-parallel to the two others (6 cases).

fixing the orientation of the spin in one triangle doesn't fix it for the neighboring ones, has infinite<sup>2</sup> classical ground state degeneracy and is one of the most strongly frustrated simple geometries. The Shastry-Sutherland lattice is another example in which the existence of a diagonal next-nearest neighbor interaction causes the frustration. They are shown in Fig.1.1 together with unfrustrated topologies as the square lattice and the CaVO (modeling  $\text{CaV}_4\text{O}_9$ ). Frustration can also occur in 3D as for the pyrochlore lattice and in 1D only with next nearest neighbors interactions. It is also worth mentioning that the concept of geometrical frustration has not only been discussed in magnetism. For instance, it is used in relation to structural arrangements [2] where a definition given reads 'A local condition is unable to lead to a simple pattern for an extended system'.

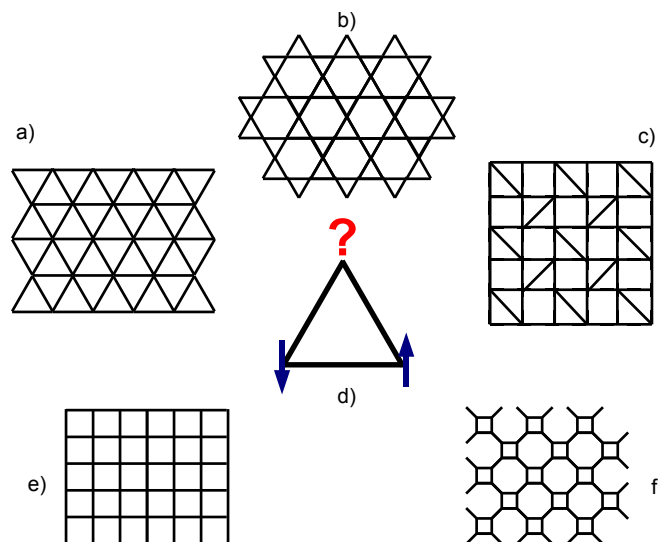


Figure 1.1: (a) Triangular, (b) Kagome, (c) Shastry-Sutherland lattices. (d) Frustrated interaction for three antiferromagnetically coupled spins on a triangle. (e) Square, (f) CaVO lattices. (a-c) are highly frustrated, while (e-f) are not.

The existence of frustration in a spin system very often leads to a different physics with some peculiar behavior as for instance, the 'order by disorder' phenomena [3]. Another unusual feature is the existence of 'algebraic order' where the correlation between the orientation of two spins does not decay exponentially with the distance as is normally the case in disordered systems, but decays much more slowly according to a power law. In frustrated systems, the role of quantum fluctuations is important and since the number

<sup>2</sup>i.e. the degeneracy increases exponentially with the number of sites.

of classical ground states is very large, it is often not possible to estimate or study the fluctuations around all of them. Unlike the case where there is a unique classical ground state, so that fluctuations may be expected to slightly modify it, the knowledge of the classical spin limit is often of no help for inferring quantum properties in frustrated systems. As a result, a wide range of interesting physics is displayed by frustrated quantum magnets and a large variety of exotic ground and excited states are found.

This thesis is devoted to the study of some particular aspects of quantum magnetism related to the frustrated  $s = 1/2$  Shastry-Sutherland model. We shall experimentally study the peculiar properties of  $\text{SrCu}_2(\text{BO}_3)_2$ , a physical realization of this model, as a function of temperature and pressure. We will describe its finite temperature behavior, the high pressure tuning across different quantum phases and the relationship between the structural and the magnetic properties.

The structure of the thesis is the following:

The next two chapters will first present the theoretical model and its physical realization (Chap. 2) as well as an introduction to the principal technics used for that research: neutron scattering and high pressure (Chap. 3). The experimental results will then be presented : the finite temperature properties of the frustrated Shastry-Sutherland compound  $\text{SrCu}_2(\text{BO}_3)_2$  (Chap. 4), The modification of the magnetic properties of  $\text{SrCu}_2(\text{BO}_3)_2$  through application of hydrostatic pressure (Chap. 5) and the relation between the atomic structure and the magnetic properties in  $\text{SrCu}_2(\text{BO}_3)_2$  as a function of temperature and pressure (Chap. 6).

# Chapter 2

## Models and materials

### 2.1 Models

The spin is understood as an intrinsic property of elementary particles, as is their mass or their electrical charge. It bears some resemblance to a rotation of the particle around its axis, hence the name ‘spin’. However the physical properties of the spin are peculiar and often counter intuitive. They can be described mathematically by an appropriate angular momentum quantum algebra. The spin is represented by a vectorial Hermitian operator  $\vec{S} = (S_x, S_y, S_z)$ . The three components of  $\vec{S}$  do not commute, but they do with  $S^2$ :

$$\begin{aligned} [S_x, S_y] &= i\hbar S_z \\ [S_y, S_z] &= i\hbar S_x \\ [S_z, S_x] &= i\hbar S_y \\ [S^2, S_j] &= 0, \quad j = x, y, z \end{aligned} \tag{2.1}$$

so that there exists a basis  $|s, m\rangle$  that diagonalizes  $S^2$  and one of the components, conventionally  $S_z$ , simultaneously.

$$\begin{aligned} S^2|s, m\rangle &= \hbar^2 s(s+1)|s, m\rangle \\ S_z|s, m\rangle &= \hbar m|s, m\rangle \end{aligned} \tag{2.2}$$

The two quantum numbers  $s$  and  $m$  are such that  $s$  is integer or half integer and  $m$  can range from  $-s$  to  $s$  in unit steps.  $s$  is fixed by the nature of the particle bearing the spin, half integer for Fermions and integer for Bosons or by the rules of spin addition in the case of composite particles.  $m$  gives the length of the spin component along a particular axis, and it can vary to minimize the energy for a given situation. For instance electrons have  $s = 1/2$  and  $m = (-1/2 \text{ or } +1/2)$ , the corresponding states  $|1/2, \pm 1/2\rangle$  are then symbolically represented by  $|\uparrow\rangle$  and  $|\downarrow\rangle$ , i.e. ‘spin up’ and ‘spin down’ respectively. When filling electronic shells in atoms ‘spin up’ and ‘spin down’ states will alternate so that electrons can stay on the same lower energy orbital without violating Pauli’s exclusion principle, and, in antiferromagnets, ‘spin up’ and ‘spin down’ states may alternate to minimize the total energy as is the case on the square lattice. Finally the length of the spin  $\|\vec{S}\| = \sqrt{S^2} = \hbar\sqrt{s(s+1)}$  is always different from  $\hbar s$  the maximal length along one axis because of the quantum fluctuations arising from the uncertainty principle. The relative difference is maximal in the  $s = 1/2$  case. As the spin is quantized in units of the reduced Planck’s constant  $\hbar$ , it will be more convenient for most of the following to use a unit system such that  $\hbar=1$ .

### 2.1.1 The Shastry-Sutherland Model

One basic model used in quantum magnetism is the Heisenberg model. In this model spins are treated as three dimensional objects obeying the quantum mechanical rules for angular momenta briefly summarized above and they couple to each other by exchange interactions labeled  $J$ . Usually the couplings are strong only among close enough spins<sup>1</sup> and calculations are restricted to nearest neighbors (nn) and next nearest neighbors (nnn). For two interacting spins indexed by  $i$  and  $j$  the interaction energy is given by the product of two spin operators  $\vec{S}_i\vec{S}_j$  and scales with the strength of the coupling  $J_{ij}$ . The Heisenberg model generalizes this to an arbitrary number of spins:

$$H = \sum_{i,j} J_{ij} \vec{S}_i \vec{S}_j \quad (2.3)$$

---

<sup>1</sup>The extension of electronic orbitals decays exponentially at long distances.

where  $H$  is known as the Heisenberg hamiltonian. Variants of the model are obtained by reducing the dimensionality of the lattice where the moments are placed, the dimensionality of the spins them self or by introducing anisotropies that will energetically favor some spin orientations. Finding an exact solution for a given configuration is far from trivial considering typical system sizes  $N$  of  $\sim 10^{23}$  spins and a Hilbert space dimension of  $(2s+1)^N$ . Numerical approaches also have limitations – although powerful techniques have been developed – especially in the case of frustrated systems where so called Monte-Carlo algorithms fail. Exact diagonalization allows to treat about  $\sim 20$  spins and diagonalization with Lanczos algorithms<sup>2</sup> taking only low energy levels into account, allows up to about 40 spins.

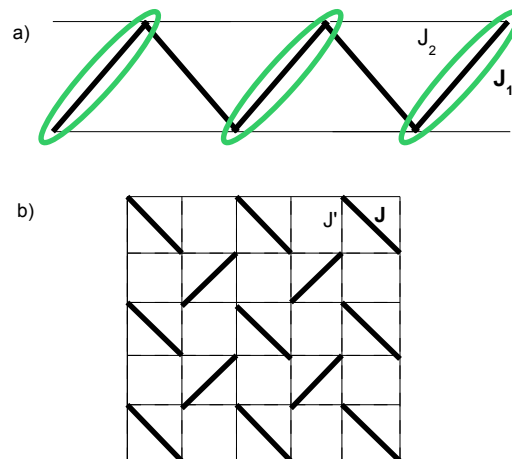


Figure 2.1: (a) A  $J_1$ - $J_2$  zigzag chain topologically equivalent to the Majumdar-Ghosh model when  $J_1=2J_2$ . The green ellipse indicates one of the two possible singlet ground states, the other one being obtained by forming the singlet on the remaining  $J_1$  bonds. (b) The Shastry-Sutherland lattice with intra-dimer coupling  $J$  (bold line) and frustrated inter-dimer coupling  $J'$  (thin line). For  $J'/J \leq \sim 0.7$  the ground state is obtained when forming singlets on all diagonal bonds.

They are a few cases however where it is possible to calculate at least the ground state exactly. An early example was pointed out by Majumdar and Ghosh [4] in 1D for a

<sup>2</sup>These take into account the sparse nature of the Hamiltonian matrix, to search for extreme eigenvalues.

spin chain connected by  $J_1$  (nn) and  $J_2$  (nnn) interactions. When  $J_2/J_1 = 0.5$  the ground state is a valence bond crystal, a product of singlets breaking the translational symmetry of the lattice. Shastry and Sutherland [5] with the model bearing their name gave another example<sup>3</sup> in 2D. The particular features of that model combined with the existence of a physical realization,  $\text{SrCu}_2(\text{BO}_3)_2$ , have since triggered considerable research efforts from both theorists and experimentalists. The Majumdar-Gosh and Shastry-Sutherland lattices are displayed in Fig.2.1.

$$H = J \sum_{nn} \vec{S}_i \vec{S}_j + J' \sum_{nnn} \vec{S}_i \vec{S}_j \quad (2.4)$$

Starting from  $s = 1/2$  spins sitting on a square lattice and adding diagonal bonds as indicated on Fig.2.1 b, one obtains the Shastry-Sutherland lattice, an orthogonal network of dimers connected by nn intra-dimer coupling  $J$  and nnn dimer-dimer coupling<sup>4</sup>  $J'$  described by the Hamiltonian in Eq.2.4. The nnn couplings induce the frustration. A product of singlets on the dimers (Eq.2.5) is always an eigenstate. The nnn couplings connect a spin to both ends of a dimer, and the matrix elements corresponding to nnn cancel out in the Hamiltonian. Shastry and Sutherland have further shown that for coupling ratios up to  $\alpha \equiv J'/J = 0.5$  this eigenstate is actually the ground state.

$$|\Psi\rangle = \prod \frac{1}{\sqrt{2}} (|\uparrow\downarrow\rangle - |\downarrow\uparrow\rangle) \quad (2.5)$$

Beyond  $\alpha = 0.5$ , the ground state cannot be obtained analytically, but numerical calculations have shown that the singlet product remains the ground state up to  $\alpha \leq \sim 0.7$  [7]. Antiferromagnetic (AFM) order is expected at large  $\alpha$  since the Shastry-Sutherland lattice then tends to the square lattice. Numerical calculations indeed showed AFM ordering already for  $\sim 0.9 \leq \alpha$ . The exact value of the transition points are subject to some variation in literature, and the nature of the phase for  $\sim 0.7 \leq \alpha \leq \sim 0.9$  known

---

<sup>3</sup>One important difference between the Majumdar-Gosh and the Shastry-Sutherland models is that the first one has a degenerate ground state breaking the translational symmetry, while the Shastry-Sutherland model has a unique ground state that does not brake the translational symmetry.

<sup>4</sup>In the original Shastry-Sutherland model the nn and nnn are reverted, we use here J for the intra-dimer coupling, regardless of the distance.



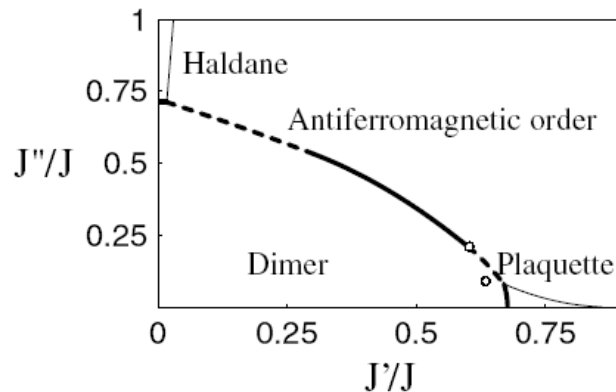


Figure 2.2: Proposed phased diagram for the Shastry-Sutherland model with inter-layer coupling  $J''$ . The circles are estimated couplings for  $\text{SrCu}_2(\text{BO}_3)_2$ . Reproduced from [6]

as the *intermediary phase* has lead to some debate among theorists. The main propositions — helical order, resonating valence bond plaquette, crystal valence bond plaquette, columnar dimer state, and no intermediary phase at all thus a direct transition from the singlet ground state to the AFM order — are summarized in Table 2.1 together with the corresponding calculation technique and the critical  $\alpha$  values. A pictorial representation of some proposed intermediary phases is shown in Fig.2.3. Some of these results will be discussed in more details in Chap. 5 in relation to the pressure tuning of  $\text{SrCu}_2(\text{BO}_3)_2$  across the Shastry-Sutherland phase diagram. It is also worth noting that for small values of the 3D interlayer couplings  $J''$ , the 2D results discussed above still hold. A possible phase diagram is shown in Fig.2.2.

Beside the existence of a possible intermediary phase, the Shastry-Sutherland model displays other interesting and sometimes unique properties:

- 1) Existence of a spin gap to very localized triplet excitations. The quasi-dispersionless nature of the excitations is unusual for extended systems. It is a consequence of the frustration that prevents triplets from hopping around once created, except through processes starting only at the sixth order in perturbation theory [7].
- 2) Correlated hopping: as the one-particle hopping is strongly suppressed by frustration, two-particle hopping plays an unusually important role on the Shastry-Sutherland lattice, in particular it is used to describe the properties of the bound triplet excitations. We

Main method	$\alpha_{c1}$	$\alpha_{c2}$	Intermediate phase
Variational method [5]	0.5	-	-
Schwinger boson mean field [8]	0.6	0.9	Helical order
Exact diagonalization (20 sites) [9]	0.70(1)	-	-
Ising expansion [10]	0.691(6)	-	-
Dimer expansion [11]	0.697(2)	-	-
Plaquette expansion [12]	0.677(2)	0.86	Plaquette singlet
Series expansion [13]	0.69	0.83 or -	Columnar or -
Exact diagonalization (32 sites) [14]	0.67	$\geq 0.71$	Plaquette singlet

Table 2.1: Summary of theoretical results for the intermediary phase, with transition points  $\alpha_{c1}$  (dimer-intermediary) and  $\alpha_{c2}$  (intermediary-AFM). Adapted from [7].

actually discovered that the softening of the bound-state upon application of hydrostatic pressure may be at the origin of the formation of the intermediary phase in  $\text{SrCu}_2(\text{BO}_3)_2$ , and that the presence of two triplets in the vicinity of each other plays an important role in the finite temperature properties of  $\text{SrCu}_2(\text{BO}_3)_2$ .

3) Magnetization plateaus: one of the most remarkable properties of the Shastry-Sutherland model is the existence of magnetization plateaus caused by the crystallization of triplets at certain fractional values of the saturation magnetization. These plateaus have indeed been observed in the real material  $\text{SrCu}_2(\text{BO}_3)_2$ , except for the 1/2 plateau that requires too large magnetic field. They are shown in Fig.2.4 together with possible associated triplet superstructures. They constitute the first evidence of ground states breaking the original Hamiltonian symmetry. The understanding of the physics of magnetization plateaus is an important ongoing theoretical and experimental research topic [15, 16].

4) Supersolid and superfluid phases: considering the triplets and the  $m=1$  two-triplet bound states as bosonic particles, the existence of superfluid phases at non-plateau magnetization has been proposed [18, 19]. Furthermore these phases may coexist with the crystalline triplet ordering in the vicinity of the magnetization plateaus and thus form a supersolid state: one fraction of the triplets stays localized on a superlattice while the rest condense into a superfluid.

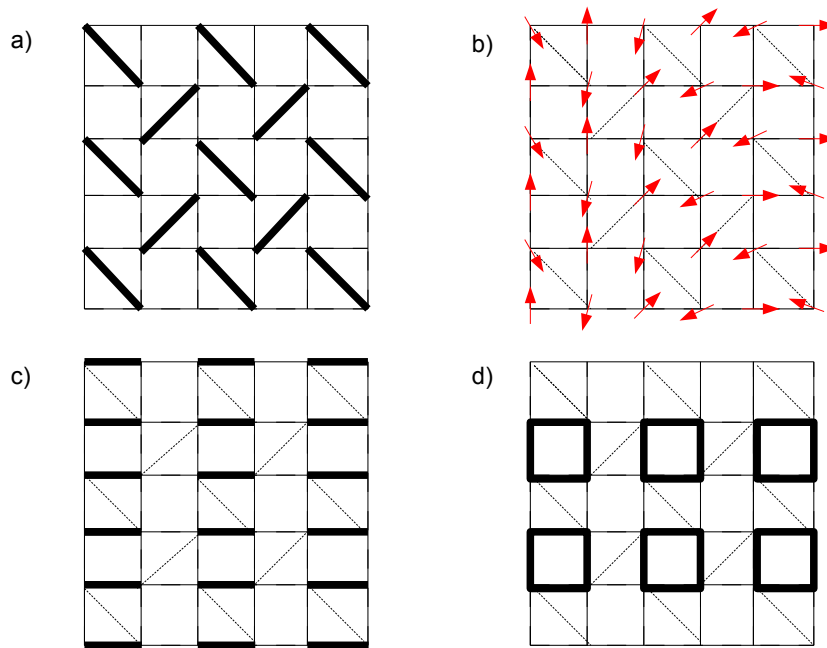


Figure 2.3: Pictorial representation of proposed intermediary phases for the Shastry-Sutherland model. (a) Dimer singlets. (b) Helical order [8]. (c) Columnar dimers [13]. (d) One of the two degenerate ground states for a plaquette valence bond crystal [14]. The thick lines connect the spins involved in the dimer or quadrumer singlets.

5) Superconductivity upon doping: several studies find a rich phase diagram for the Shastry-Sutherland model upon doping, including different superconducting phases [20, 21, 22].

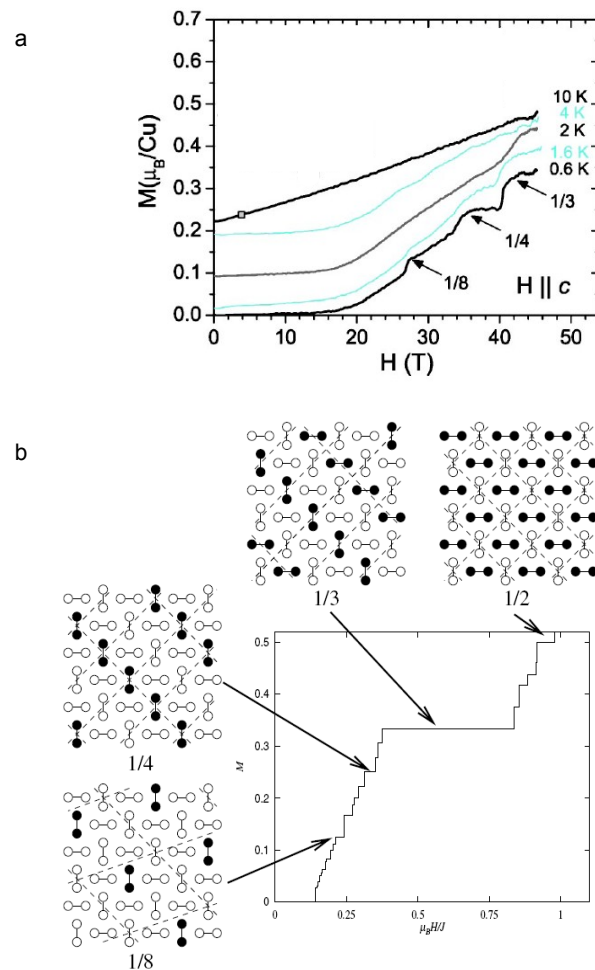


Figure 2.4: Magnetization plateaus. (a) Experimental observation of magnetization plateaus as function of temperature. Reproduced from [17]. (b) Numerical calculation of the magnetization curve using an effective hard-core boson model, and possible triplets (full bonds) superstructures. Reproduced from [7].

## 2.2 Materials

### 2.2.1 $\text{SrCu}_2(\text{BO}_3)_2$



Figure 2.5: Single crystal of  $\text{SrCu}_2(\text{BO}_3)_2$  grown by traveling solvent floating zone technique at PSI. The single crystalline part at the top of growth (right on the figure) is several centimeters long. For neutron scattering studies natural boron was replaced by the  $^{11}\text{B}$  isotope.

#### Crystal structure

Some 20 years after the theoretical model by Shastry and Sutherland it was discovered [23] that a previously synthesized material [24]  $\text{SrCu}_2(\text{BO}_3)_2$  is a topological realization of the model (Fig.2.6). At ambient conditions  $\text{SrCu}_2(\text{BO}_3)_2$  crystalizes in the tetragonal space group  $I\bar{4}2m$  with lattice constants  $a = b = 8.99 \text{ \AA}$ ,  $c = 6.45 \text{ \AA}$ . Each  $\text{Cu}^{2+}$  is connected to its unique  $\text{Cu}^{2+}$  nearest neighbor by two oxygens and to its four next nearest neighbors by planar  $\text{BO}_3$  groups. The nn distance is  $\sim 2.9 \text{ \AA}$  and nnn distance  $\sim 5.1 \text{ \AA}$ . The nn  $\text{Cu}^{2+}$  form a structural and magnetic dimer unit and the dimers themselves form an orthogonal network. The slightly buckled magnetic plane containing the  $\text{Cu}^{2+}$  ions is normal to the crystallographic  $[001]$  direction. These magnetic planes are well isolated from each other by intercalated Sr layers. The dimers are oriented along  $[110]$  and  $[-110]$ . Each dimer sits in a mirror plane that passes through to center of its orthogonal neighbor. Cu, B, and one O are on special positions and have eight equivalents in the

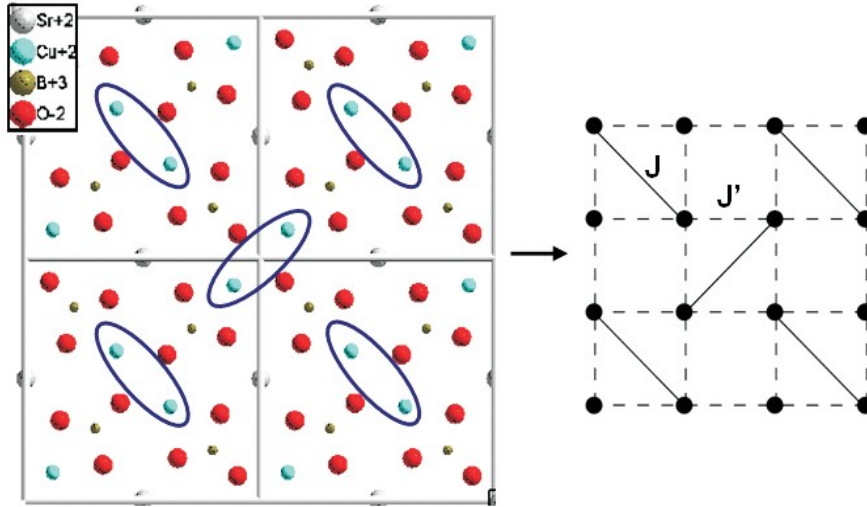


Figure 2.6: Left: view of the magnetic plane of  $\text{SrCu}_2(\text{BO}_3)_2$ . Right: topologically corresponding lattice of the Shastry-Sutherland model.

body centered conventional cell. Sr is on a higher symmetry position and has only four equivalents, while the other O is on a general position with the maximal multiplicity of sixteen. The conventional unit cell thus contains four dimers on two different layers, with alternating orientations (Fig.2.7). As temperature is raised above ambient, Sparta et al. [25] discovered a structural transition at  $T=395$  K to a higher symmetry phase with tetragonal space group  $I4/mcm$  where the buckling disappears and the magnetic plane becomes a mirror plane. No phase transitions have been detected upon cooling to low temperature, but our work (Chap. 6) and the work of others [26, 27] show notable structural changes (lattice constant, nn distance, thermal expansion coefficient, Cu-O-Cu angles, etc) that are likely to be related to spin gap regime below 35 K, all these however not changing the  $I\bar{4}2m$  symmetry in a noticeable manner. At high pressure and ambient temperature Loa et al. [28] discovered a transition to a monoclinic phase at 47 kbar and to another unidentified phase at 150 kbar. We extended these results with combined low temperature and high pressure measurements to obtain a complete P-T phase diagram, showing structural and magnetic transitions (see Chap. 5 and 6).

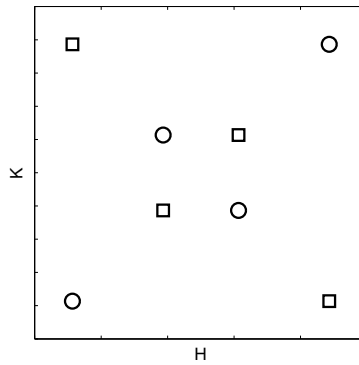


Figure 2.7: Projected view of the Cu positions in the unit cell. There are two different magnetic Cu layers represented by circles and squares. The lower layer (circle) has a height in the  $c$ -direction of  $\sim 0.25$  and the upper layer (square) of  $\sim 0.75$ .

### Relation with the Shastry-Sutherland model and magnetic properties

As seen from the crystal structure, the  $s = 1/2$   $\text{Cu}^{2+}$  ions form an orthogonal dimer network that can be mapped topologically to the Shastry-Sutherland model. In the real material small interlayer couplings are present. However this does not influence the exactness of the singlet ground state [6, 7]. It is therefore correct to assume that to a large extent the magnetic properties of  $\text{SrCu}_2(\text{BO}_3)_2$  are well described by the Shastry-Sutherland model. Early susceptibility measurements showed a gapped behavior and a non-magnetic ground state [29, 23]. The compound was latter investigated by numerous experimental techniques including ESR [30, 31, 32], INS [33, 34, 35],  $\mu\text{Sr}$  [36, 37], specific heat [38, 17], sound wave measurements [39, 40], Raman spectroscopy [41, 42, 28], NMR [43, 15, 44], (see Ref.[45] for an experimental review). The singlet ground state is separated from an excited triplet state by a 35 K (3 meV) gap. This triplet state exhibits the unusual property of being almost dispersionless, which is understood in terms of the frustration in the Shastry-Sutherland model that prevents triplets from hopping. The frustration leads the strongly correlated network of  $s = 1/2$  ions to behave in a first approximation as isolated dimers. However, the isolated dimer model while a good starting point to estimate properties of  $\text{SrCu}_2(\text{BO}_3)_2$ , cannot explain most of its interesting features which originate from the strong interaction between the dimers. A precise modeling of  $\text{SrCu}_2(\text{BO}_3)_2$

has to take into account not only the  $J''$  interlayer coupling<sup>5</sup> but also the anisotropic Dzyaloshinskii-Moriya (DM) interactions that are needed to explain high-resolution measurements [46, 47]. The triplet gapped excitation observed by high resolution INS is actually split into three components separated by about 0.2 meV and having different Q-dependent intensities [34, 35]. ESR – which intrinsically is a high resolution technique compared to INS – shows two distinct excitations due to different selection rules [7, 46]. This Q-dependent DM splitting is thus the main source for the small dispersion observed in lower resolution INS experiments. Among higher energy states, a two-triplet bound state is observed at  $\sim 5$  meV. The two triplets, by binding together, manage to reduce their total energy by about 1 meV. Similarly the  $\sim 9$  meV excitation observed by INS, has been described as a multi-triplet excitation [7, 33]. The value of coupling parameters in  $\text{SrCu}_2(\text{BO}_3)_2$  has been subject to some variation in the literature, the dispersionless nature of the gap preventing simple fitting of the INS dispersion curve. Miyahara and Ueda [7] proposed  $J=84$  K,  $J'=54$  K,  $J''=8$  K ( $J'/J=0.635$ ,  $J''/J=0.09$ ) as the optimal set of parameters from fits to the susceptibility.

A major interest in the magnetic properties of  $\text{SrCu}_2(\text{BO}_3)_2$  comes from the magnetization plateaus observed at fractional values of the saturation magnetization (Fig.2.4). These commensurate states arise from the reduction of the triplets kinetic energy due to the peculiar frustrated orthogonal geometry. More than ten years after the discovery, the full understanding of the magnetization process of  $\text{SrCu}_2(\text{BO}_3)_2$  is still a hot topic. The challenging experimental conditions, requiring a combination of high fields and sub-kelvin temperatures, make the lowest plateau ( $1/8$  at 28 T) the most studied while the predicted  $1/2$  plateau has not been observed yet due to the field above 70 T needed. The existence of a spin-gap, the unusual nature of the excitations, the mapping to the Shastry-Sutherland model and the magnetization plateaus have made this compound a model quantum magnet for experimental and theoretical studies.

---

<sup>5</sup>Strictly speaking the symmetry would imply two non-equivalent major interlayer couplings due to the buckling of the magnetic plane, however this is unimportant for the magnetic properties [7].



### 2.2.2 Other Shastry-Sutherland compounds

$\text{SrCu}_2(\text{BO}_3)_2$  is the only known realization of the Shastry-Sutherland model with a real  $s = 1/2$  spin. However, there are other materials whose magnetic ions can be mapped to the Shastry-Sutherland network:  $\text{RB}_4$ ,  $\text{R}_2\text{BaPdO}_5$  [48] (R=rare earth),  $\text{Nd}_2\text{BaZnO}_5$  [49],  $\text{Yb}_2\text{Pt}_2\text{Pb}$  [50]. Most of these order antiferromagnetically at low temperature, the choice of the R ion being important as is usually the case in rare earth magnetism. Helical structures are suggested for  $\text{TbB}_4$  [51] and  $\text{GaB}_4$  [52].  $\text{RB}_4$  with R=Tb [51], Dy [53], Er [54], Tm [55] also exhibit plateaus in their magnetization curves [56] as is the case for  $\text{SrCu}_2(\text{BO}_3)_2$ . On the other hand there are notable differences:  $\text{RB}_4$  compounds are good metals while  $\text{SrCu}_2(\text{BO}_3)_2$  is an insulator. The 3d transition metal and 4f rare earth magnetism also involve different hierarchies in the strength of spin-orbit and crystal fields, so that one should remain careful when drawing parallels to  $\text{SrCu}_2(\text{BO}_3)_2$ , and these materials constitute a subject of study by their own right.



# Chapter 3

## Methods

### 3.1 Neutron scattering

Neutron scattering is one of the most powerful techniques available for the study of condensed matter in particular for the study of magnetism. It enables to probe the microscopic properties of materials, as opposed to the macroscopic ones measured by more common techniques as magnetic susceptibility, magnetization, and specific heat to cite a few. On the other hand unlike the previous, neutron scattering requires large facilities, not routinely available at universities or institutes, which implies obtaining measurement time (beam time) through proposals where the scientific objectives and technical feasibility of the experiment are judged. The beam time demand largely exceeding the facilities capacity (overload factor of  $\sim 2$  to  $3$ ) it results in relatively long idle time between different experiments making the research quite different from home based research at university institutes. The neutron sources are essentially of two types: 1) nuclear reactors with compact core, where neutrons are produced through controlled fission of  $^{235}\text{U}$ , and 2) spallation sources, where an accelerated proton beam hits a heavy target producing an 'evaporation' of neutrons. Reactors usually produce steady flow of neutrons while spallation sources are pulsed<sup>1</sup>. The neutrons produced by the source initially have MeV energies and are slowed down by collisions in a moderator, such as heavy water, to a thermal (300 K, 26 meV) or cold (25 K, 2.2 meV) energy range useful for condensed matter studies. They are a

---

<sup>1</sup>SINQ the Swiss spallation source has the particularity of being quasi-continuous.

few dozens neutron scattering facilities world wide including important ones in western Europe such as ILL and LLB (France), FRM2 and HMI (Germany), SINQ (Switzerland) and ISIS (UK). The neutron scattering experiments for the work presented here have been performed at SINQ, ILL, and FRM2.

ILL with a 60 MW nuclear reactor produces a record flux of  $1.5 \cdot 10^{15}$  [57] neutrons per second and  $\text{cm}^2$  in the moderator. FRM2 and SINQ respectively produce  $8 \cdot 10^{14}$  and  $10^{14}$  neutrons  $\text{cm}^2 \text{s}^{-1}$  [58, 59]. The final flux at the sample depends on the nature of the source, the distance between the source and the instrument, the quality of the neutron guide, and finally the experimental conditions such as the choice of wavelength and filters. Cold triple axis instrument IN14 at ILL, for instance, has  $1.6 \cdot 10^7$  neutrons  $\text{cm}^2 \text{s}^{-1}$  at a wavelength  $\lambda = 4.04 \text{ \AA}$  [60] while the thermal triple axis IN8 has a flux of  $2 \cdot 10^8$  neutrons  $\text{cm}^2 \text{s}^{-1}$  at  $\lambda = 2.36 \text{ \AA}$  [61].

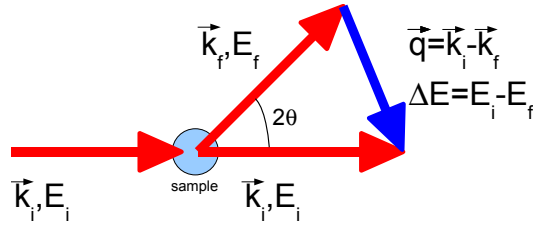


Figure 3.1: Definition of the scattering geometry: the incoming neutron with energy  $E_i$  and wave vector  $\vec{k}_i$  exits the sample after scattering at an angle  $2\theta$  with energy  $E_f$  and wave vector  $\vec{k}_f$ . The energy and wave vector transfer are given by  $\vec{Q}$  and  $\Delta E$ .

For magnetic studies results obtained by neutron scattering are often decisive for the characterization of the sample properties. For instance while bulk measurement can tell if a sample is metallic or insulating, magnetic or non-magnetic and assign it to more specific categories, information on the relevant magnetic interactions, the values of the couplings, the involved exchange paths, the orientation of the spins and the excitation spectrum above the ground state is more directly gained by neutron scattering experiments. As an example, in the case of  $\text{SrCu}_2(\text{BO}_3)_2$  bulk measurements combined with crystallographic information, indicated clearly an interesting non-magnetic insulator, with a gap from probably a singlet state to higher excited triplet levels. INS allows to measure directly the 35K gap (the value  $\sim 19 \text{ K}$  was underestimated by early susceptibility fits [23]), to discover the excitation spectrum is dispersionless and that there are multi-triplet bound

states at higher energy.

### 3.1.1 Neutron scattering cross section

The basic idea behind neutron scattering is the process represented in Fig.3.1. One neutron originating from the source (or monochromated to the desired energy  $E_i$ ) hits the target sample and is scattered in some direction defined by an angle  $2\theta$ . The measurement of that direction as well as the measurement of the final neutron energy provides all the information on the scattering process. The wave vector  $\vec{k}$ , momentum  $\vec{p}$ , mass  $m_n$ , velocity  $v$ , wavelength  $\lambda$ , frequency  $\nu$ , angular frequency  $\omega$  and conventional equivalent temperature  $T$  of the neutron are related to its energy  $E$  through the usual formulae that apply for massive particles:

$$E = h\nu = \hbar\omega = \frac{1}{2}m_nv^2 = \frac{p^2}{2m_n} = \frac{h^2}{\lambda^2} \frac{1}{2m_n} = \frac{\hbar^2 k^2}{2m_n} = k_b T \quad (3.1)$$

where  $k_b$ ,  $h$  and  $\hbar$  are the Boltzmann, Planck and reduced Planck constant ( $h/2\pi$ ) respectively. The formalism of neutron scattering has been treated in several books [62, 63, 64], its central item being the calculation of the different cross sections. The following gives a short description of the different types of scattering processes and the result for the corresponding cross section. Considering an incoming neutron flux at the sample  $\Psi$  given in number of neutrons per second per surface unit, where the surface is taken perpendicular to the neutron beam, the *scattering cross section* is defined by:

$$\sigma = \frac{N_s}{\Psi} \quad (3.2)$$

with  $N_s$  the number of neutrons scattered per second by the system.  $\sigma$  has units of area and is of the order of  $10^{-28}m^2 \equiv 1$  barn. The *differential cross section* is used to count neutrons scattered in a specific direction defined by a solid angle  $d\Omega$  originating from the sample:

$$\frac{d\sigma}{d\Omega} = \frac{N_s^{d\Omega}}{\Psi d\Omega} \quad (3.3)$$

where  $N_s^{d\Omega}$  is the number of neutrons scattered per second by the system into the solid angle  $d\Omega$ . Finally, the *the partial differential cross section* is the relevant quantity when the energy of the neutron is analyzed (we assume here constant initial energy  $E_i$  and variable final energy  $E_f$ ):

$$\frac{d^2\sigma}{d\Omega dE_f} = \frac{N_s^{d\Omega dE_f}}{\Psi d\Omega dE_f} \quad (3.4)$$

with  $N_s^{d\Omega dE_f}$  the number of neutrons scattered per second into the solid angle  $d\Omega$  with final energy between  $E_f$  and  $E_f + dE_f$ . These three quantities are related by

$$\sigma = \int \frac{d\sigma}{d\Omega} d\Omega = \iint \frac{d^2\sigma}{d\Omega dE_f} d\Omega dE_f. \quad (3.5)$$

Describing the interaction between the neutron and the sample by an operator  $\hat{U}$ , the differential cross section  $\frac{d\sigma}{d\Omega}$  can be derived from a basic quantum mechanical result, Fermi's golden rule, giving the probability of transition between an initial state  $|\Psi_i\rangle$  and a final state  $|\Psi_f\rangle$ :

$$\frac{d\sigma}{d\Omega} = \frac{k_f}{k_i} \left( \frac{m_n}{2\pi\hbar^2} \right)^2 |\langle \Psi_f | \hat{U} | \Psi_i \rangle|^2 \quad (3.6)$$

The partial differential cross section is obtained by multiplying the previous result by a Dirac function to account for energy conservation:

$$\frac{d^2\sigma}{d\Omega dE_f} = \frac{k_f}{k_i} \left( \frac{m_n}{2\pi\hbar^2} \right)^2 |\langle \Psi_f | \hat{U} | \Psi_i \rangle|^2 \cdot \delta(E + E_i - E_f) \quad (3.7)$$

There are two major types of interactions between the neutron and the sample: nuclear and magnetic. The operator  $\hat{U}$  will turn out to be approximated by a very simple expression for nuclear interactions, while it takes a more complicated form for magnetic interactions. There are also two major types of scattering processes to be distinguished: elastic and inelastic. The former provides information on the structure by measuring the angles at which neutrons are diffracted after collisions with the probe, the latter reveals the excitations by measurement of the energy the neutron has exchange with the sample.

The following four categories can thus be distinguished:

1) **Elastic nuclear scattering.** The neutron interacts with the nuclei of atoms on very short scales ( $\sim 10^{-5} \text{ \AA}$ ) through nuclear forces. The wavelength of thermal neutrons ( $\sim 2 \text{ \AA}$ ) being orders of magnitude larger than the interaction range, the individual scattering processes are essentially isotropic, so that the incoming neutron can be viewed as plane wave and the scattered neutron as a spherical wave with the scattering strength strongly isotope and nuclear-spin dependent. When these nuclei form a symmetric arrangement with interatomic distances comparable to the neutron's wavelength (which is usually the case) a coherent diffraction pattern (Bragg peaks) emerges from which the original structural configuration can be recomputed. The presence of different isotopes and nuclear spins additionally leads to an incoherent scattering that adds as a background to the coherent diffraction pattern. The main technique however to obtain structural information remains X-ray diffraction. While there are number of similarities with neutron diffraction, X-rays have some decisive advantages: very high flux, small beam size i.e. small sample can be used, and X-ray sources are more commonly available than neutron sources. On the other hand, the X-ray cross section increases as a function of the atomic number while the neutron cross section varies essentially 'randomly' among elements and isotopes. Neutrons thus become useful when it comes to detecting light elements, differentiate isotopes, and also for probing the inner part of a sample.

Given the very short range of nuclear interactions, the operator  $\hat{U}$  can be approximated by the Fermi pseudo-potential:

$$\hat{U}(\vec{r}) = \frac{2\pi\hbar^2}{m_n} \sum_j b_j \delta(\vec{r} - \vec{R}_j) \quad (3.8)$$

where  $\vec{r}$  is the spatial position at which the interaction is evaluated,  $\vec{R}_j$  the position of the  $j^{\text{th}}$  nucleus in the sample and  $b_j$  is known at the scattering length for this nucleus.  $b_j$  reflects the ability to scatter neutron for a particular isotope and its values have been experimentally measured for almost all elements and can easily be found in specialized

tables [65]. The spacial Dirac function ensures the nuclear interaction is only effective at the nuclei positions.

We now consider nuclei in a crystal so that they are spatially arranged on a regular lattice comprising  $N$  unit cells of volume  $V_0$  described by reciprocal lattice vectors  $\vec{\tau}$ . Equations 3.8 and 3.6 combine to give

$$\frac{d\sigma}{d\Omega} = \frac{N}{V_0} (2\pi)^3 e^{-2W} |F_N(\vec{Q})|^2 \sum_{\vec{\tau}} \delta(\vec{Q} - \vec{\tau}). \quad (3.9)$$

This is the fundamental equation for elastic neutron scattering. The Debye-Waller factor  $e^{-2W}$  accounts for small displacement of nuclei around their equilibrium position. Equation (3.9) contains the usual Bragg diffraction law<sup>2</sup>:  $n\lambda = 2d\sin(\theta)$  through the condition that the neutron's wave vector transfer  $\vec{Q}$  must equal a reciprocal lattice vector:  $\vec{Q} = \vec{\tau}$ . It further provides the intensity of each Bragg reflection through the structure factor  $F_N(\vec{Q})$ ,

$$F_N(\vec{Q}) = \sum_l b_l e^{i\vec{Q}\cdot\vec{d}_l} \quad (3.10)$$

where the sum is taken over one unit cell on all the nuclei at relative positions  $\vec{d}_l$ . In the neutron diffraction pattern, the position of the Bragg peaks ( $\vec{Q} = \vec{\tau}$ ) gives the information on the unit cell — the structural periodicity of the sample — while the relative intensities of these peaks (Eq.3.10) give the information on the position of the atoms inside the unit cell.

2) **Inelastic nuclear scattering.** Through the same type of interaction the neutron can also gain or loose energy in the sample. This energy comes from the absorption or creation of lattice excitations: *phonons*. The value of the mass of the neutron  $m_n$ , trough relations (3.1), makes this particle an excellent probe for collective low energies excitations of  $\sim$ meV order involving  $\sim$ Å distances. Thermal neutrons with energies  $\sim$ 20 meV comparable to phonon are thus commonly used to study the different lattice vibration modes and map their dispersion  $E(\vec{q})$ . Thanks to recent instrumentation progress, phonons can also be measured by inelastic X-ray scattering but then require very high relative resolution in

---

<sup>2</sup>Where  $d$  is the spacing between atomic planes and  $n$  an integer.



order to detect energy transfers of  $\sim 10$  meV when the initial X-ray energies are several keV.

The cross section for inelastic nuclear scattering can be developed into terms describing multiple phonon creation or annihilation processes. We only mention here the form taken by the coherent one-phonon cross section for atoms of mass  $M$  and scattering length  $b$ .

$$\begin{aligned} \frac{d^2\sigma}{d\Omega dE_f} &= \frac{k_f}{k_i} b^2 \left( \frac{4\pi^3}{V_0 M} \right) e^{-2W} \sum_{s,q} \frac{[\vec{Q} \cdot \vec{e}_s(\vec{q})]^2}{E_s(\vec{q})} \\ &\quad \{ (n_s + 1) \delta(E - E_s(\vec{q})) \sum_{\tau} \delta(\vec{Q} - \vec{q} - \vec{\tau}) + \\ &\quad n_s \delta(E + E_s(\vec{q})) \sum_{\tau} \delta(\vec{Q} + \vec{q} - \vec{\tau}) \} \end{aligned} \quad (3.11)$$

where  $\vec{e}_s$  is the polarization vector of the phonon with index  $s=(1,2,3)$ , and  $n_s$  the Bose factor reflecting the relative probabilities of creation and annihilation processes as function of temperature:

$$n_s = \frac{1}{e^{\frac{E_s(\vec{q})}{k_b T}} - 1}. \quad (3.12)$$

The second line in (3.11) represents the creation of a phonon and the third line its annihilation. At  $T=0$  K, only creation is possible as  $n_s = 0$ .

3) **Elastic magnetic scattering.** The neutron having a magnetic moment<sup>3</sup>  $\vec{\mu}_n$

$$\mu_n = -\gamma\mu_c = -9.66 \cdot 10^{-27} J/T, \quad \mu_b = 9.274 \cdot 10^{-24} J/T \quad (3.13)$$

where  $\mu_c$  is the nuclear magneton,  $\mu_b$  the Bohr magneton and  $\gamma = 1.913$  the gyromagnetic ratio of the neutron, it interacts with the magnetic moments of the nuclei and of the electron via dipole-dipole interaction. We consider here only the electronic case. The electron cloud extending to distances comparable to the neutron's wavelength, the scattering is no longer isotropic and a form factor has to be considered (Eq.3.16). In neutron experiments,

---

<sup>3</sup>The negative sign indicates that for the neutron the magnetic moment is antiparallel to the angular momentum, unlike the case of protons where they are parallel.

this reflects in intensity disappearing at large wave numbers  $Q$ . The electronic moments involved come from the unpaired electrons in the target sample. For instance,  $\text{Cu}^{2+}$  has  $3d^9$  electronic configuration missing one electron to form a full shell and is left with an unpaired spin  $s = 1/2$ . The magnetic moment is proportional to the spin with a proportionality factor  $g\mu_b$ , the precise value of  $g \simeq 2$  depending on the particular compound. Neutron elastic magnetic scattering provides then the information on the orientation of the moments and thus the magnetic structure of the material. Similar to nuclear Bragg peaks, magnetic Bragg peaks will be observed with intensities often comparable to the nuclear reflections. A typical example is given when a transition occurs upon cooling from a disordered magnetic phase to an ordered antiferromagnet. In many such cases the magnetic structure has a unit cell with double size compared to the structural unit cell. This will reflect in Bragg peaks suddenly appearing in the reflection pattern at positions forbidden by the structural symmetry.

The interaction potential for magnetic scattering between one neutron and one electron is given by

$$\hat{U} = -\hat{\boldsymbol{\mu}}_n \left[ \text{rot} \left( \frac{\hat{\boldsymbol{\mu}}_e \times \vec{R}}{R^3} \right) - \frac{e}{m_e c} \frac{\hat{\mathbf{p}}_e \times \vec{R}}{R^3} \right] \quad (3.14)$$

where  $\hat{\boldsymbol{\mu}}_n$  and  $\hat{\boldsymbol{\mu}}_e$ , are the operators associated to the magnetic moment of the neutron and of the electron respectively,  $\hat{\mathbf{p}}_e$  the momentum operator of the electron,  $m_e$  its mass and  $\vec{R}$  the distance between the neutron and the electron. The quantity inside the brackets in (3.14) represents the magnetic field produced by the electron at the neutron's position. The first term inside the bracket is the dipole-dipole interaction arising from the electron's spin, while the second term comes from the electron's orbital motion. In the following we neglect the orbital motion and consider 'spin-only' scattering. The magnetic moment operators for the neutron and the electron relate to the spin of these particles through:

$$\begin{aligned} \hat{\boldsymbol{\mu}}_n &= -\gamma\mu_c\hat{\sigma} \\ \hat{\boldsymbol{\mu}}_e &= -g\mu_b\vec{S} \end{aligned} \quad (3.15)$$

with  $\hat{\sigma}$  the Pauli operator for the neutron spin. The magnetic form factor  $f(\vec{Q})$  is given

by the Fourier transform of the normalized unpaired spin density  $\rho_s(\vec{r})$ :

$$f(\vec{Q}) = \int \rho_s(\vec{r}) e^{i\vec{Q}\cdot\vec{r}} d\vec{r}. \quad (3.16)$$

The elastic magnetic cross-section from a magnetically ordered material containing  $N_M$  magnetic unit cells of volume  $V_{0M}$  takes a form similar to (3.9):

$$\frac{d\sigma}{d\Omega} = \frac{N_M}{V_{0M}} (2\pi)^3 (\gamma r_0)^2 \left(\frac{g}{2} f(Q)\right)^2 e^{-2W} |F_M(\vec{Q})|^2 \sum_{\vec{\tau}_M} \delta(\vec{Q} - \vec{\tau}_M). \quad (3.17)$$

The sum is now taken over the reciprocal vectors  $\vec{\tau}_M$  of the magnetic unit cell and  $r_0$  is the classical electron radius. The magnetic Bragg reflections obey the condition  $\vec{Q} = \vec{\tau}_M$  and their relative intensities –apart from the form factor  $f(\vec{Q})$ – is given by the magnetic structure factor  $F_M(\vec{Q})$ :

$$F_M(\vec{Q}) = \sum_l S_{d_l}^\perp e^{i\vec{Q}\cdot\vec{d}_l}. \quad (3.18)$$

One important difference with elastic nuclear scattering is that neutrons can only probe the spin component  $S^\perp$  perpendicular to  $\vec{Q}$ .

4) **Inelastic magnetic scattering.** This is the magnetic counterpart to inelastic nuclear scattering. Not only the neutron can probe the static arrangement of the spins it can also probe their dynamics. In particular *magnons*, the magnetic analogue to phonons, are the collective excitations of the spin system. Inelastic magnetic scattering directly measures these as a function of energy and momentum. This technique is at the heart of the present thesis. The cross section is given by

$$\frac{d^2\sigma}{d\Omega dE_f} = (\gamma r_0)^2 \left(\frac{g}{2} f(\vec{Q})\right)^2 e^{-2W} \sum_{\alpha,\beta} \left(\delta_{\alpha,\beta} - \frac{Q_\alpha Q_\beta}{Q^2}\right) S^{\alpha,\beta}(\vec{Q}, E), \quad (3.19)$$

with the *dynamical structure factor*  $S(\vec{Q}, E)$  useful to express the cross section has been introduced:

$$S^{\alpha,\beta}(\vec{Q}, E) = \sum_{a,b} e^{i\vec{Q}\cdot(\vec{R}_a - \vec{R}_b)} \sum_{\lambda_i, \lambda_f} p(\lambda_i) \langle \lambda_i | S_a^\alpha | \lambda_f \rangle \langle \lambda_f | S_b^\beta | \lambda_i \rangle \delta(E + E_i - E_f). \quad (3.20)$$

a and b label the positions  $\vec{R}_a$  and  $\vec{R}_b$  of the spins  $S_a$  and  $S_b$ ,  $\alpha$  and  $\beta$  are the three spatial directions (x,y,z),  $\lambda_i$  and  $\lambda_f$  the initial and final states and  $p(\lambda_i)$  the occupation probability of the state  $\lambda_i$ .  $S(\vec{Q}, E = \hbar\omega)$  is related to the imaginary part of the magnetic susceptibility through the fluctuation dissipation theorem:

$$S(\vec{Q}, \omega) = \frac{1}{1 - e^{-\hbar\omega/k_bT}} \text{Im}\chi(\vec{Q}, \omega). \quad (3.21)$$

$\text{Im}\chi(\vec{Q}, \omega)$  itself is connected to the real part of the susceptibility by the Kramers-Kronig relations:

$$\text{Im}\chi(\vec{Q}, \omega) = -\frac{1}{\pi} P \int_{-\infty}^{\infty} \frac{\text{Re}\chi(\vec{Q}, \omega')}{\omega' - \omega} d\omega' = -\frac{2\omega}{\pi} P \int_0^{\infty} \frac{\text{Re}\chi(\vec{Q}, \omega')}{\omega'^2 - \omega^2} d\omega' \quad (3.22)$$

$$\text{Re}\chi(\vec{Q}, \omega) = \frac{1}{\pi} P \int_{-\infty}^{\infty} \frac{\text{Im}\chi(\vec{Q}, \omega')}{\omega' - \omega} d\omega' = \frac{2}{\pi} P \int_0^{\infty} \omega' \frac{\text{Im}\chi(\vec{Q}, \omega')}{\omega'^2 - \omega^2} d\omega' \quad (3.23)$$

where  $P$  is the principle part of the integral and the second equalities follow from  $\text{Im}\chi(\vec{Q}, \omega)$  and  $\text{Re}\chi(\vec{Q}, \omega)$  being odd and even functions respectively. Finally,  $S(Q, \omega)$  also satisfies the *detailed balance condition*:

$$S(-\vec{Q}, -\omega) = e^{-\hbar\omega/k_bT} S(\vec{Q}, \omega) = S(\vec{Q}, -\omega), \quad (3.24)$$

the last equality being realized only when an inversion symmetry is present.

### 3.1.2 Neutron scattering instruments

As seen in the previous section, the structural and magnetic excitations in a sample can directly be probed by neutrons. However, given that the detection of neutrons involves  $\sim$ MeV energies while the energy transfers with the sample are of the meV order, special strategies need to be implemented. The main two are: triple axis and time of flight

measurements, and both enable to measure the change in energy and momentum of the neutron.

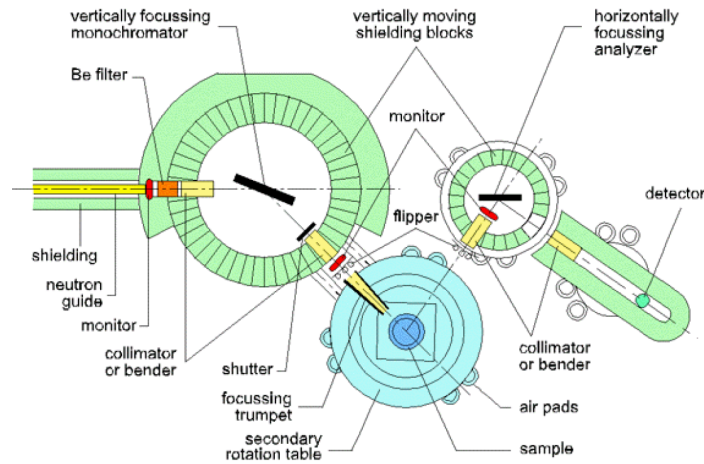


Figure 3.2: Schematic view of the triple axis instrument TASP at SINQ PSI. Reproduce from [59].

The name triple axis comes from the three axis of rotation the instrument possesses: monochomator, sample table and analyzer. From the neutron beam emitted by the source, the monochromator rotation selects the desired incoming wavelength, by Bragg reflections from a crystal<sup>4</sup>. Neutrons exiting the monochromator hit the sample with a defined momentum  $\vec{k}_i$  and energy  $E_i$ . The sample table rotation allows to orient crystal samples relative to the incoming beam. The analyzer placed at an angle  $2\theta$  (Fig. 3.1) selects by Bragg reflections the outgoing neutrons having the desired final energy, and reflects them towards the detector where they are counted. The scattering process  $(E_i, \vec{k}_i \rightarrow \vec{k}_f E_f)$  is thus entirely defined by the experimental geometry. Filters such as Be or BeO are placed on the neutron path to cut higher harmonics of the Bragg diffraction, and the analyzer and monochormator crystals can be bent to obtain higher flux at the sample at the expense of a loss in resolution. A typical layout of a triple axis instrument is given in Fig.3.2.

An alternative method to triple axis is the time of flight technique. The incoming neutrons reach the sample in pulses after passing through a chopper. For inelastic experiments they are additionally monochromatized before reaching the sample. The time at which they

<sup>4</sup>Typically Si, Ge or PG (pyrolytic graphite).

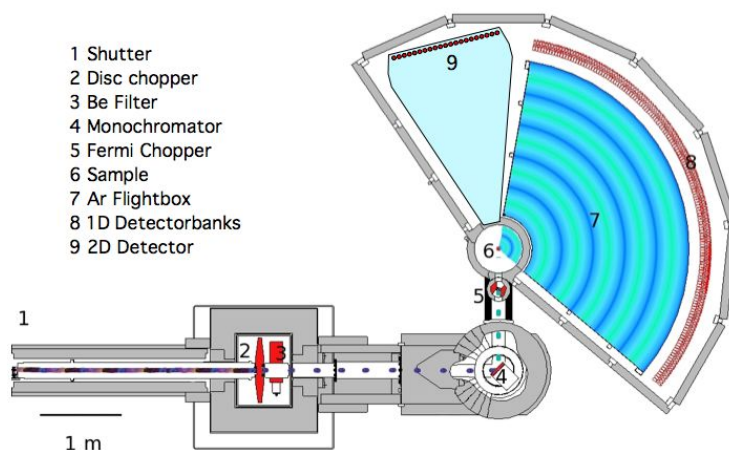


Figure 3.3: Schematic view of the time of flight instrument FOCUS at SINQ PSI. Reproduce from [59].

reach the detector is recorded allowing to compute their velocity hence their energy. This technique is particularly useful at spallation sources, where the neutrons are produced in pulses, so that the incoming neutron beam is not ‘wasted’ during the chopping process. Time of flight instruments typically have a collection of detectors covering a large angular region (Fig.3.3) thus allowing to map a large  $(\vec{Q}, E)$  range, but provide less flexibility than the triple axis instruments. The final choice between the two eventually depends on the particular experiment and the sample environment. Single crystal spectroscopy is more often performed on triple axis.

Powder diffraction is performed on dedicated diffractometers, like HRPT at SINQ. The neutron beam is monochromatized in a way similar to triple axis, but the analyzer stage is removed. The sample rotation, in principle not needed for isotropic powders, is still implemented in order to average for possible texture effects. The detector covers a large angular region to collect a maximum of Bragg reflections, and can be oscillated to average over its efficiency. In the case of HRPT oscillating radial collimators (mylar-Gd-O) have been added to remove Bragg peaks from the sample environment, this enabled us to solve the structure of  $\text{SrCu}_2(\text{BO}_3)_2$  under pressure with the Paris-Edinburgh press.

## 3.2 High pressure in neutron scattering

$\text{SrCu}_2(\text{BO}_3)_2$  with estimated coupling  $J'/J = 0.635$  is close to both the quantum phase transition to the plaquette and the AFM order phase. This is to say that relatively small changes in the structure could bring the material to enter a new phase. They are essentially two ways by which one can ‘tune’ a magnet across its parameter space:

1) Chemical substitution, i.e. replacing totally or partially some of the original atoms by other atoms in order to slightly modify the crystalline arrangement, so that the magnetic coupling paths are affected. These modifications should, in principle, not change the original structural symmetry. In many cases this has proven to be possible and even continuous substitution rates of one element by another have been achieved. In the case of  $\text{SrCu}_2(\text{BO}_3)_2$  this has proven to be a difficult task with only marginal substitution rates achievable [66], except on the Sr position [67].

2) Application of pressure to the original sample so that by reduction of the unit cell size, the magnetic exchange paths are modified. Apart from the technical difficulties involved by any type of high pressure study, this is the favored tool for tuning a magnet across quantum phase transitions without using an external magnetic field.

Historically the development of high pressure technics made tremendous progress through the achievements of Percy Bridgmann around the beginning of the 20<sup>th</sup> century. By his new sealing technics the maximal pressures increased from  $\sim 1$  kbar to  $\sim 20$  kbar [68, 69]. Opposed anvils cells and later diamond opposed anvils cell (DAC) allowed the pressure range to be further increased [69, 70]. For instance  $\sim 100$  kbar can be reached with WC or BN anvils on the Paris-Edinburgh press (PE) adapted to neutron scattering [71] and the megabar (1000 kbar) range in certain applications of the DAC [72]. Even higher (500'000 kbar! [69]) out of equilibrium pressures are possible for short times in shock experiments. Nevertheless high-pressure measurement constitute an experimental challenge.

The choice of the pressure cell and pressure transmitting medium<sup>5</sup>, has to be considered, from the specificities of the measurement. To cite a few: sample size, magnetic vs non magnetic material, transparent material for light, X-rays or neutrons, operational temperature range, cooling and warming time, expected signal to pressure cell induced background, etc. In the case of neutron scattering, Table 3.1 gives a review of existing devices with estimates of the maximal pressure and sample size. Except for the single crystal gems, the constituents should be understood in the sense of alloys with certain mixing rates and special thermal treatment. In general also, pressure cells are build in relatively small numbers and performance may vary within a generic type. Figure 3.4 shows the high-pressure neutron scattering possibilities at the spallation source ISIS (UK) as for 2002 [70]. In the lower pressure range  $p \leq 12$  kbar, allowing  $\text{cm}^3$  sample volume, the preferred materials are: TiZr and Al. Ti and Zr have opposite sign scattering lengths (-3.44 and 7.16 fm resp.) which, combined to their atomic masses (47.87 and 91.22 resp.), gives a zero coherent scattering when the two elements are mixed at about 50-50% mass ratio. This is particularly useful for diffraction studies as no additional Bragg peaks are produced by the pressure cell. Ti however possesses non negligible absorption cross section (6 barn), which limits the thickness of the pressure cell walls and its incoherent scattering cross section (2.9 barn) produces a constant background, that may not be acceptable for inelastic measurements with weak intensities. In this case, Al with small incoherent scattering (0.008 barn) and absorption (0.23 barn) is preferred. As a general rule, for weak intensities, as in INS, one will favor having all the pressure cell signal located at particular Q positions away from the region of interest, while for strong intensities and large Q-range studies, as in diffraction, distributing the background is preferable. Our first measurements under pressure on  $\text{SrCu}_2(\text{BO}_3)_2$  were limited to 12 kbar. They showed a reduction of the spin gap, indicating the systems was getting closer to the quantum phase transition. However it was clear that 12 kbar was not enough, and a new high pressure cell, named HPCAL17, was developed in collaboration with R. Sadikov from the Institute of High Pressure Physics in Toitsk, Russia. This cell improved the existing possibilities

---

<sup>5</sup>This is usually a liquid or a gas that will allow the pressure to be transmitted to the sample under hydrostatic conditions. Some times soft solids are also used as was the case in our low temperature Paris-Edinburgh press experiments.



P max	type	material	application	max. sample size
5 [73]	Hydraulic oil	Steel - Sapphire	SANS	1.3 cm <sup>3</sup>
5 [74]	Gas loaded	Al or TiZr	INS / Diffraction	~ 2 cm <sup>3</sup>
7-12 [70, 75]	Piston-cylinder	Al or TiZr	INS / Diffraction	1.1 cm <sup>3</sup>
17	Piston-cylinder HPCAL 17	Al - Steel	INS / Diffraction	1.1 cm <sup>3</sup>
20 [76]	Piston-cylinder	CuBe	Diffraction	0.2 cm <sup>3</sup>
25 [77]	Piston-cylinder	NiCrAl - CuBe	Diffraction	0.2 cm <sup>3</sup>
25 [78, 70]	Piston-cylinder McWhan	Al <sub>2</sub> O <sub>3</sub> - Steel	Diffraction /INS	0.1 cm <sup>3</sup>
100-200 [71]	Opposed anvils Paris-Edinburgh	WC or BN	Diffraction / INS	10-30 mm <sup>3</sup>
200 [79, 80]	Cubic anvils	WC	Diffraction	10 mm <sup>3</sup>
100 [81, 82]	Opposed anvils	Sapphire	Diffraction + field	1 mm <sup>3</sup>
500 [81, 82]	Opposed anvils DAC	Diamond	Diffraction + field	0.001-0.01 mm <sup>3</sup>

Table 3.1: An overview of the current possibilities in high pressure neutron scattering, with approximative maximal pressure and sample size. The last two entries are found at the LLB laboratory in Saclay near Paris, on a dedicated diffractometer G6-1. Thanks to the small size of the gem cells, combined pressure and magnetic field experiments are possible.

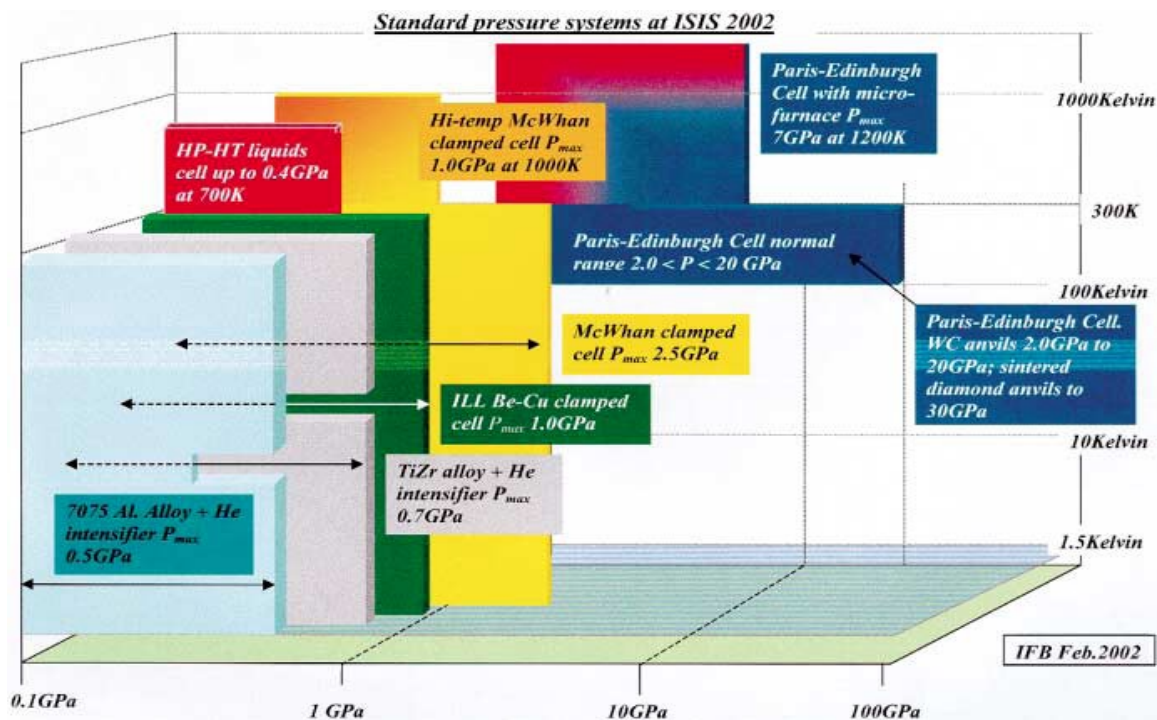


Figure 3.4: Pressure facilities available at ISIS in 2002. Reproduced from [70].

of INS with  $\text{cm}^3$  samples to 17 kbar, and is thus a major achievement on its own. The cell is composed of Al and is reinforced by a thin steel inset. The inset is pre-compressed to enhance its mechanical strength. The different parts of the cell are shown in Fig.3.6. We used and tested different Fluorinert<sup>TM</sup> as pressure transmitting liquid: Fluorinert<sup>TM</sup> FC87 - FC85 at 1:1 volume mixing on IN14 and Fluorinert<sup>TM</sup> FC77 on Panda. The maximal low temperature (1.5 K) pressure of 16.5 kbar was obtained during a test measurement at SINQ with a FC75-FC77 1:1 volume mixing and short ( $\sim 4.5$  cm) Teflon cans as sample container. This particular Fluorinert mixing has the advantage of not losing pressure upon cooling after the cell is loaded to the maximal pressure, whereas we experienced pressure loss with FC87-FC85 1:1. For ambient temperature measurement FC87 and FC84-FC87 1:1 should still be preferred as they have higher hydrostatic limits, resp. 22 and 23 kbar, than FC75-FC77 1:1 (16 kbar) or FC75 (15 kbar) [83]. FC87 however

is no longer produced [84] and one has to rely on the existing stocks. The short teflon cans produce less friction than longer cans and than Pb cans. Teflon cannot be used to determine the pressure as it can be done with Pb [75], and one has to add a reference, for instance NaCl, for pressure determination<sup>6</sup>. HPCAL17 enabled us to obtain high quality

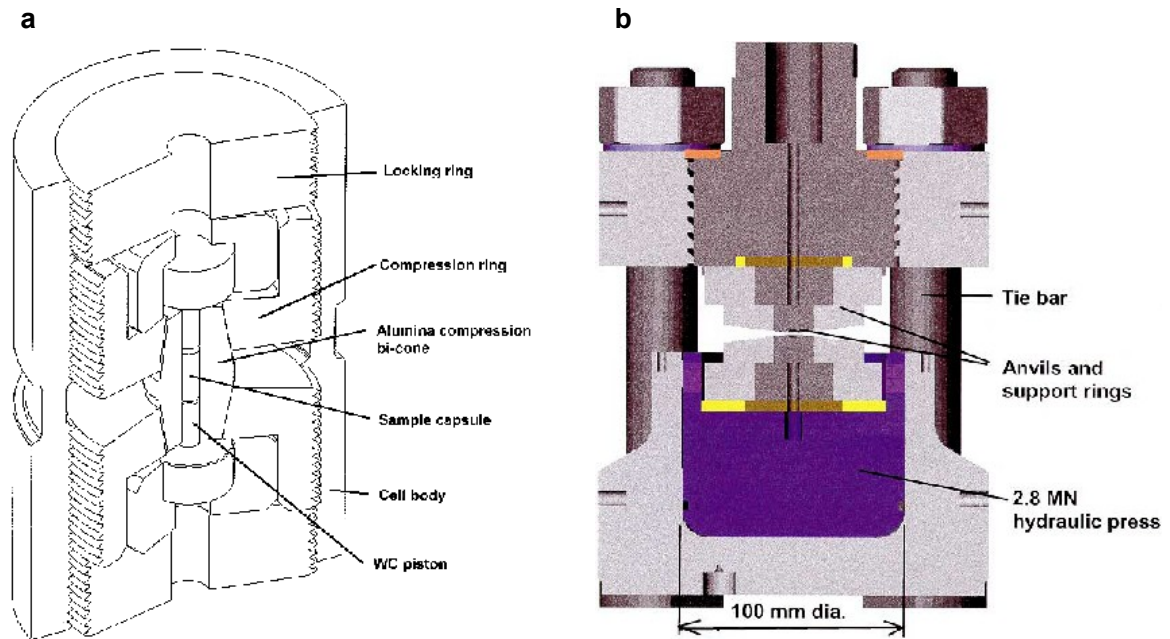


Figure 3.5: High pressure cells: (a) Schematic of the McWhan cell. (b) Schematic of the Paris-Edinburgh press. Reproduced from [70].

INS data for  $\text{SrCu}_2(\text{BO}_3)_2$ , the study of the new quantum phase however required even higher pressures and was made possible using a McWhan cell [78] at the cost of massive loss in sample mass (from 3g to 0.2g). The McWhan cell developed in the 70's has an alumina ( $\text{Al}_2\text{O}_3$ ) bi-cone core through which Tungsten carbide (WC) pistons compress the sample. The alumina core itself is compressed radially by the compression rings (Fig.3.5 a). We used Fluorinert<sup>TM</sup> FC84-FC87 1:1 as pressure transmitting medium and were able to reach 21.5 kbar at 0.5 K. The Paris-Edinburgh press [71] allows to reach pressures above 100 kbar. It uses an opposed anvil technic similar to DAC but with much larger

<sup>6</sup>This is done directly on the neutron instrument by measuring the shift in lattice constant of the reference.

sample space as is often required in neutron scattering experiments. Compared to piston clamp cells it offers the advantageous possibility of changing the pressure directly on the instrument. We used Boron nitride (BN) anvils for powder diffraction experiments. These provide a direct collimation of the neutron beam on the sample thanks to the huge absorption cross section of Boron. To hold the radial forces a TiZr gasket is placed around the sample container and we used deuterated methanol-ethanol at 4:1 volume as pressure transmitting medium. For single crystal experiments, the Paris-Edinburgh press was cooled down to 3.5 K using a close cycle cryostat, and pressure could usually be changed around 100 K. The toroidal anvils made of WC were specially manufactured to obtain large aperture angles [85] useful when tilting the single crystal. The sample is placed in a CuBe ring inserted in Pb matrix acting as pressure transmitting medium and hold by an Al gasket. For low temperature experiments, the pressure is transmitted to the anvils by a He capillary as hydraulic oil cannot be used. The Paris-Edinburgh press can also be used with sintered diamond anvils to reach 300 kbar [70].

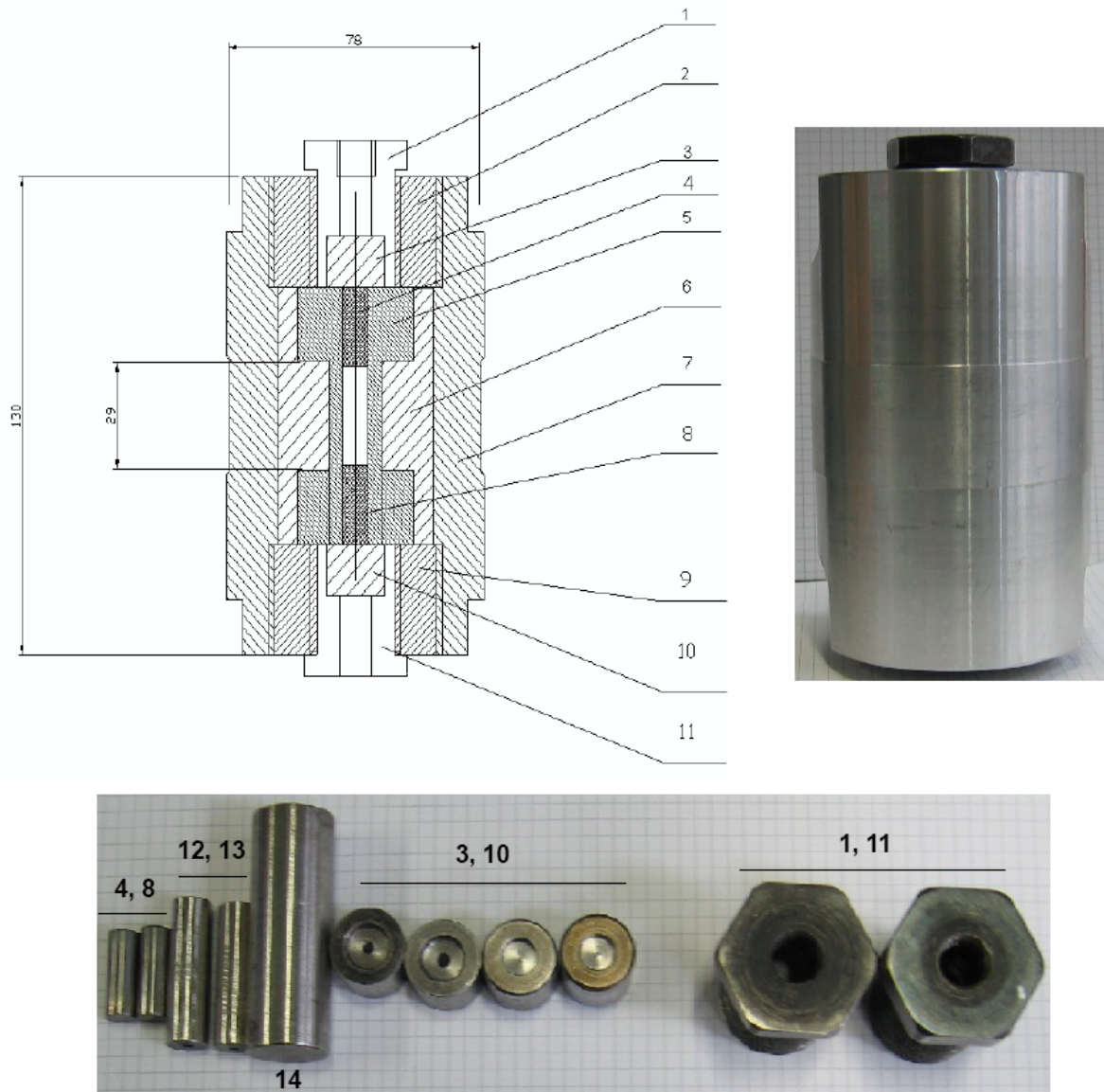


Figure 3.6: New pressure cell: HPCAL 17. Components: (1, 11): top and bottom clamp screws. (2, 9): top and bottom pre-compression screws. (3, 10): top and bottom piston holders. (4, 8) top and bottom inner pistons. 5: steel inset. 6: Al inset. 7 Al outer wall. (12, 13): push pistons. 14: Inset pre-compression push piston.



# Chapter 4

## Unusual temperature damping in $\text{SrCu}_2(\text{BO}_3)_2$

This chapter presents our results on the temperature dependence of the gapped excitation in  $\text{SrCu}_2(\text{BO}_3)_2$ . The excitation, measured by INS, shows a peculiar behavior: although the spin gap is 35 K the peak intensity is strongly suppressed above 5 K and disappears into a flat continuum around 15 K. Our INS study on powder and single crystals as a function of  $\vec{Q}$  and magnetic field shows that, while the peak intensity rapidly decreases as function of the temperature, the integrated spectral weight can still be matched to an isolated dimer model up to 10 K. An analysis using damped harmonic oscillators shows that the line shape can be modeled with a two component damping process: one mode remains resolution sharp while the second broadens and their intensities are exchanged as T increases. The energies, intensities and damping widths are determined and the underlying physics discussed.

### 4.1 Time of flight measurements on $\text{SrCu}_2(\text{BO}_3)_2$ powder

A time of flight INS measurement was performed on the FOCUS spectrometer (see Fig.3.3) located at the Swiss spallation source SINQ at PSI. FOCUS was operated with incoming

energy monochromatized to 7 meV between the disk chopper and the Fermi chopper, and with 3 detector banks covering a large angular range from 10 to 130 degrees in  $2\theta$ . The powder  $\text{SrCu}_2(\text{BO}_3)_2$  sample of 12 g was placed in a 12 mm diameter aluminium holder. TOF spectra were taken at 2, 6.25, 7.5, 10, 15 and 20 K and an empty aluminium can measurement at low temperature was used for background subtraction (signal to background ratio =12 on the 2 K peak). Figure 4.1 presents the temperature dependence of the excitation spectrum up to 5.5 meV and shows the singlet-triplet gap and the two bound triplet excitation around 3 and 5 meV respectively. Although the spin-gap is  $\sim 35$  K ( $\sim 3$  meV) the observed Q-integrated excitation starts to be strongly suppressed above 5 K and turns into a flat continuum around 15 K. It can also be seen from Fig.4.1 that the excitation broadens as the peak intensity reduces, and its center slightly moves towards higher energies.

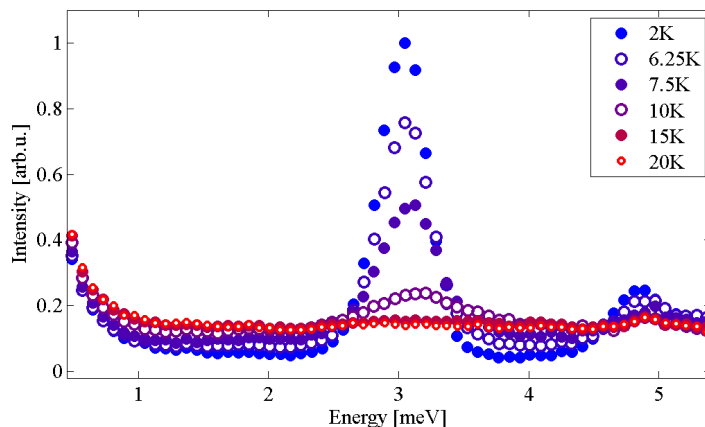


Figure 4.1: Q-integrated spectrum as function of temperature for a  $\text{SrCu}_2(\text{BO}_3)_2$  powder sample.

So far the temperature dependence of the gap excitation has been discussed mostly in terms of the reduction of peak intensity [33, 34, 86]. Gaussian fits to the spectrum show a dramatic decrease of the peak intensity and an increase of the ‘background’ (Fig.4.2 left). In fact not only the peak intensity is reduced, but the system undergoes a damping mechanism, with the excitation broadening around its central energy. Little has been proposed so far for the understanding of the integrated intensity and for the damping itself. Haravifard et al [66] however observed that the substitution of  $s = 1/2$   $\text{Cu}^{2+}$  ions by non magnetic  $\text{Mg}^{2+}$  resulted in an increase in damping widths. The correct determination



of the total integrated intensity is hindered by the issue of the integration range, as for low energies the damped excitation merges with the much more intense elastic line while at high energies, it merges with the two-triplet excitation around 4.2 meV. Figure 4.2 left (triangle symbols) shows the integrated magnetic intensity in the 0.5-4.2 meV range. The measured INS excitation is proportional to the number of singlets in the system (Fig.A.1), however when T increases the intensity scattered into this energy range departs from the isolated dimer singlet population (black line). The integrated intensity lies mostly below the dimer line indicating damping also occurs outside of this integration range. At higher temperatures (15-20 K) higher energy excitations are being damped into the 0.5-4.2 meV range and new low energy transitions between thermally populated states become possible, which explains the smaller decrease of the integrated intensity. Figure 4.2 right shows an interesting behavior of the partial integral (i.e. integrated intensity as function of the upper integration limit). It demonstrates the intensity is damped symmetrically to the higher and lower energy sides as the same spectral weight is recovered for all temperatures at the gap energy. This behavior is robust upon lowering the integration limit and the unique crossing point converges towards the gap energy.

The broadening is clearly of magnetic origin, the non-magnetic background (remaining after the empty can subtraction) is obtained from the base temperature spectrum outside the almost resolution limited 3 meV peak. Its magnetic nature is further assessed by the Q-energy maps in Fig.4.3 and Q-cuts at different energies in Fig.4.4. At 2 K the Q-cut on the gap excitation,  $E=2.8-3.2$  meV (blue circles), shows a maximum around  $Q = 1.1 \text{ \AA}^{-1}$  corresponding to the  $\text{SrCu}_2(\text{BO}_3)_2$  dimer structure factor, followed by a decrease at higher Q corresponding to the magnetic form factor of the Cu ion. Outside the peak region for  $E=3.8-4.2$  meV and  $E=1.5-2.2$  meV (open green symbols), the Q dependence is different: essentially flat except for some intensity around  $Q = 2 \text{ \AA}^{-1}$  which is due to a Bragg peak. The cuts at energies higher ( $E=3.8-4.2$  meV) and lower ( $E=1.5-2.2$  meV) than the gap are similar and have been combined. This base temperature non-magnetic background is assumed to be energy and temperature independent and is thus subtracted from all the other cuts giving the blue and full green symbols in Fig.4.4. It can clearly be seen that as T increases the off center cut acquires more structure and eventually becomes identical to the central energy cut at 15 and 20 K. However, although they share the similar general

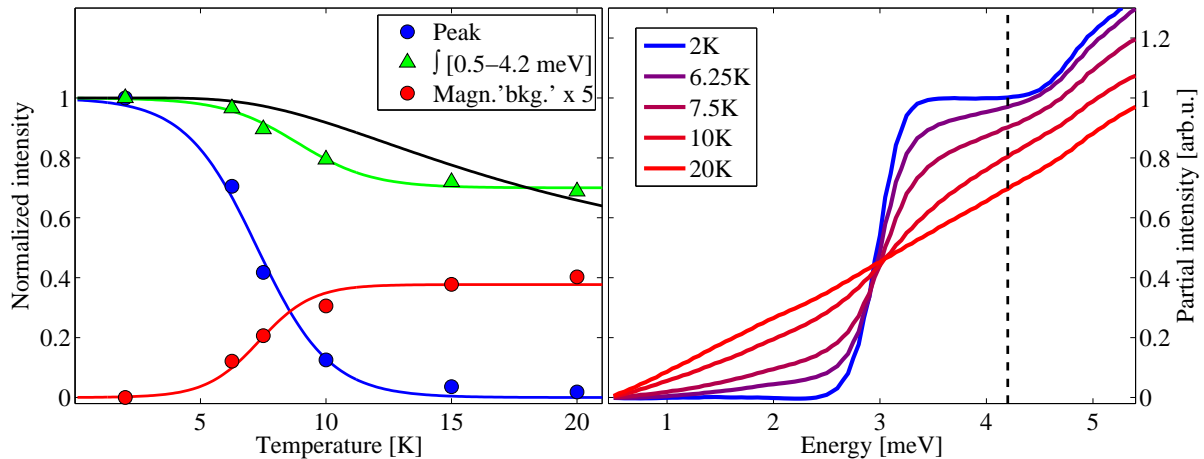


Figure 4.2: Integrated and peak intensity as function of temperature for a  $\text{SrCu}_2(\text{BO}_3)_2$  powder sample. Left: Peak intensity with varying background (in same unit as the peak) from Gaussian fits, and integrated intensity in the 0.5-4.2 meV range, color lines are guides to the eye. The black line is a  $\Delta=35$  K isolated dimer singlet population. Right: Partial integral of the measured intensity: integrated intensity from 0.5 meV as function of the upper integration limit

feature of a maximum and a decrease at larger  $Q$ , the  $Q$  dependent shape of the magnetic signal at 15-20 K is different from the 2 K base temperature and the maximum has shifted to lower  $Q$ .

## 4.2 Damped Harmonic oscillator

To further analyze the spectrum a theoretical line shape is needed. Although there is no general result for intrinsic line shapes at finite temperature, one often uses a simple Lorentzian form, corresponding to the Fourier transform of an exponential decay for the excitation's life-time. The simple Lorentzian however does not satisfy the required detailed balance rule (3.24) and does not imply an odd imaginary part for the susceptibility (3.21 and 3.22). The slightly more sophisticated damped harmonic oscillator (DHO) form obtained from linear response theory has the advantage to fulfill both requirements. It has been first discussed for the finite temperature line shape of phonons in solids and

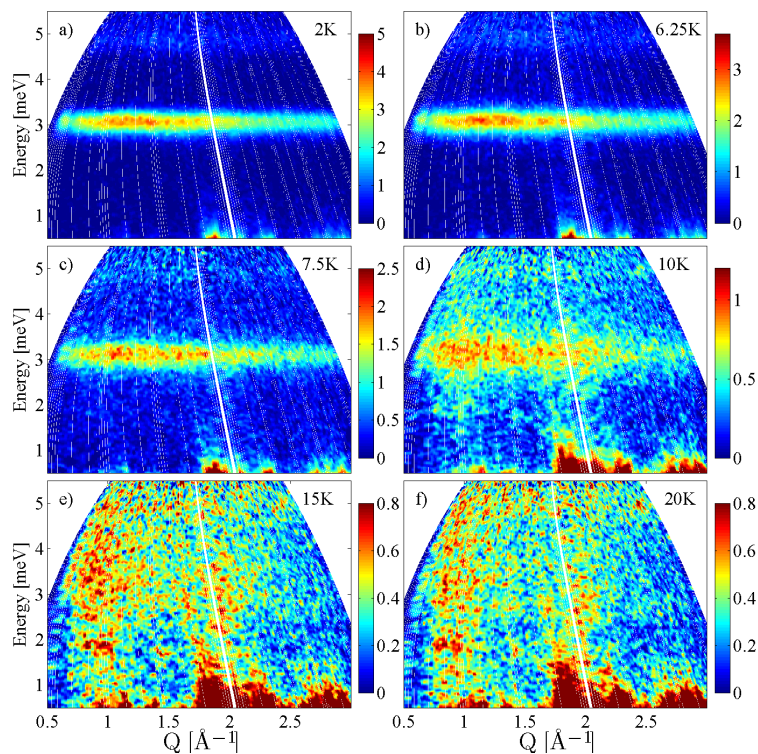


Figure 4.3:  $Q$ -energy color maps as function of temperature for a  $\text{SrCu}_2(\text{BO}_3)_2$  powder sample.

phonon-like excitations in liquids and the discussion applies also to magnons [63, 87]. We give two equivalent formulations of the dynamical structure factor  $S(\vec{Q}, \omega)$  to which the INS signal is proportional (see Eq.3.19). While the first one is commonly used, the second more clearly shows that it consists of the difference of two Lorentzians weighted by the detailed balance<sup>1</sup> factor so that it simultaneously satisfies the two requirements mentioned above. The DHO tends to two Dirac functions at  $+\omega_0$  and  $-\omega_0$  for vanishing damping widths.

$$S(\vec{Q}, \omega) = \frac{F(\vec{Q})}{\pi} \frac{[n(\omega) + 1]4\omega\Gamma}{(\omega^2 - \Omega_0^2)^2 + 4\omega^2\Gamma^2} \quad (4.1)$$

$$S(\vec{Q}, \omega) = \frac{[n(\omega) + 1]F(\vec{Q})}{\omega_0\pi} \times \left[ \frac{\Gamma}{(\omega - \omega_0)^2 + \Gamma^2} - \frac{\Gamma}{(\omega + \omega_0)^2 + \Gamma^2} \right] \quad (4.2)$$

<sup>1</sup>Also called Bose factor and having the following property:  $n(\omega) + 1 = -n(-\omega)$

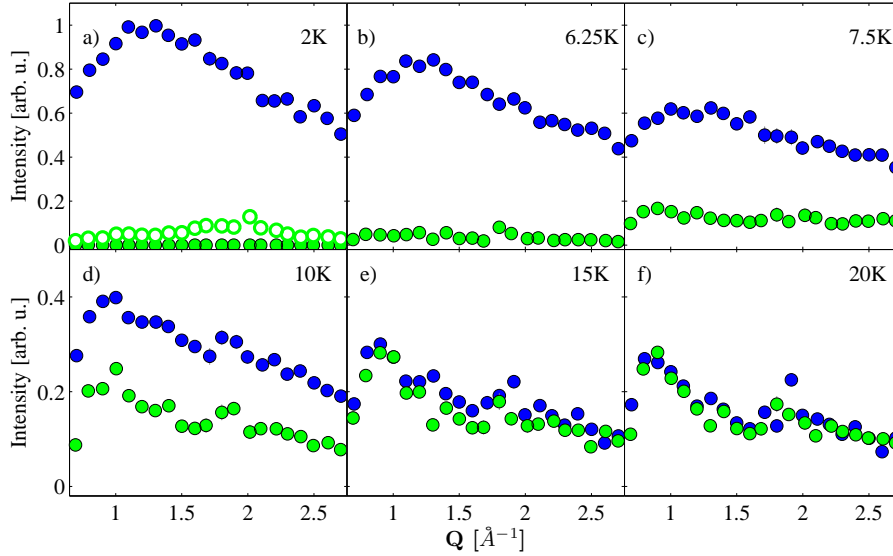


Figure 4.4: Constant energy cuts of the  $(Q,E)$  maps of Fig. 4.3. Blue:  $E=(2.8-3.2 \text{ meV})$ . Full green:  $E=(3.8-4.2 \text{ meV})$  and  $(1.5-2.2 \text{ meV})$ . Open green in (a) defines the non-magnetic background and is subtracted from all other cuts.

with

$$\Omega_0^2 = \omega_0^2 + \Gamma^2, \quad n(\omega) = \frac{1}{e^{\frac{\omega}{T}} - 1} \quad (4.3)$$

$\omega_0$  is the undamped excitation energy,  $\Gamma$  the DHO half width,  $n(\omega)$  the detailed balance factor, and  $F(\vec{Q})$  accounts for the  $Q$ -dependence of the intensity. In the case of magnetic excitations  $F(\vec{Q})$  is the real part of the susceptibility  $\text{Re}\chi(\vec{Q})$ . For simplicity, we use  $\hbar$  and  $k_b = 1$ . For data analysis, the DHO is convolved with a Gaussian to account for the instrumental resolution. The integrated intensity,  $\omega_0$  and  $\Gamma$  are the fit parameters. It should be noted that in the low temperature range  $\leq 10 \text{ K}$ , and for the damping widths we finally obtained, results only negligibly depart from a Lorentzian convoluted to a Gaussian, i.e. from a Voigt function with half Lorentzian width  $\Gamma$ .

### 4.3 High field triple axis measurements on single crystals

Having fixed the line shape,  $Q$ -dependent single crystal data are needed to understand the damping mechanism. The situation is complicated by the fact that the triplet excitation is

slightly split ( $\sim 0.2$  meV) by DM interactions at zero field, and the different branches could in principle have different damping, as one could think of the  $S_z = \pm 1$  modes relieving next-nearest neighbor frustration in a different manner than the  $S_z = 0$  mode. They are essentially three ways to study the triplet modes individually: 1) apply a magnetic field in order to separate the Zeeman split modes, 2) use very high resolution neutron scattering at zero field (at the cost of intensity), 3) use polarized neutrons to separate the central mode from the two others [88] (also at the cost of intensity). We performed the first two options which enabled us to extract a model for the temperature damping of  $\text{SrCu}_2(\text{BO}_3)_2$ .

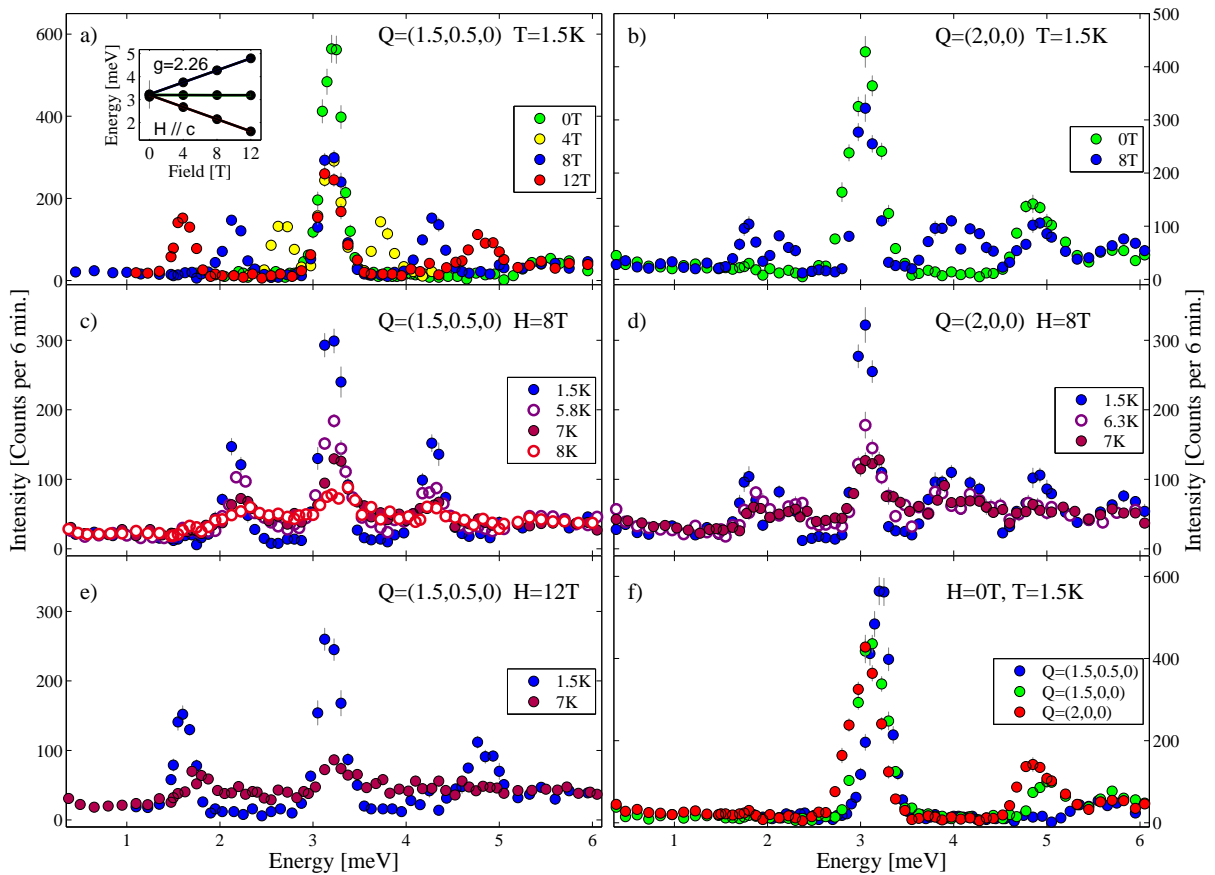


Figure 4.5:  $\text{SrCu}_2(\text{BO}_3)_2$  Single Crystal: Excitation spectrum at various fields, temperatures and Q points. The inset in (a) shows the Zeeman splitting for  $Q=(1.5,0.5,0)$ .

High field INS measurements were taken at the FRM2 research reactor in Garching (Germany) on the triple axis instrument PANDA with a 3 g single crystal mounted in a 15 T cryomagnet with a and b axes in the scattering plane and  $H//c$ . The instrument

was operated at fixed  $k_f=1.55 \text{ \AA}^{-1}$  with double focusing monochromator and horizontally focusing analyzer. Figure 4.5 shows the raw spectra obtained on Panda. At 8 T the three modes are sufficiently separated to clearly observe individual damping. At  $Q=(1.5,0.5,0)$  the triplet intensity is high and the multi-triplet states are reduced in intensity and higher in energy [35, 89] so that their influence is minimal on the one triplet spectrum. At  $Q=(2,0,0)$ , due to DM interactions, the upper and lower triplets further split into two branches each, with the upper mode merging into the bound triplet above 6 K. At 12 T the upper triplet mode also mixes with the lower modes of the  $s=1$  bound state, making a clean analysis difficult. We shall thus use the  $Q=(1.5,0.5,0)$  data at 8 T to fix the temperature damping model for  $\text{SrCu}_2(\text{BO}_3)_2$ . It can first be seen (Fig.4.5 a) that there is no redistribution of spectral weight among the triplets when field is applied as was observed for  $Q=(1.5,0,0)$  in Ref. [90]. The second observation is that no major changes in damping occur among the three triplet branches.

Several fitting procedures based on DHO line shapes were implemented to explain the experimental data. The fit parameters were fixed step by step to obtain the simplest model yielding satisfactory fits. The final result uses *two* DHO for each mode and is shown in Fig. 4.6 (red line) where it is compared to a single DHO broadening (black line). While fitting the three modes with one DHO each works for the lower temperatures, it clearly fails at 7 and 8 K. We thus implemented a two component –sharp and broad– DHO damping for each mode. It turns out, over the studied temperature range, that the sharp component remains resolution limited  $\Gamma = 0$ . The total integrated intensity (the sum of the broad and sharp components) is essentially constant and can be matched, within error bars, to the isolated singlet dimer population. The ratios sharp to broad intensities for each triplet mode are found to be similar and are correlated in the final fit. The  $\Gamma$  for each modes are left uncorrelated, the shift in energy could influence their value. The  $\omega_0$  shifts are correlated. Once the base temperature spectrum is fitted, the remaining temperature dependent fit parameters are thus:  $\{I^{S1}, \omega_0^{S1}, \Gamma^{B1}, \Gamma^{B2}, \Gamma^{B3}\}$ , where I is the integrated intensity. The superscripts S and B refer to sharp and broad components and the numbers 1, 2, 3 to the lower, middle and upper triplet respectively.

The fit results are summarized in Fig.4.7. The excitations are not only damped but slightly

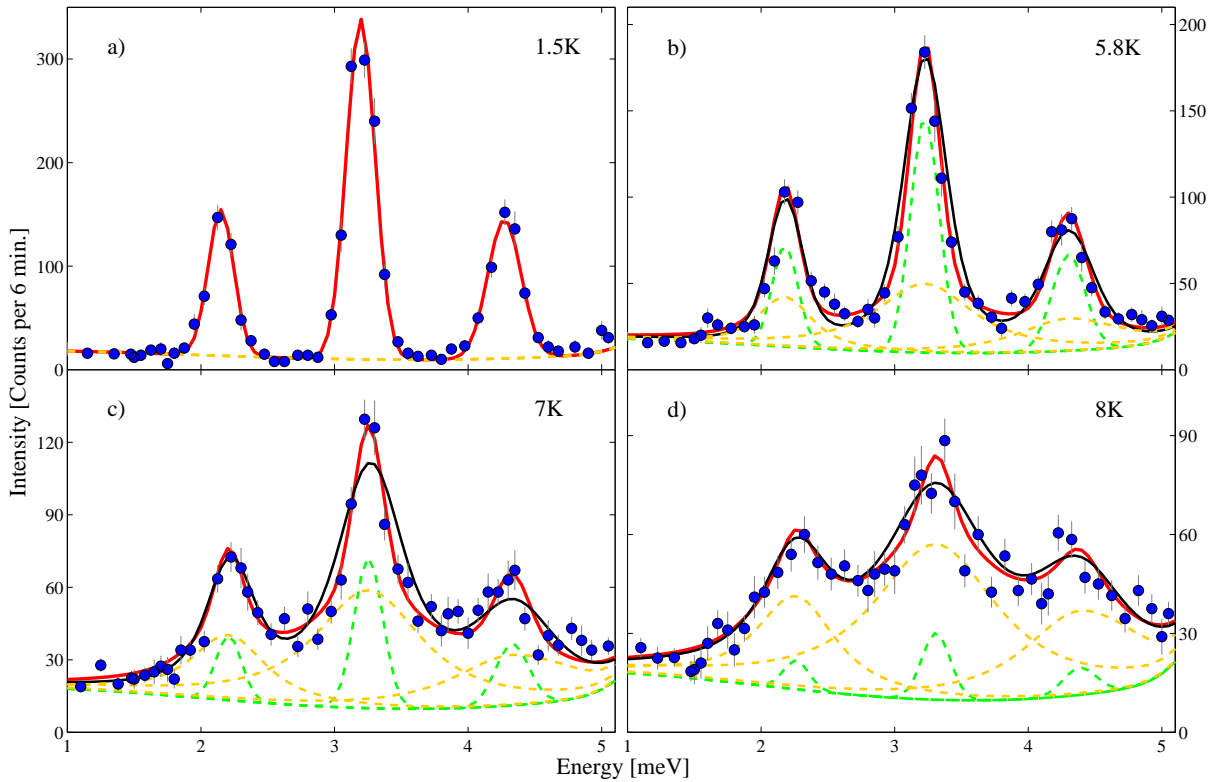


Figure 4.6: SrCu<sub>2</sub>(BO<sub>3</sub>)<sub>2</sub> Single Crystal temperature dependence. Fits to the excitation spectrum at H=8 T, Q=(1.5,0.5,0): The black line assumes a single component DHO damping. The red line is the fit result with our two component model (see text). Dashed lines are the resolution limited sharp (green) and broad (orange) components.

shift to higher energies as observed in the powder sample. The integrated intensity of the sharp component quickly drops to zero while the broad intensity increases. There is in fact, as a function of temperature, a remarkable exchange of spectral weight between the two components with a cross-over at 5.5 K. At 8 K the sharp component has almost completely vanished. The measured integrated intensity over a finite range (0.5 to 4.2 meV for instance) decreases faster than the fitted value indicating that the damping involves a large energy range as can be expected from a Lorentzian form. The damping widths  $\Gamma$  of the upper and middle triplets are similar while the lowest is sharper indicating the damping is not simply governed by the individual triplet energies.

We shall now apply the same model to zero field data at different Q points.

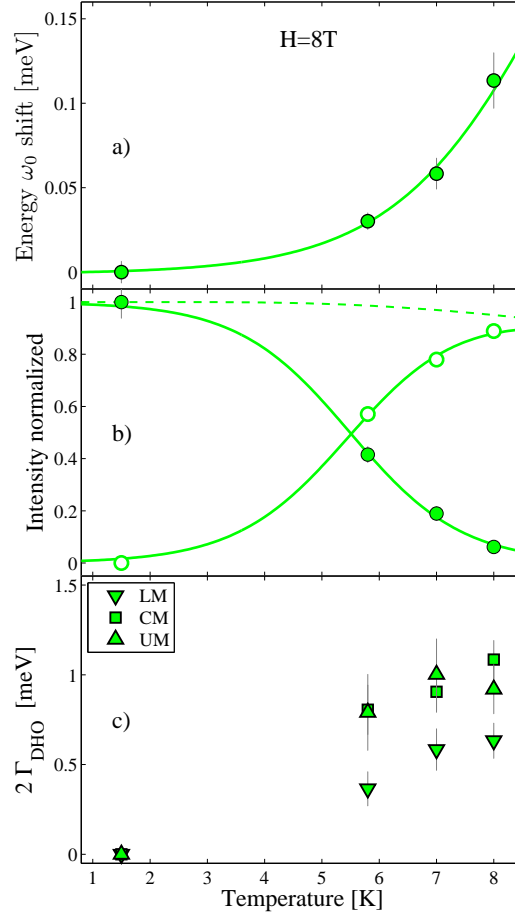


Figure 4.7: Fit parameters for the two component damping model at 8 T,  $Q=(1.5,0.5,0)$ . Open (close) symbols in (b) refer to the broad (sharp) component. The dashed line is the isolated singlet population at 8 T. In (c) the LM, CM, UM, are the lower, middle, and upper triplet modes respectively. Full lines are obtained by fitting the parameters to a sigmoidal function of type  $1/(1 + e^{-a(T-c)})$ .

#### 4.4 Triple axis measurements at zero field

Zero field measurements (Fig.4.8) were performed on the triple axis instrument TASP at SINQ. TASP was operated at fixed  $k_f=1.2 \text{ \AA}^{-1}$  with coaligned single crystals. The measurement for  $Q=(1.5,0.5,0)$  had the a and b axes in the scattering plane while for  $Q=(1.5,0,0)$  and  $Q=(2,0,0)$  the a and c axes were the scattering plane. The total sample mass was 8 g, and the achieved energy resolution 0.18 meV at  $E=3$  meV. At zero field the three triplets are slightly split ( $\sim 0.2$  meV) because of DM anisotropies, and their relative intensities vary with  $Q$  [90, 34, 35]. At  $Q=(1.5,0,0)$  and  $Q=(2,0,0)$  we observe a double



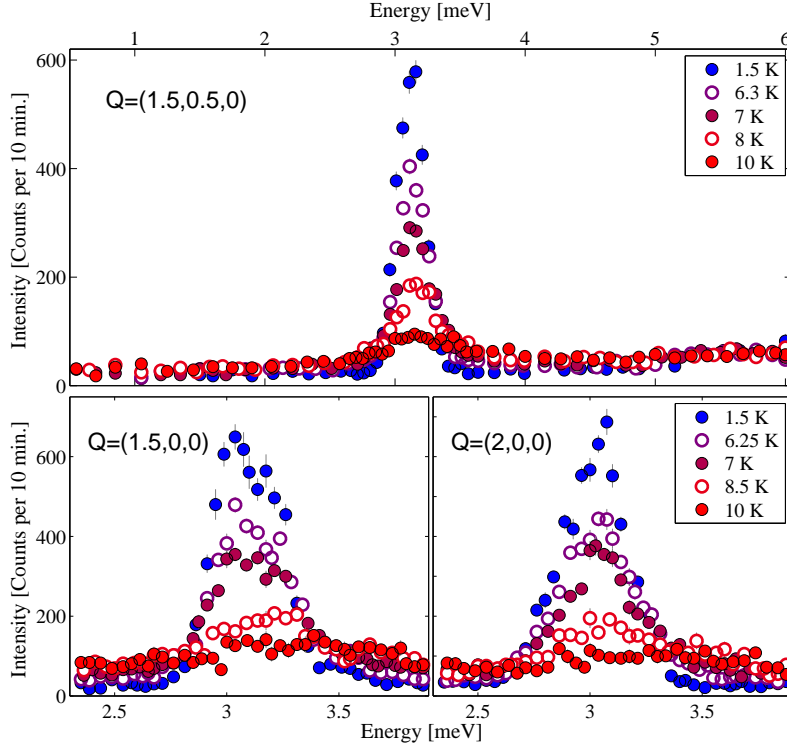


Figure 4.8: SrCu<sub>2</sub>(BO<sub>3</sub>)<sub>2</sub> Single Crystal temperature dependence at zero field. Excitation spectrum for Q=(1.5,0.5,0), Q=(2,0,0) and Q=(1.5,0,0).

and a triple peak structure respectively while at Q=(1.5,0.5,0) the excitation is essentially a single peak in accordance with previous work [35]. We apply the model derived above to fit the zero field data: each DM split mode is fitted by two DHO, one remaining resolution sharp. The intensity ratios of the two components are correlated and the total intensity is matched to the isolated singlet population. The  $\omega_0$  shifts are correlated. The  $\Gamma$  are this time also correlated as the triplets are on the same energy scale, and it would be extremely difficult to assign a difference in broadening to one specific peak when they are so close. After fitting the base temperature spectrum, the remaining set of variable parameter is thus:  $\{I^{S1}, \omega_0^{S1}, \Gamma^{B1}\}$  where the number 1 refers to the first DM split mode. As shown in Fig.4.9 and 4.10 our damping model, obtained from Q=(1.5,0.5,0) H=8 T measurement, matches the zero field data very well. It can also be directly applied to the other two Q points, although these have a different intrinsic triplet structure. A single DHO broadening again fails to fit the data as shown by the black line in Fig.4.9.

The results of fits are summarized in Fig.4.11 a-c. The damping width and the shift in

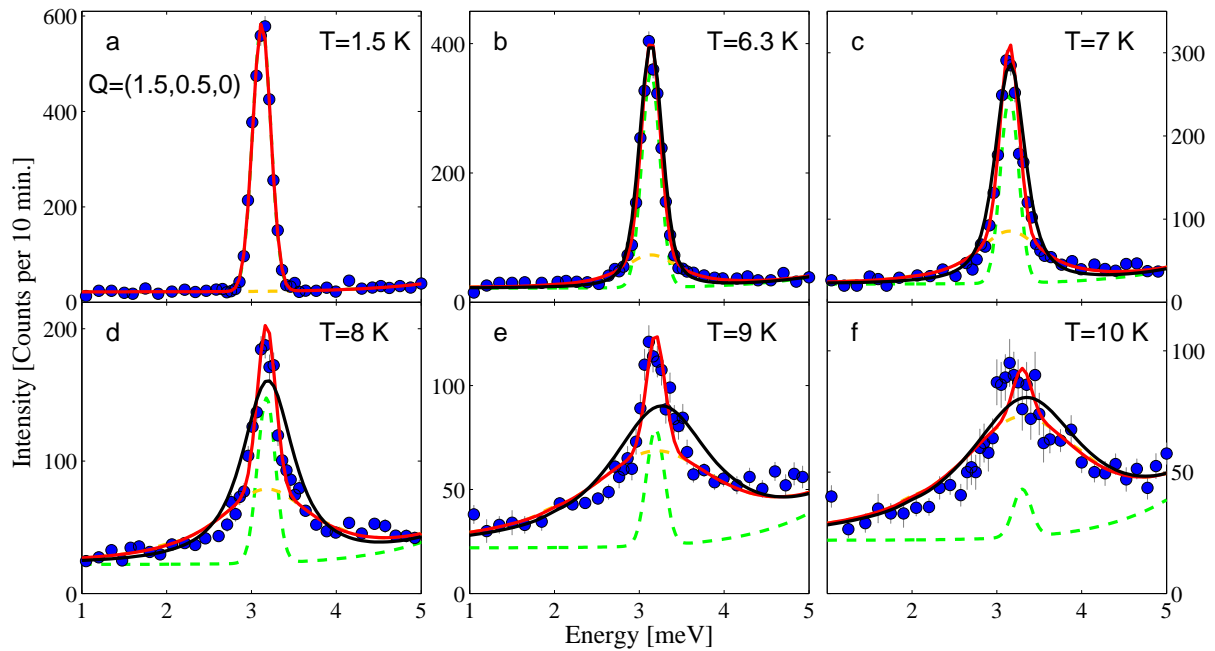


Figure 4.9: Fits to the excitation spectrum at  $H=0$  T,  $Q=(1.5,0.5,0)$ : The black line assumes a single component DHO damping. The red line is the fit result with our two component model. Dashed lines are the resolution limited sharp (green) and broad (orange) components.

energy appear to be slightly larger for  $Q=(2,0,0)$ . The integrated intensities on the other hand remarkably lie on top of each other for the three  $Q$  points with a cross-over at 6.8 K. Upon comparing 0 and 8 T results in Fig.4.11 d-f, one notices an increase in the energy shift as function of field and a reduction of the cross-over temperature for the sharp and broad components of about 0.15 K/T.

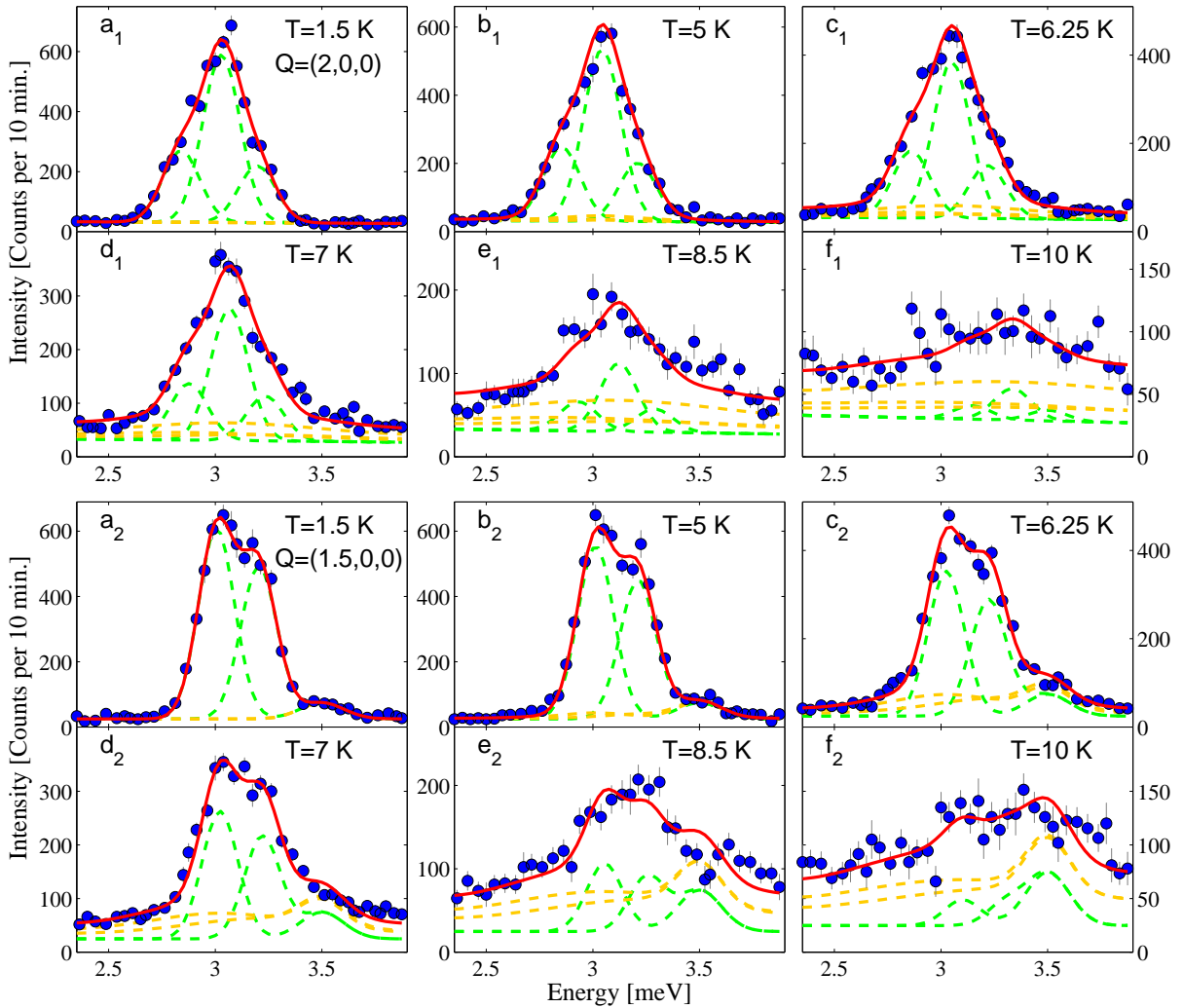


Figure 4.10: Fits to the excitation spectrum at  $H=0$  T. Upper panel ( $a_1$ - $f_1$ ):  $Q=(2,0,0)$ . Lower panel ( $a_2$ - $f_2$ ):  $Q=(1.5,0,0)$ . The red line is the fit result with our two component model. Dashed lines are the resolution limited sharp (green) and broad (orange) components. For  $Q=(1.5,0,0)$  the bump around 3.5 meV is a temperature independent spurious background peak already present at 1.5 K.

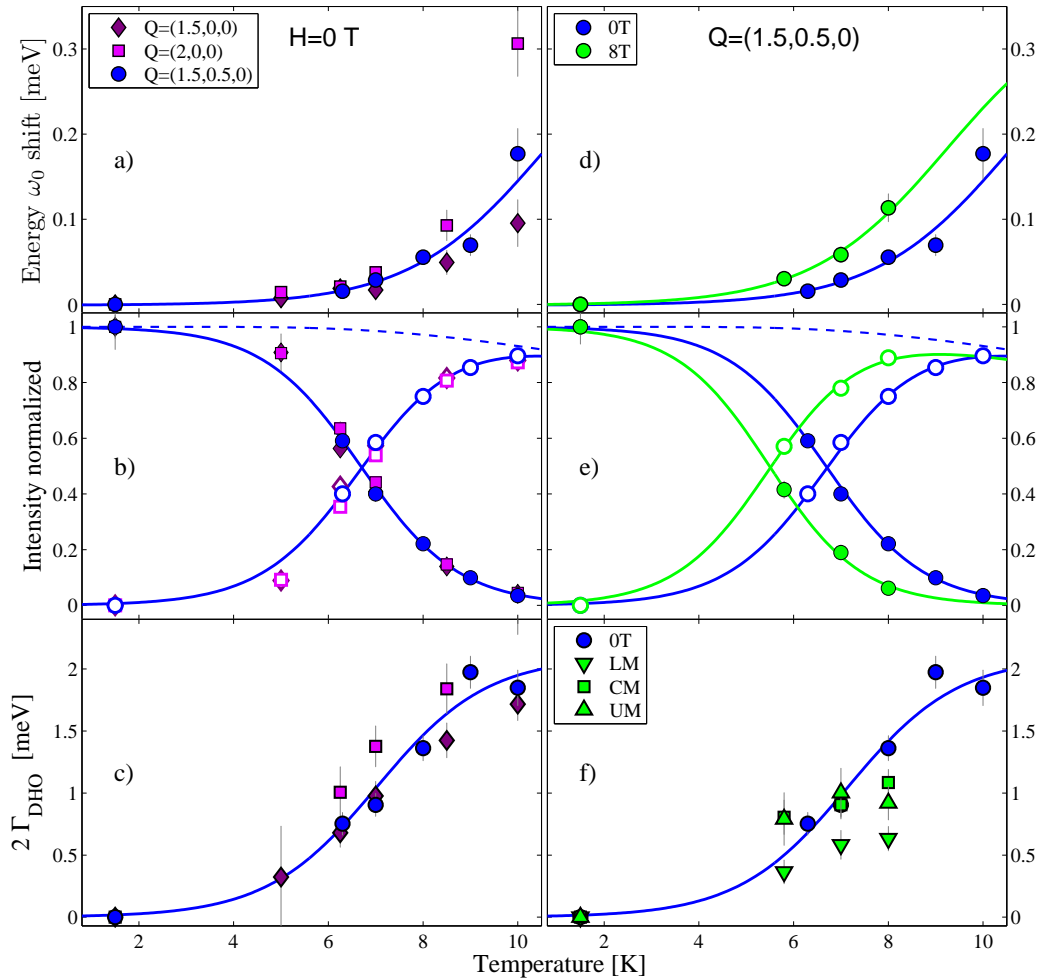


Figure 4.11: Fit parameters as a function of Q (Left) and field (right). Open (close) symbols in (b,e) refer to the broad (sharp) components. The dashed line is the isolated singlet population at 0 T. In (f) the LM, CM, UM, are the lower, middle, and upper triplet modes respectively. Full lines are guides to the eye obtained by fitting the parameters to a sigmoidal function of type  $1/(1 + e^{-a(T-c)})$ .

## 4.5 A phenomenological model for the temperature damping

The model derived for the finite temperature damping in  $\text{SrCu}_2(\text{BO}_3)_2$  is robust, as it describes field and zero field data at various Q points. The line shape of the excitation spectrum can be modeled by a mechanism with two components. The first one involves undamped triplets, that remain with a well defined (sharp) energy. This type of triplet excitation is rapidly suppressed when increasing temperature, and even more rapidly in the presence of a magnetic field. The second type of triplet excitation decays quickly with characteristic damping widths increasing with temperature. The total integrated intensity does not vary much in the 0-10 K temperature range and can be matched to an isolated singlet population. However, while at base temperature the triplet excitations are all sharp, above  $\sim 10$  K they all decay, and an exchange in the probability ratio of the two processes occurs in between. This implies that the presence of a very small percentage of thermally excited triplets strongly modifies the thermodynamical properties in  $\text{SrCu}_2(\text{BO}_3)_2$ . This is somehow reminiscent of the correlated hopping where an isolated triplet cannot move on the Shastry-Sutherland lattice<sup>2</sup>, while the presence of another triplet in the vicinity will allow it to hop to neighboring sites.

The decay mechanism can be modeled by thinking of a simultaneous presence of triplets on the lattice. We consider first the following process: a triplet excitation created by the neutron will remain well defined when no other triplets are present, but will decay if thermally excited triplets are present nearby. This will account for the broad and sharp components of the spectra. The triplet densities involved are very low: at 6.8 K, the crossover temperature for the broad and sharp damping, a  $\Delta=35$  K isolated dimer has a triplet density of about only 2% (see Appendix A) and this is enough to end up with the same probability for a triplet decaying or remaining sharp. At 10 K, the triplet density is about 9% and all triplets decay. The low triplet density in turn would imply that one triplet can ‘feel’ the presence of another triplet at an extended distance. To be more quantitative we use the 2D Shastry-Sutherland lattice, which has two dimers per unit

---

<sup>2</sup>Except by unlikely processes starting at 6<sup>th</sup> order in perturbation, while correlated hopping already starts at 2<sup>nd</sup> order [7] and is the main source for the triplet motion.

cell, and compute the temperature dependent probability for having (and not having) a thermal triplet within a spacial range extending to  $N_u$  unit cells around a given dimer: The probability of having only singlets in these  $N_u$  unit cells is:

$$P_s(T) = n_s(T)^{2N_u} \quad (4.4)$$

with  $n_s(T)$  the singlet density. The second probability to compute corresponds to having a singlet on the given dimer – so that it can be excited by the neutron – and at least one triplet on  $2N_u-1$  remaining dimers:

$$P_t(T) = n_s(T) - n_s(T)^{2N_u} = n_s(T) - P_s(T). \quad (4.5)$$

$P_s(T)$  accounts for the sharp component, as the neutron excited triplet is created in a region where no thermal triplets are present and thus remains sharp.  $P_t(T)$  accounts for the broad component as the neutron excited triplet is created in a region where there are thermal triplets causing its decay. This microscopic phenomenological model matches the experimental temperature dependence of the broad and sharp intensities very well for a number of unit cells  $N_u$  of about 21 (Fig. 4.12).

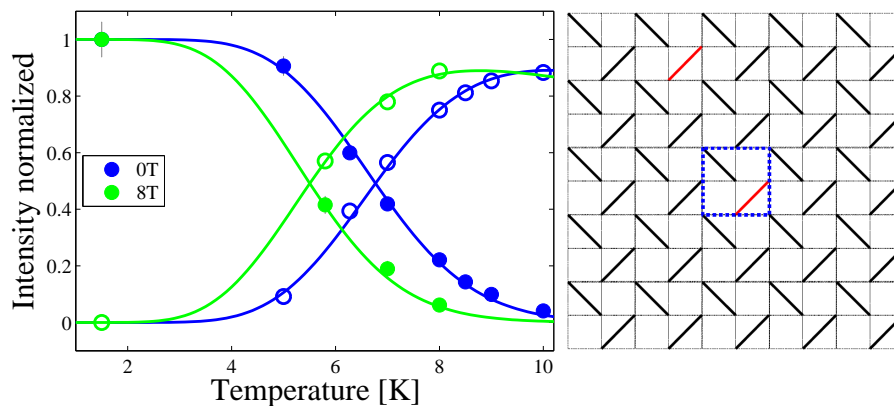


Figure 4.12: Left: Fit of broad (close symbols) and sharp (open symbols) damping intensities at 0 and 8 T  $Q=(1.5,0.5,0)$ . The lines are the probabilities  $P_s(T)$  and  $P_t(T)$  discussed in the text for  $N_u=21$  and  $\Delta=35$  K. Right: Sketch of the situation. The neutron excites a dimer to a the triplet state (red bond) in the presence of a thermal triplet (red bond) within about two unit cells (dashed blue) in each direction.

The simple calculation above offers a scale for how far the triplet inducing the decay can be: about 2 unit cells in each directions. This value also matches 8 T data without any

further modification, the shift to lower temperatures being accounted for by the different value  $n_s(T)$  takes in the presence of the field.

Alternatively the situation can be viewed considering that the presence of a triplet polarizes the neighboring dimers not leaving them in an exact singlet state. This ‘triplon’ extends over several dimers. If a neutron hits a singlet –creating a triplon– in a region far away from any thermal triplons a sharp excitation results. If the singlet is in the vicinity of a thermal triplon the excitation decays. The mathematical formulation of the probabilities is the same as before, and the interaction range is now understood as the distance between the triplons. Considering a 2D isotropic case, the 21 unit cell area found above corresponds to a triplon center to center distance of 2.6 lattice units (23 Å). We model the decay to occur when the two triplons overlap, so that their radius is 1.3 lattice units and they thus extend over an area of  $\sim 5$  unit cells (Fig. 4.13).

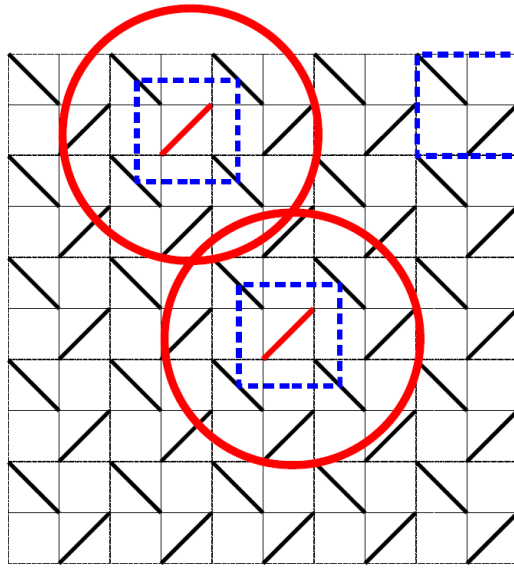


Figure 4.13: Two triplets (red bonds) polarize the neighboring singlets (black bonds) to create triplons whose extensions are given by the red circles. The decay is modeled to occur when the triplons overlap. The dashed blue lines indicate unit cells in the 2D Shastry-Sutherland lattice.

The results by Haravifard et al [66] for a doped  $\text{SrCu}_{2-x}\text{Mg}_x(\text{BO}_3)_2$  single crystal indicate that the introduction of a small percentage ( $x=2.5\%$ ) of non-magnetic impurities on the lattice increases the damping widths and causes them to remain finite even at base

temperature. This could indicate that a spin vacancy polarizes the neighboring singlets in an even more dramatic manner than the presence of a triplet.

## 4.6 Conclusion on the temperature dependence of $\text{SrCu}_2(\text{BO}_3)_2$

In conclusion we have measured the excitation spectrum on  $\text{SrCu}_2(\text{BO}_3)_2$  at finite temperatures by INS. The peak intensity of the 3 meV (35 K) excitation rapidly reduces and the excitation spectrum is flat already at 15 K. The integrated intensity however remains close to the one expected for a isolated dimer with a 35 K gap. The temperature dependent damping can be modeled by the sum of two DHO for each triplet mode, whereas a single DHO fails. One DHO remains resolution limited and corresponds to triplets not decaying. The second DHO broadens and corresponds to decaying triplets. As temperature increases the decay process becomes dominant. With a phenomenological microscopic model we can describe the situation as resulting from an interaction between two triplons which extend over the neighboring unit cells. The application of an external magnetic field accelerates the damping process and can simply be understood by the modification of the singlet-triplet densities.

Finally it is instructive to have a look at the low temperature ( $T \leq \sim 10$  K) structure of  $\text{SrCu}_2(\text{BO}_3)_2$ . It appears that some structural properties of  $\text{SrCu}_2(\text{BO}_3)_2$  are modified in two steps in that temperature range, very similarly to the change in damping regime we find around  $\sim 6.8$  K. Figure 4.14 shows the change in lattice constant and in linear expansion coefficient as function of temperature. As we shall see in Chap. 6 the lattice constants of  $\text{SrCu}_2(\text{BO}_3)_2$  are clearly affected upon entering the spin gap regime at  $T \sim 35$  K with an unusual increase in the unit cell volume. Around 7 K another puzzling behavior is observed with an abrupt change in slope of the linear expansion coefficient, reflected also in the temperature dependence of the lattice constants. It is very likely that at such low temperatures, it is the magnetic properties drive these structural effects. The change of slope in the linear expansion coefficient may thus well be related to the decay of triplets: the a axis lattice constant initially decreases quickly upon adding triplets up to  $\sim 7$  K



where the triplets have significant probabilities to decay which reduces the decrease of the lattice constant.

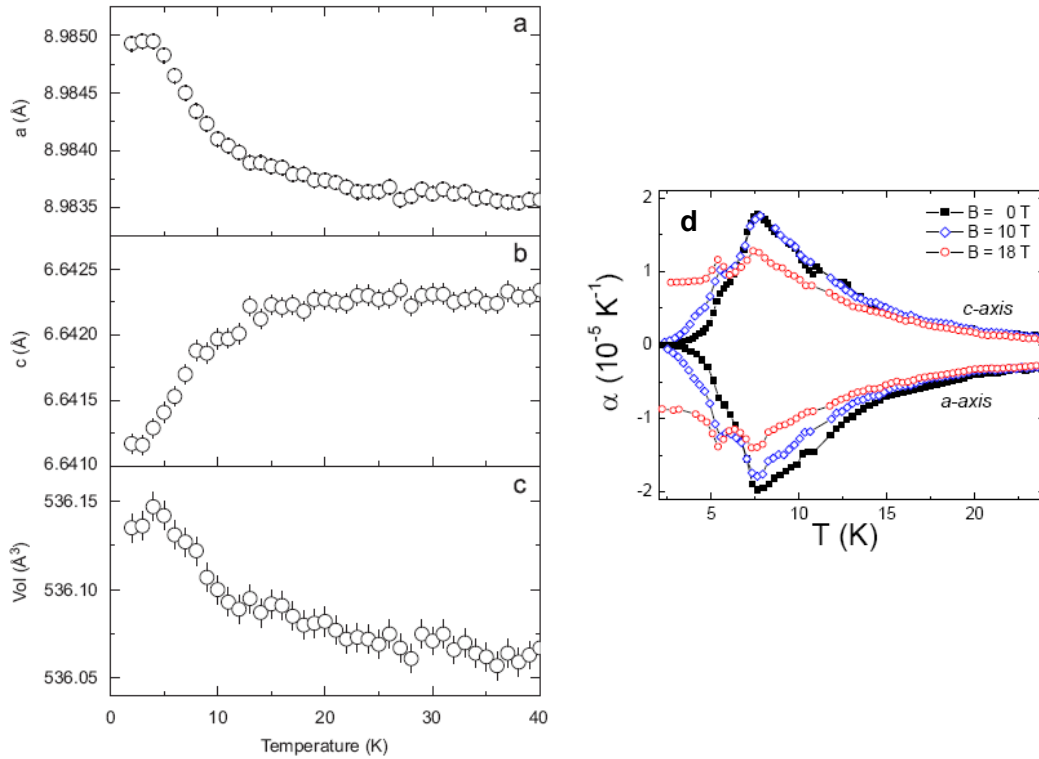


Figure 4.14: Structural modification in  $\text{SrCu}_2(\text{BO}_3)_2$  below 10 K. (a-c) a-axis, c-axis and unit cell volume resp. Reproduced from [26]. (d) Linear expansion coefficient as function of field. Reproduced from [91].



# Chapter 5

## Pressure induced quantum phases in $\text{SrCu}_2(\text{BO}_3)_2$

We present here inelastic neutron scattering (INS) results demonstrating that the Shastry-Sutherland compound  $\text{SrCu}_2(\text{BO}_3)_2$  can be tuned out of the exactly solvable singlet dimer ground state by application of hydrostatic pressure to a new disordered phase. The INS measurements are complemented by magnetic susceptibility up to 10 kbar and the critical pressure for the quantum phase transition is estimated around 18 kbar. The new discovered phase corresponds to the long sought after intermediary phase of the Shastry-Sutherland model and is identified as a plaquette phase. Elastic neutron scattering and X-ray diffraction at higher pressures show that  $\text{SrCu}_2(\text{BO}_3)_2$  eventually enters Neel long range order above 40 kbar, just before a structural monoclinic transition. INS experiments were performed on the triple axis instruments TASP at SINQ (Villigen-PSI, Switzerland), PANDA at FRM2 (Garching, Germany) and IN14 at ILL (Grenoble, France) using different pressure cells, instrument configurations and cryostats. The setups used are summarized in Table 5.1 together with those used for the elastic neutron experiments performed on IN8 at ILL and the synchrotron X-ray diffraction measurement at beamline ID9b of ESRF (Grenoble).

Setup	Instrument	Sample mass [g]	Pressure cell	Scattering plane	$k_f$ $\text{\AA}^{-1}$	Base T [K]
1	TASP <sup>+</sup>	3	HPCAL12	(1,2,0)-(0,0,1)	1.3	1.5
2	PANDA <sup>+</sup>	3	HPCAL17	(1,0,0)-(0,0,1)	1.5	1.5
3	IN14 <sup>+</sup>	3	HPCAL17	(1,0,0)-(0,0,1)	1.3	2
4	IN14 <sup>+</sup>	0.2	McWhan	(1,0,0)-(0,0,1)	1.5	2
5	IN14 <sup>+</sup>	0.2	McWhan	(1,0,0)-(0,0,1)	1.5	0.5
6	IN8 <sup>*</sup>	0.1	P-E	(1,1,0)-(0,0,1)	2.66	3.5
7	IN8 <sup>*</sup>	0.1	P-E	(1,0,0)-(0,1,0)	2.66	3.5
8	ID9b <sup>**</sup>	$\sim 10^{-6}$	DAC	(1,0,0)-(0,1,0)	15.148	$\sim 25$

Table 5.1: The different setups used for high pressure spectroscopy measurements. (+) INS: Instruments where operated with horizontally focused analyser. Tasp and IN14 have vertically focusing monochromator and Panda a double focusing monochromator. Base temperature of 0.5 K is achieved with a  $^3\text{He}$  cryostat in setup 5. Pressure is determined by the shift in lattice parameter of a Pb or NaCl reference to 0.7 kbar accuracy. (\*) Neutron diffraction: IN8 is operated with two PG filters and flat analyser. The Paris-Edimburg press (P-E) is cooled down to 3.5 K with a closed cycle displax. Pressure is determined trough the lattice constant of the lead matrix containing the sample. (\*\*) Synchrotron X-ray diffraction with diamond anvil cell (DAC) and He cryostat. Pressure is calibrated by the Ruby fluoresence method.

## 5.1 Previous experimental and theoretical results

Before presenting our results, we review some of the previous theoretical work related to the intermediary phase of the Shastry-Sutherland model and experimental results on  $\text{SrCu}_2(\text{BO}_3)_2$  under pressure.

The possible existence of an intermediary phase in the Shastry-Sutherland model and its nature have been discussed in Section 2.1.1. We point out here the work by Takushima et al [92] indicating the existence of two different low energy triplet excitations in the intermediary RVB plaquette-like phase obtained in their model (Fig.5.1 a). The nature of

these is understood in connection to the 1D orthogonal dimer chain where they correspond to a dispersionless four fold degenerate state leaving two diagonal spins free on a plaquette for the lower in energy and to a triplet excitation breaking a singlet on a plaquette for the higher (Fig.5.1 b). These two excitations are calculated to cross over at  $\alpha \sim 0.76$  in the 2D system before the plaquette gap goes soft at  $\alpha=0.86$ . Figure 5.1 c shows the results by Al Hajj and Malrieu [93] for columnar plaquette block energy calculated by a ‘renormalized excitonic method’ (REM) and Fig.5.1 d the results by Koga et al obtained by plaquette expansion calculation [12] suggesting the existence of a gapped plaquette like phase. These theoretical works give a quantitative value for the excitation energy in the dimer and the intermediary phase and shall be compared to our experimental findings.

On the experimental side, in parallel to the neutron work presented in this thesis, several other experiments have been reported. Magnetic susceptibility [94] and ESR [95] to moderate pressures ( $p \leq 12$  kbar) indicate a softening of the gap. The combined effect of pressure and field was also measured by susceptibility and NMR [44]. In the latter case magnetic order occurring at 24 kbar and 7 T on a fraction of the dimers was proposed. The main results are show in Fig.5.2. From the structural point of view, at room temperature, a transition from the ambient  $I\bar{4}2M$  tetragonal space group to monoclinic was observed at 47 kbar and a second transition to an unidentified phase at  $\sim 150$  kbar [28].

## 5.2 Magnetic susceptibility up to 10 kbar.

Magnetic susceptibility up to 10 kbar was measured in a SQUID by collaborators in the U.K.<sup>1</sup>. Given that the magnetic signal of the pressure cell is by far larger than the signal from the sample, such measurements require accurate background subtraction. Figure 5.3 shows final results. The susceptibility peak shifts to lower temperatures, as pressure increases suggesting a reduction of the spin gap in accordance with the results of Fig.5.2. We performed quantitative fits of  $\chi(p, T)$  by 20 sites exact diagonalization<sup>2</sup> which allowed us to quantify the gap reduction and to extract the pressure dependence of the individual couplings  $J$  and  $J'$ . Both couplings decrease linearly up to 10 kbar. Since these

---

<sup>1</sup>Ch. Rüegg, Ch. Panagopoulos, S. S. Saxena, M. Ellerby and A. Magee.

<sup>2</sup>The exact diagonalization data have been computed by A. Läuchli.

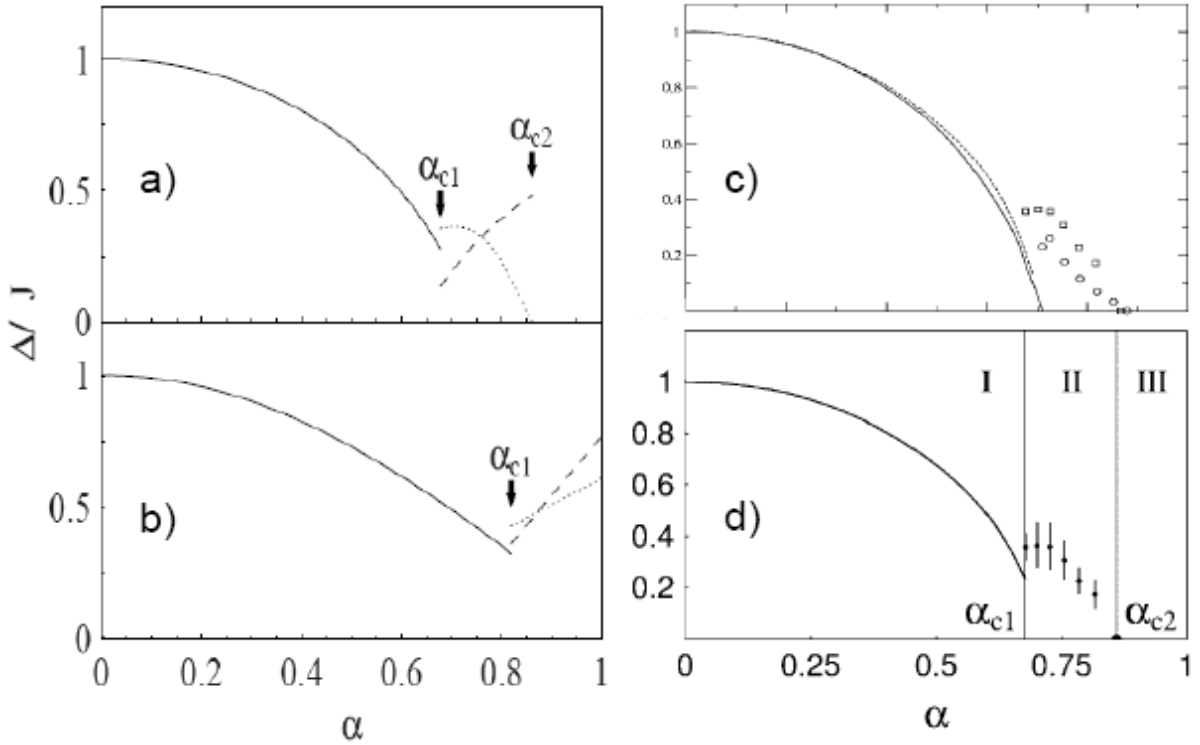


Figure 5.1: Excitation energies in the dimer and plaquette phases. (a) 2D Shastry-Sutherland model and (b) 1D orthogonal dimer chain. The full line is the singlet-triplet gap in the dimer phase, the dotted line a triplet excitation on the plaquette and the dashed line the four fold degenerate state discussed in the text. Reproduced from [92]. (c) The REM gap (full line) and columnar plaquette block energies (circles) compared to a dimer expansion calculation (dashed line) [10] and plaquette expansion (squares) [12]. Reproduced from [93]. (d) Dimer expansion calculation (full line) [10] and plaquette expansion (symbols) as in (c) with error bars on the symbols. Reproduced from [12].

pressures correspond to small displacement of the atomic positions, it seems reasonable to extrapolate the linear dependence to higher pressures. Since  $J$  has the larger slope,  $\alpha$  increases with pressure, consistent with the system getting closer to the first quantum critical point. After presentation of the INS measurements in the next sections, we shall compare and combine the results from these two techniques to obtain the phase diagram of  $\text{SrCu}_2(\text{BO}_3)_2$ . The extraction of  $\alpha(p)$  (Fig.5.3 right) by magnetic susceptibility will also enable to compare experimental INS results given as a function of pressure to the theoretical calculations given as a function of  $\alpha$ .

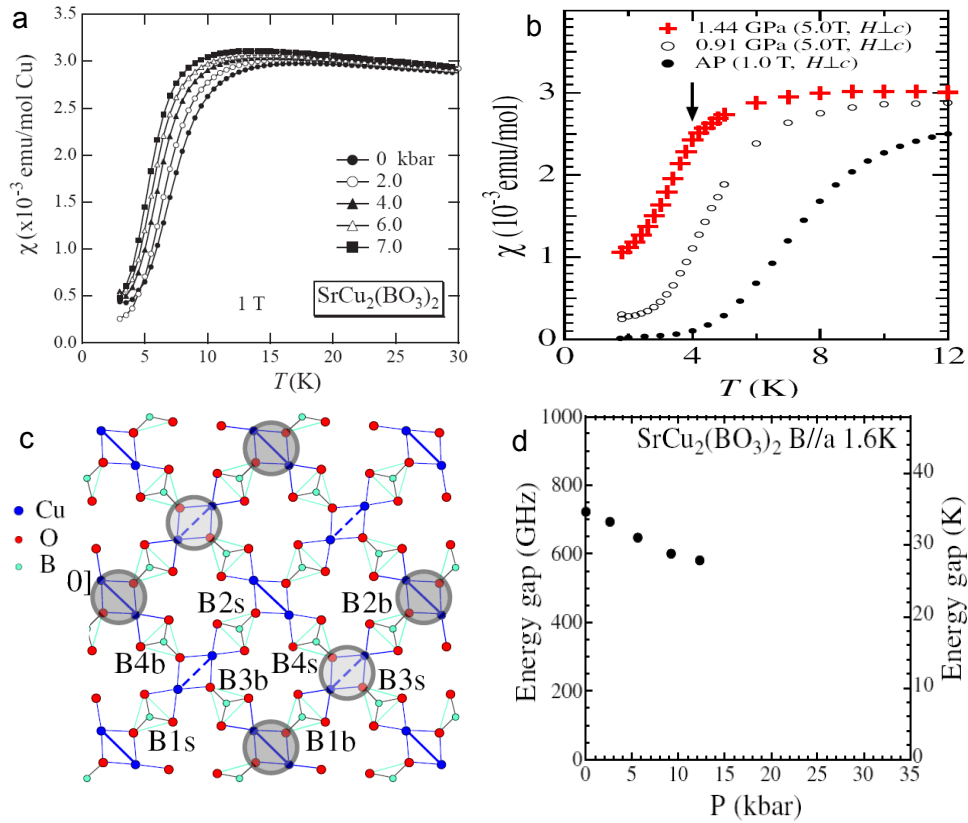


Figure 5.2: Measurements of  $\text{SrCu}_2(\text{BO}_3)_2$  under pressure. (a) and (b) Magnetic susceptibility, showing a possible kink in (b) at 16 kbar and 5 T. Reproduced from [94] and [44]. (c) Possible magnetic ordering at 24 kbar and 7 T, observed by NMR. The shaded regions indicate magnetic dimers. Reproduced from [44]. (d) Spin gap extracted by ESR. Reproduced from [95].

### 5.3 Inelastic neutron scattering up to 22 kbar

We measured the excitation spectrum of  $\text{SrCu}_2(\text{BO}_3)_2$  with setup 1 (Table 5.1) on the triple axis instrument TASP. 12 kbar was about the limit, at the time, for high pressure INS with a sample volume of the order of  $1 \text{ cm}^3$ . Figure 5.4 shows the first results we obtained by application of hydrostatic pressure on  $\text{SrCu}_2(\text{BO}_3)_2$ . The spin gap is reduced in energy from ambient  $\sim 3 \text{ meV}$  to  $\sim 2.2 \text{ meV}$  at 12 kbar. The analysis of the dispersion and structure factor Fig.5.5 demonstrates the system remains in the original dimer phase, with a reduced energy scale. The dispersion only slightly increases with pressure, which could be understood by the increase of  $\alpha$  [10]. The fact that the gap energy *reduces* upon

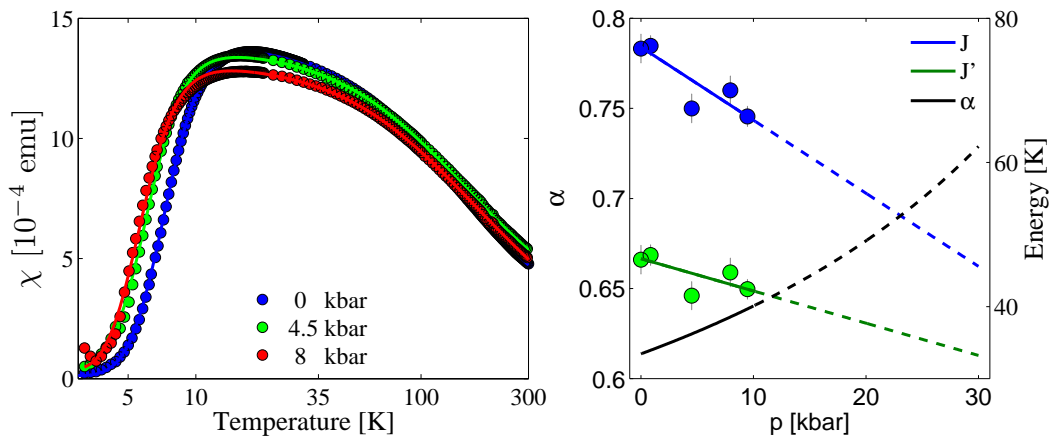


Figure 5.3: Left: Magnetic susceptibility of  $\text{SrCu}_2(\text{BO}_3)_2$  under pressure (log scale), full line are fits to 20 sites exact diagonalization data. Right: the extracted pressure dependence of nearest neighbor coupling  $J$ , the next nearest neighbor coupling  $J'$ , and of the ratio  $\alpha = J'/J$  with linear fits for  $J$  and  $J'$  (full lines) extrapolated above 10 kbar (dashed lines).

application of pressure is a sign that pressure brings the system closer to the quantum phase transition. The ground state should *at the latest* be modified when the excited triplet goes completely soft. It is also very possible that the quantum phase transition will take place before the the gap energy vanishes as proposed in the scenarios of Section 5.1, where a first order transition to the intermediary phase is expected before the dimer gap closes. The measurement also shows that pressure softens the three quasi-degenerated triplet modes [46] alike. This is different to the application of a magnetic field, which Zeeman splits the three modes, reducing the energy of the lower one only. One notices the intensity of the excitation is strongly reduced, which is likely to relate to the reduction of the gap energy. Knowing the unusual temperature dependence of  $\text{SrCu}_2(\text{BO}_3)_2$  (see previous chapter) where the peak intensity of the INS excitation is reduced by half around 6 K for a 3 meV gap, it is possible that for a smaller value of the gap the damping of triplets is already important around 1.5 K.

The conclusion of this first experiment is thus that pressure may bring the system to the quantum phase transition, but that higher pressures than the (at the time) available 12 kbar are needed. Besides, given the reduction in peak intensity, the observation of the bound-states (or even of the gap at higher pressures) will only be achievable on



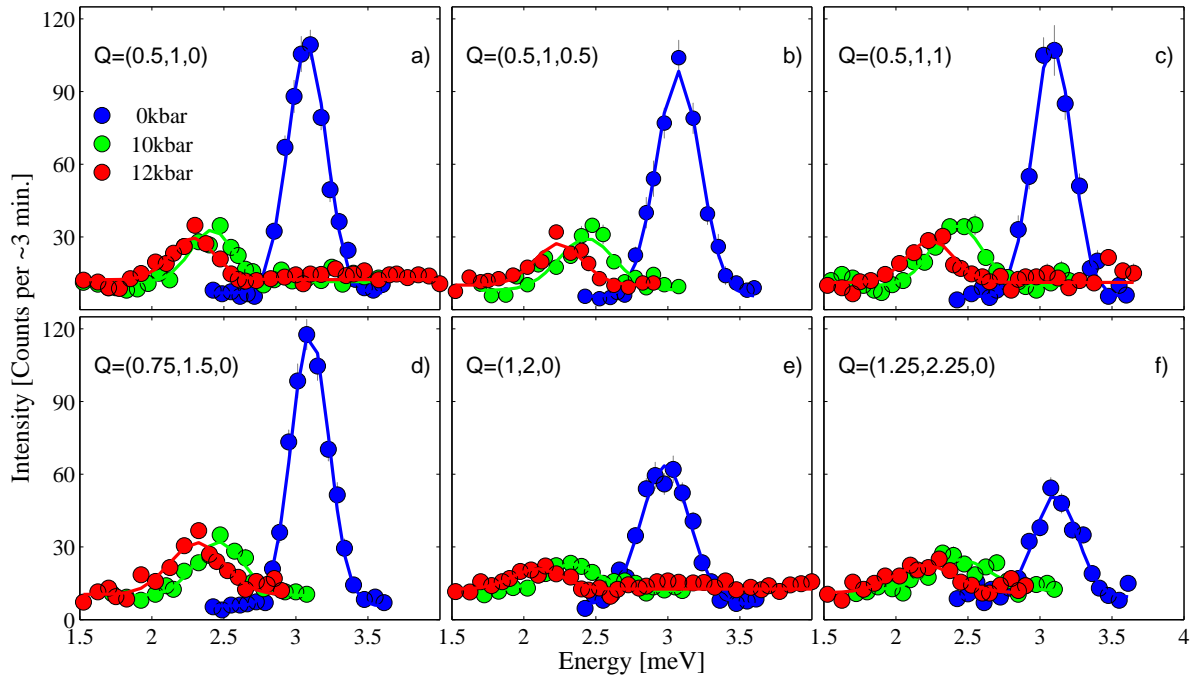


Figure 5.4: INS energy scans on TASP at different Q points and pressures. (a-c) Out of plane dependence. (d-f) In plane dependence.  $T=1.5$  K,  $k_f=1.3 \text{ \AA}^{-1}$ .

instruments with higher flux like IN14 or Panda.

To further increase the pressure range a new large volume aluminium-steel piston cylinder cell reaching 17 kbar (HPCAL17) was developed (see Chap. 4). It was used on the triple axis instruments Panda and IN14 with setups 2 and 3. Even higher pressures can only be explored with much reduced sample size and the range 16-22 kbar was studied with a McWhan cell on IN14 with setups 4 and 5.

Figure 5.6 shows energy scans performed on Panda with the HPCAL17 pressure cell. Both the gap and the bound triplet can be observed. The measured gap  $\Delta$  is consistent with the results of Fig 5.4, and the bound triplet energy is also reduced by application of pressure. The structure factor at the three pressures remains identical as shown by the Q scans in Fig.5.7, indicating the dimer phase still survives at 14.5 kbar.

Figure 5.8 shows high quality energy scans performed on IN14 with the same pressure cell. As observed in the first experiment both the gap energy and intensity strongly reduce upon application of pressure. No out of plane dependence is observed, although in  $\text{SrCu}_2(\text{BO}_3)_2$  the c-axis is softer resulting in reduced interlayer distances at high pressures [28]. Com-

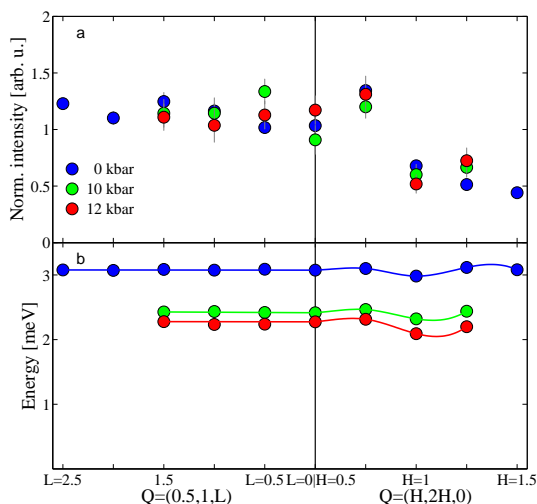


Figure 5.5: Structure factor (top) and dispersion (bottom), obtained by Gaussian fits to the spectra of Fig.5.4. Intensities are normalized. Lines are guides to the eye.

binning the different results in Fig.5.9, it can be seen that in the pressure range 0-15 kbar, the softening is linear with a slope of  $0.075(5)$  meV/kbar and is essentially  $Q$ -independent, with no signs of a new quantum phase. Interestingly however, the triplet binding energy,  $\delta = 2\Delta - E_{BT} = 1.19(2)$  meV remains pressure independent, so that the bound triplet energy  $E_{BT}$  softens twice as fast  $0.143(7)$  meV/kbar. The pressure dependent gap obtained through the  $Q=0$  expansion of Ref. [13] from the susceptibility couplings  $\Delta(J_\chi(p), J'_\chi(p))$  is in very good agreement with the direct INS gap measurement  $\Delta_Q(p)$ . To take into account the small  $Q$ -dependence of  $\Delta_Q$ , we consider  $\Delta_Q(p) = \Delta(J_\chi(p), J'_\chi(p)) + D_Q(p)$ , where the dispersion factor  $D_Q$  is of the order of 2 K. When extrapolating  $\Delta_Q(p)$  to higher pressures, the gap would close around 31 kbar for  $Q=(2,0,L)$  (lines in Fig.5.9). However the two triplet bound state (BT) would go soft before  $\Delta$ , around 27 kbar, with BT becoming energetically favorable around 20 kbar when considering the finite dispersion. At this crossover a cascade mechanism could trigger the transition to a new quantum phase, much differently than a direct AFM ordering upon closure of the gap, and be at the origin of the existence of the intermediary phase.

The instability of the bound state has been discussed in Ref. [96] where the gap is calculated to close at  $\alpha \simeq 0.7$  and one of the  $s=1$  bound states at  $\alpha \simeq 0.63$  with the crossover between the one and two triplet energies taking place just before. Our experimental

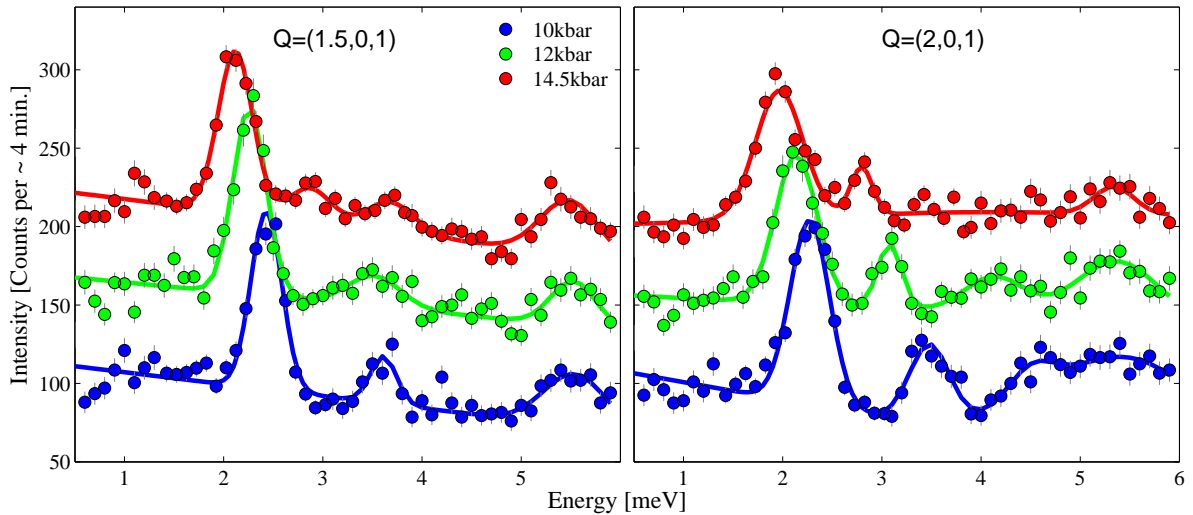


Figure 5.6: INS energy scans on PANDA at different Q points and pressures. Data is shifted on the y-axis for clarity (+50 and +100 for 12 and 14.5 kbar resp.). Solid lines are Gaussian fits.  $T=1.5$  K,  $k_f=1.5 \text{ \AA}^{-1}$ .

results indicate a higher  $\alpha$  value (0.685) for the crossover and no acceleration of BT softening in the  $0 \leq p \leq 15$  kbar where it was possible to observe it. Using setups 4 and 5 we discovered the first evidence of  $\text{SrCu}_2(\text{BO}_3)_2$  entering a new quantum phase between 16 and 21.5 kbar, as a discontinuity in the gap softening occurs. The spectra at these two pressures for  $Q=(1.5,0,1)$  (Fig.5.10) and  $(2,0,0)$  (Fig.5.11 a) look extremely similar with  $\Delta \simeq 2$  meV unchanged, while the shift in lattice parameters of the sample and of the NaCl reference definitely indicate an increased pressure. The observation of such a discontinuity in the gap softening could correspond to the calculations of Fig.5.1 where the intermediary plaquette phase is gapped. The fact that the gap energies at 16 and 21.5 kbar are identical could simply be accidental given that they are, a priori, expected to be close on both sides of the critical point. The structure factor, measured by a Q scan along  $(H,0,1)$ , is however also identical to the ambient pressure singlet-triplet structure factor of  $\text{SrCu}_2(\text{BO}_3)_2$ . We shall see that this can be understood in terms of a new plaquette phase where we calculate that one of the excited states is actually expected to display such a structure factor. The transition to a new quantum phase is further proven by a new type of excitation suddenly appearing at the higher pressure (Fig.5.10 c and 5.11 c-d). It is clearly visible around 1 meV for  $Q=(1,0,1)$ ,  $(-1,0,1)$  and  $(1,0,1.5)$  at 0.5 K

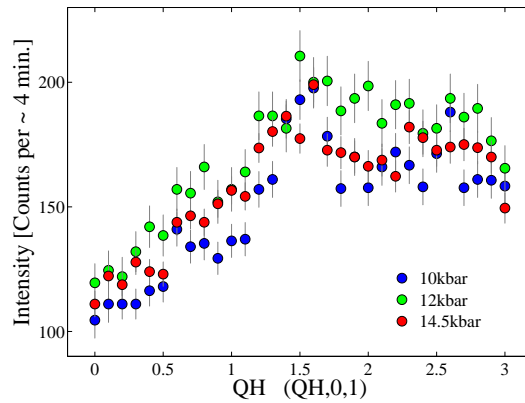


Figure 5.7: Structure factor at different pressure. Combined constant energy scans at resp. 2.4-2.5 meV (10 kbar), 2.1-2.2 meV (12 kbar), and 1.95-2.00-2.05-2.10 meV (14.5 kbar).

and is not observed at 15 K, which indicates a magnetic origin. We label the new low energy excitation LE and keep the  $\Delta$  label for the 2 meV excitation. The high pressure spectra at different Q points are shown in Fig.5.11 where one can notice that no change in intensity occurs for  $\Delta$  between 2 K and 0.5 K. The dispersion and structure factor of these two excitations are shown in Fig.5.12. LE is more dispersive than  $\Delta$ :  $\sim 0.5$  meV in the measured Q-range. It also has a completely different structure factor strongly peaking at  $Q=(1,0,1)$ .  $\Delta$ , consistent with the Q-scan of Fig.5.10, is indistinguishable from the singlet-triplet gap in the dimer phase.

To summarize the experimental results up to 21.5 kbar,  $\Delta$ , BT and LE are plotted as a function of pressure in Fig.5.13 for some Q points. It can be seen that the gap softening in the 0-15 kbar range is suddenly interrupted at higher pressure, and that LE has a lower energy than the extrapolated dimer phase triplet excitation.  $\Delta$  on the other hand is higher than the expected dimer gap at 21.5 kbar. It is thus clear that above a certain critical pressure in the 16-21.5 kbar interval, the spectrum is strongly modified, reflecting a new ground state in the system. Since we have no other experimental data points in the 16-21.5 kbar interval, we can only notice that it corresponds to the low range of the calculated critical  $\alpha$  in the Shastry-Sutherland model. For instance,  $\alpha_c=0.67$  as calculated in Ref. [14] would correspond to a critical pressure  $p_c=18.3$  kbar indicated by the dashed vertical line.

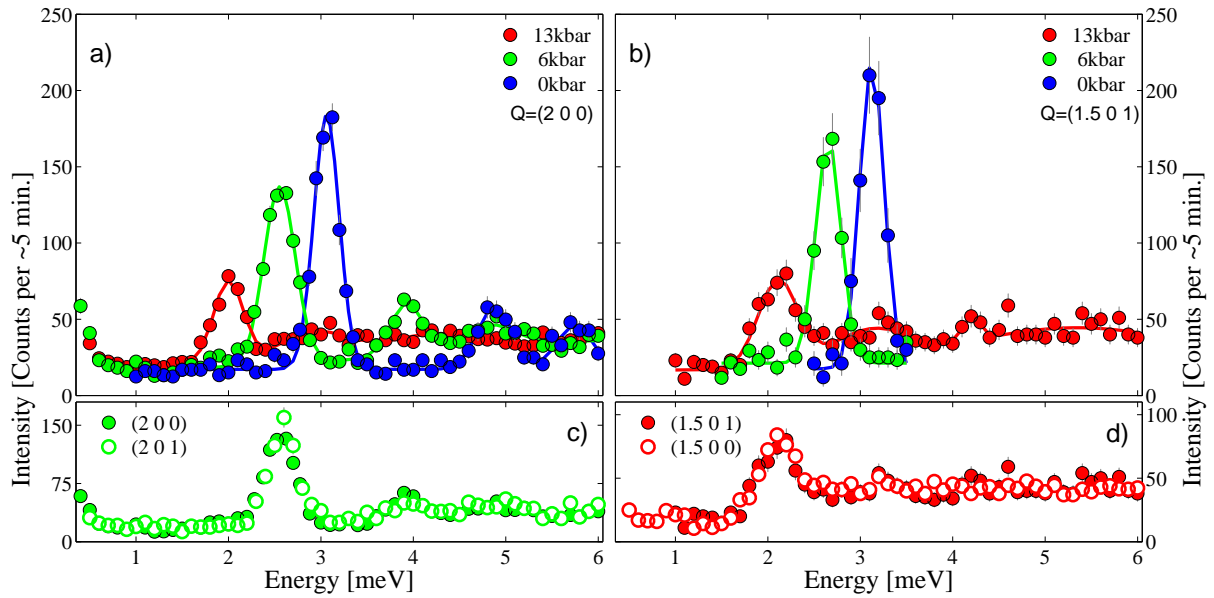


Figure 5.8: INS energy scans on IN14 at different Q points and pressures. in (a-b) the solid lines are Gaussian fits. (c-d) show the out of plane Q-dependence of the spectrum.  $T=2$  K,  $k_f=1.3 \text{ \AA}^{-1}$ .

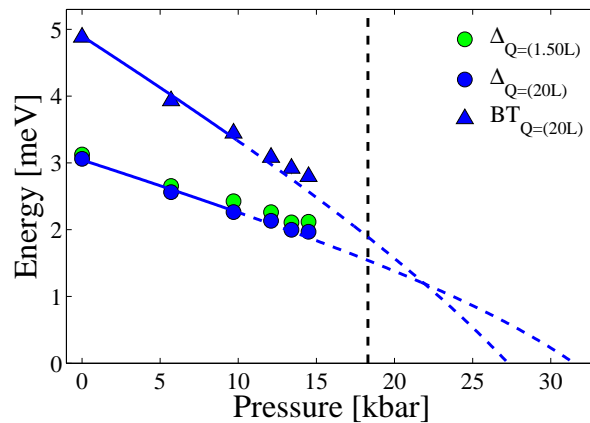


Figure 5.9: Summary of the pressure dependence of the gap and BT energies as a function of pressure up to 15 kbar. Data are for  $L=0$  and  $L=1$  which have been combined. The full line is the combined fit of INS and magnetic susceptibility  $\Delta(J_\chi(p), J'_\chi(p)) + D_{20L}(p)$  discussed in the text and the dashed line its extrapolation to higher pressures. The vertical dashed line is a possible quantum critical point [14] corresponding to  $\alpha=0.67 \leftrightarrow p=18.3$  kbar.

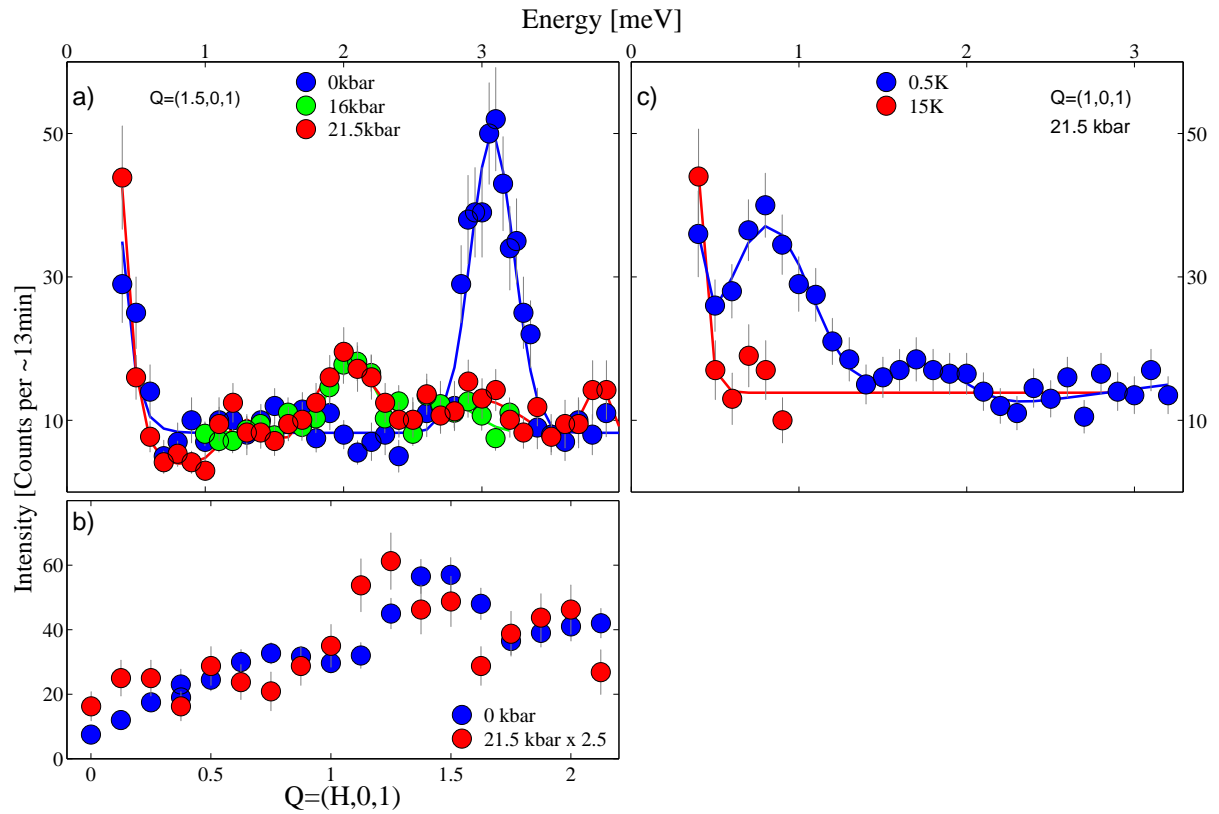


Figure 5.10: (a) Energy scans at 0, 16 and 21.5 kbar measured on IN14, setup 4,  $T=2$  K. (b) Q-scan on the peak maxima at ambient pressure ( $E \sim 3$  meV) and 21.5 kbar ( $E \sim 2$  meV), setups 4 and 5. (c) Energy scan at  $Q=(1,0,1)$  at 21.5 kbar as a function of temperature, setup 5.

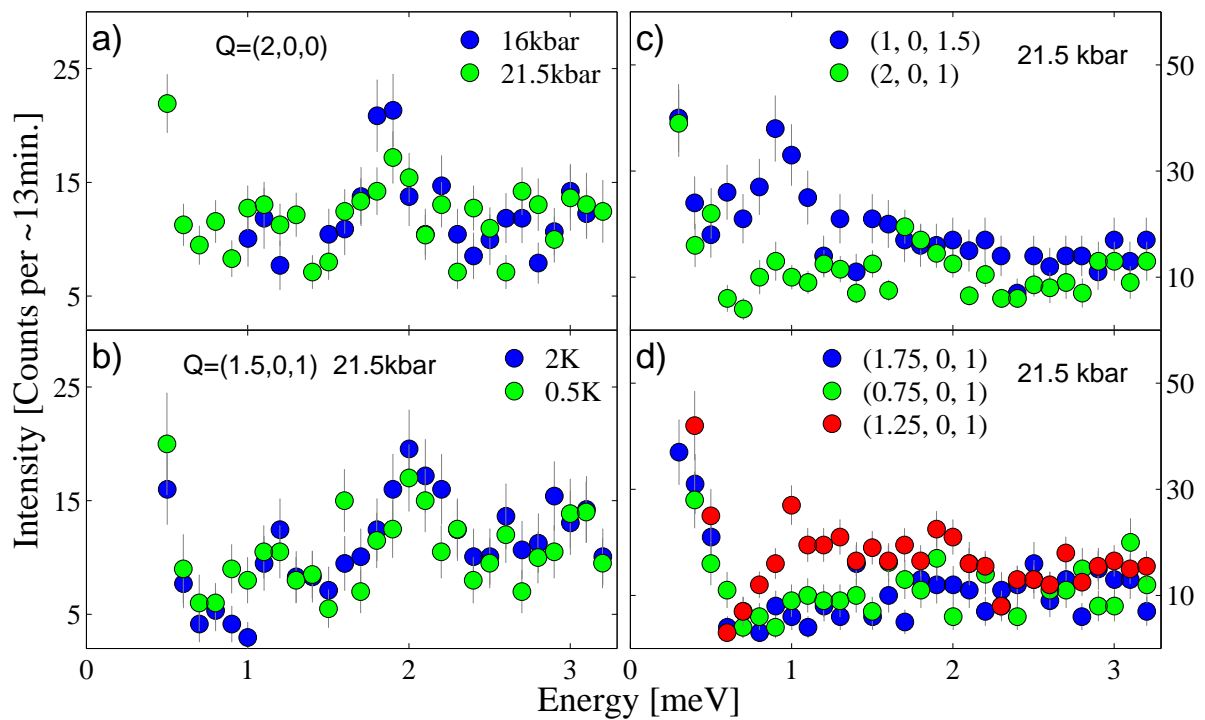


Figure 5.11: INS energy scans on IN14 at different Q points, pressures and temperatures. (a) Pressure dependence of  $\Delta$ . (b) Temperature dependence of  $\Delta$ . (c-d) New low energy feature LE visible at  $Q=(1,0,1.5)$  and  $Q=(1.25,0,1)$ , note that for the latest both  $\Delta$  and LE have intensity.

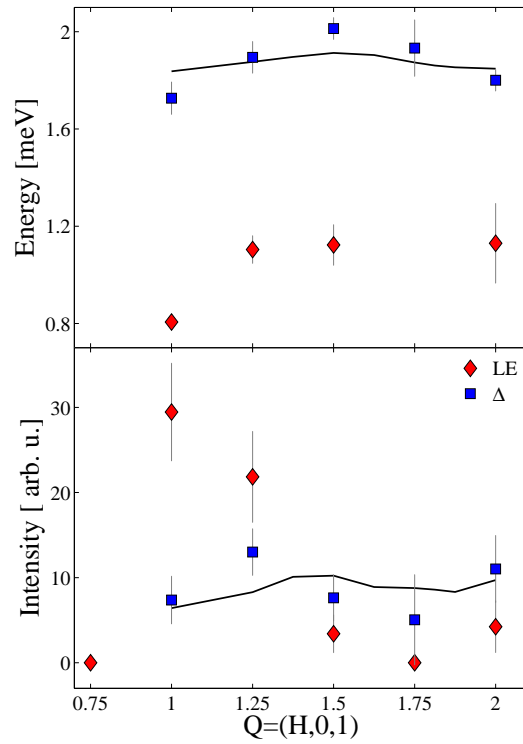


Figure 5.12: Dispersion (top) and structure factor (bottom) of  $\Delta$  and LE at 21.5 kbar obtained by Gaussian fits to the energy scans. The full line are scaled dispersion and structure factor of the singlet-triplet gap at ambient pressure for  $(H,0,0)$  extracted and adapted from Ref. [35].

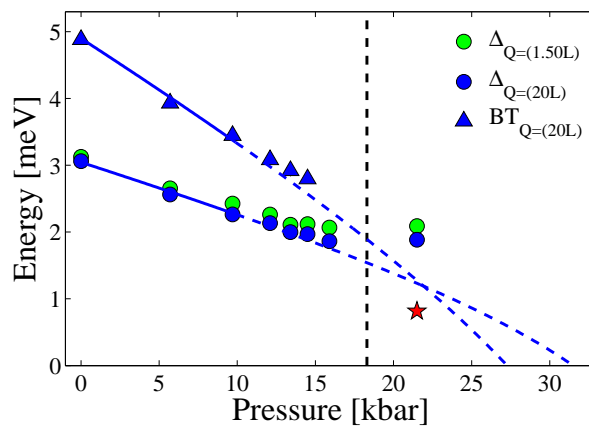


Figure 5.13: Summary of the pressure dependence of the gap and BT energies as a function of pressure up to 21.5 kbar. Lines and symbols are identical to Fig.5.9. The  $\star$  indicates LE for  $Q=(1,0,1)$ .



## 5.4 Identification of the new phase

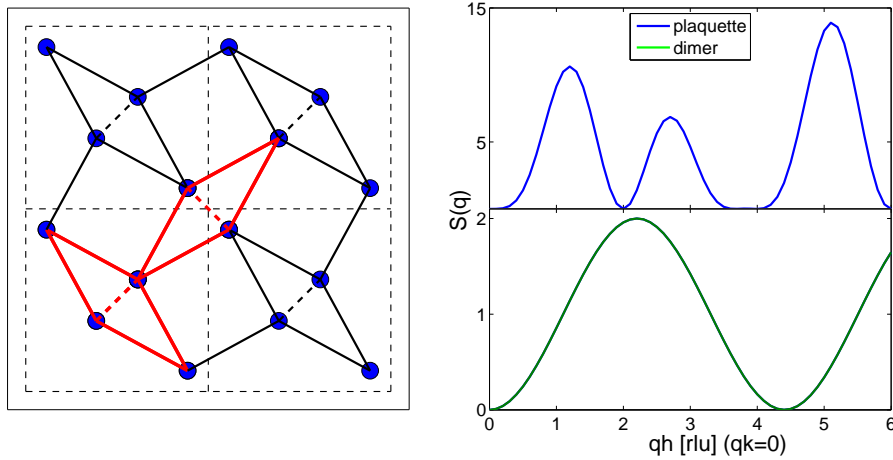


Figure 5.14: Left: Plaquette in the  $\text{SrCu}_2(\text{BO}_3)_2$  geometry. The two red plaquettes are used to compute the structure factor, the unit cells are indicated by the dashed lines. Right: (Top) Structure factor of the triplet excitation in the plaquette. (Bottom) Structure factor of the quadruplet identical to the structure factor of two dimers.

We have considered different possibilities for the new discovered phase including a mixed dimer and plaquette state. Since  $\Delta$  is reminiscent of the dimer gap, a mixed phase could possibly explain the experimental observation and such phases (mixed columnar and plaquette dimers) have recently been pointed out by theoretical works in some quantum dimer model [97]. However the existence of a mixed phase has never been suggested for the Shastry-Sutherland model to our knowledge. We finally find that the simplest physical interpretation of the new high pressure phase in  $\text{SrCu}_2(\text{BO}_3)_2$  is a plaquette phase on the plaquettes containing a diagonal bond. The study of the excitation spectrum and structure factor of the isolated plaquette is detailed in Appendix B. The ground state is a  $s=0$  singlet and there is a triplet excited state and a four-fold degenerate state corresponding to a singlet on the diagonal plus two free spins. The triplet state has a structure factor peaking around  $Q=(1,0)$  in the 2D geometry of  $\text{SrCu}_2(\text{BO}_3)_2$  and the quadruplet<sup>3</sup> has a structure factor identical of to that of an isolated dimer on the diagonal bond. The isolated plaquette with diagonal bond thus displays the main characteristics of the new

<sup>3</sup>Only the transitions to the three  $s=1$  states of the quadruplet can be observed by INS, not the fourth one that is a transition between two  $s=0$  states and is thus forbidden in spin-only magnetic scattering.

high pressure phase:

- 1) a non-magnetic gapped ground state
- 2) a low energy triplet with structure factor peaking at  $Q=(1,0)$
- 3) an other low energy excitation with structure factor identical to the singlet-triplet in the exact dimer phase.

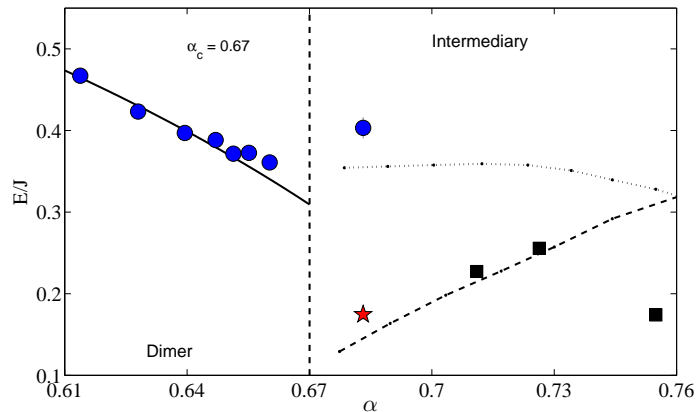


Figure 5.15: Experimentally determined excitation energies in  $\text{SrCu}_2(\text{BO}_3)_2$  compared to theoretical predictions. The color symbols are our experimental results defined as before. The dotted lines are calculation from Ref. [92] for the low lying triplet excitations in a plaquette state, and the black squares are the columnar plaquette block energies from Ref [93] (see Fig.x5.1).

To analyze the extended system, we plot in Fig.5.15 the energy  $E/J$  vs  $\alpha$  which enables a direct comparison between our results and the calculations for the low and high energy plaquette triplets [92], and columnar plaquette energy [93]. We find first that the series expansion for the gap as a function  $\alpha$  [10] (black line) that we use to compute the gap from the susceptibility fits, matches the direct INS measured gap quite well in the dimer phase. Beyond the quantum critical point, there is qualitative agreement for the energy scales, in particular the energy of LE is close to the expected low energy plaquette excitation of Takushima et al [92]. In their work the two excitations are understood in connection to the 1D orthogonal dimer chain where they correspond to a state leaving two diagonal spins free on a plaquette for the lower in energy and to a triplet excitation breaking a singlet on a plaquette for the higher. Our experimental results indicate however that the low energy excitation is more dispersive than the high energy feature, which is the opposite

of what they obtain. The calculation of Takushima et al is thus likely<sup>4</sup> to correspond to our experimental observation provided the two low energy states are inverted.

Finally our results could also explain the magnetic ordering proposed by NMR measurement at 24 kbar and 7 T: the new spin  $s=1$  excitation LE being low in energy (0.5 meV), a 7 T field is sufficient to close it and to obtain a magnetic ground state.

## 5.5 Neutron and X-ray diffraction

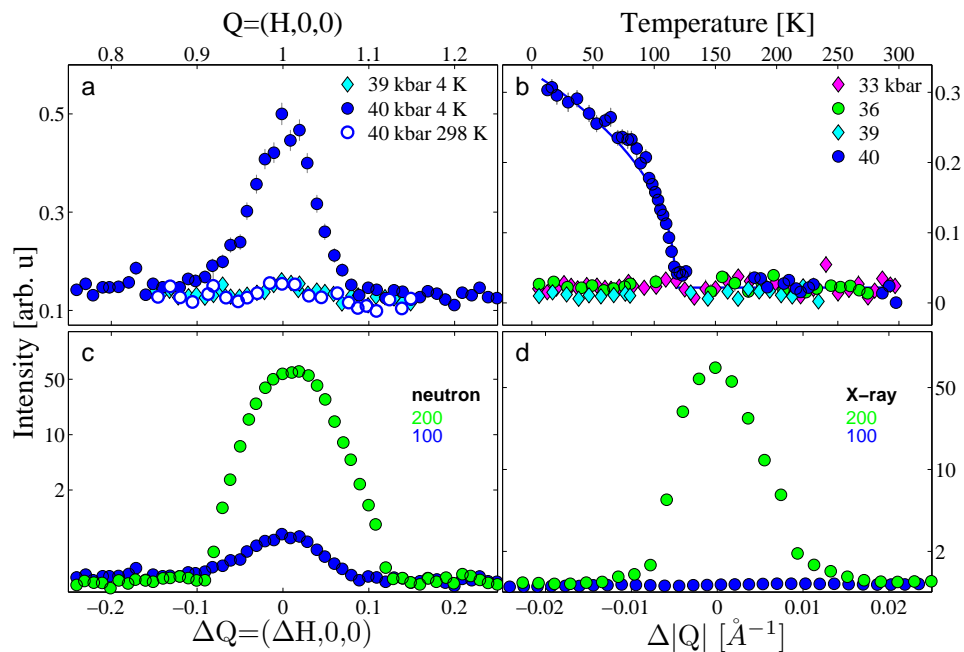


Figure 5.16: High pressure magnetic Bragg peak in SrCu<sub>2</sub>(BO<sub>3</sub>)<sub>2</sub>. (a) Nuclear forbidden  $Q=(1,0,0)$  peak at 39 and 40 kbar, from neutron diffraction. (b) Temperature dependence of the  $Q=(1,0,0)$  peak intensity. Full line is a power law fit giving a critical exponent of 0.43. (c) Relative intensity (log scale) of  $Q=(2,0,0)$  and  $Q=(1,0,0)$  at 40 kbar 4 K from neutron diffraction. Setups 6 and 7. (d) Same reflections from X-ray diffraction at 42 kbar 34 K, setup 8.

We now turn to the higher pressure range  $20 \leq p \leq 60$  kbar in which SrCu<sub>2</sub>(BO<sub>3</sub>)<sub>2</sub> eventually enters an antiferromagnetic ordered phase. Elastic neutron diffraction was performed in the opposed anvils Paris-Edinburgh press on the thermal triple axis instrument IN8

<sup>4</sup>The structure factors are not given in the article.

operated with setups 6 and 7 (see Table 5.1). At 40 kbar and 118 K a new type of Bragg reflections suddenly appears (Fig.5.16). These are  $Q=(1,0,0)$  type peaks ( $H+K+L=\text{odd}$ ) that are nuclear forbidden from the centering of the  $\bar{I}42M$  space group. The intensity of the forbidden reflections smoothly increases upon cooling to reach its maximum at low T. The relative  $(2,0,0)$  to  $(1,0,0)$  peak intensity is about  $\sim 200$ . In contrast these peaks appear abruptly as a function of pressure as they were not observed at 36, 38 nor 39 kbar down to 4 K. The transition is fully reversible upon temperature increase and no significant hysteresis is observed. At higher pressures the transition temperature is hardly modified: 123 K at 55 kbar. At 47 kbar and ambient temperature Loa et al [28] have observed a structural monoclinic distortion. It is however clear for two reasons that the new Bragg peaks we describe are not directly related to this distortion: 1) they appear at lower pressure and the transition temperature remains below ambient at pressures both higher and lower than 47 kbar, 2) the monoclinic transition would not result in these new reflections but rather in the splitting of allowed peaks into non equivalent reflections.

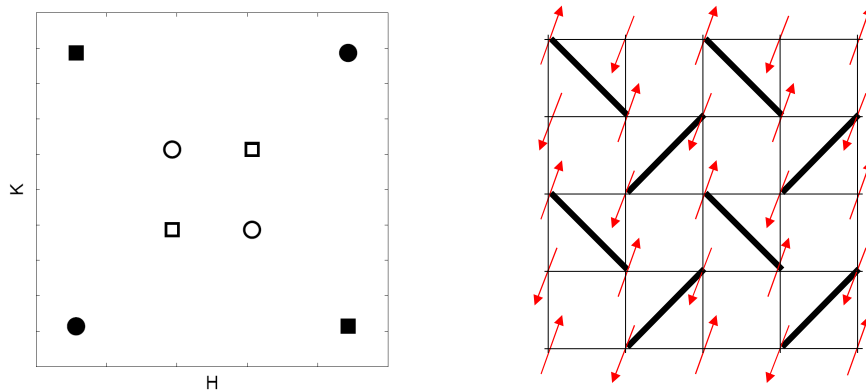


Figure 5.17: Neel order in  $\text{SrCu}_2(\text{BO}_3)_2$  at high pressure. Left: View of the two  $\text{Cu}^{2+}$  layers in  $\text{SrCu}_2(\text{BO}_3)_2$ . Squares (circles) represent the ions in the upper (lower) layer. Full symbols are spin up and empty symbols spin down. Right corresponding Neel order on the extended Shastry-Sutherland lattice (the absolute orientation of the spins is chosen arbitrarily).

The magnetic nature of these Bragg reflections was checked in a high pressure diamond anvil cell synchrotron measurement on beamline ID9b at ESRF using setup 8. No peaks of the  $(1,0,0)$  type were observed at any pressure or temperature in the 0-180 kbar and 300-25 K range. This is a clear sign for the magnetic origin of these reflections since X-rays

are only sensitive to structural order whereas neutrons are sensitive to both structural and magnetic order. The (1,0,0) peaks can be understood as simple Neel order with a magnetic cell of the same size as the conventional chemical cell. The extinction of (1,0,0) peaks due to body centering (I symmetry) does not apply in the magnetic cell, where they are two types of inequivalent Cu ions with spin up and down. Figure 5.17 left shows the projection along the c-axis of the Neel ordered magnetic cell. It contains two magnetic layers (circles and squares), within which orthogonal dimers have opposite spin orientation (full and open symbols). This ordering corresponds to the expected AFM long range order on the Shastry-Sutherland lattice (Section 2.1.1). The strong antiferromagnetic coupling  $J$ , cannot prevent the two spins within one dimer to be ferromagnetically aligned for large enough values of  $\alpha$ . The magnetic ordering is thus the same as for the simple square lattice ( $J=0$ ) Neel order. The absolute orientation of the spins could not be fully obtained. However, considering the tetragonal symmetry of  $\text{SrCu}_2(\text{BO}_3)_2$  and the fact that the neutron can only probe the component of the magnetic moment perpendicular to  $Q$ , two types of high symmetry orientations are possible: one with spins pointing out of the magnetic plane along  $[0,0,\pm 1]$  and the other one with spins pointing in-plane along one of the diagonals  $[\pm 1,\pm 1,0]$ . The monoclinic distortion could be traced down as a function pressure and temperature and magnetic ordering is observed both in the tetragonal and monoclinic regions. Due to the reduction of symmetry in the monoclinic phase one could expect the orientation of the spins to be different in that structural phase. We also note here, that beyond the monoclinic distortion the dimers are not constrained by symmetry to remain orthogonal and the system is no longer described by the Shastry-Sutherland model. The structural part of this study shall be presented in the next chapter.

## 5.6 Conclusion on the pressure induced quantum phases in $\text{SrCu}_2(\text{BO}_3)_2$

In summary the combination of INS, X-ray and neutron diffraction, and magnetic susceptibility measurements enabled us to identify the pressure induced quantum phases in  $\text{SrCu}_2(\text{BO}_3)_2$ . The dimer phase survives up to  $18(\pm 2)$  kbar. Beyond that,  $\text{SrCu}_2(\text{BO}_3)_2$

enters a new non magnetic gapped phase which corresponds to the formation of a plaquette ground state on the plaquettes containing a diagonal bond. The extraction of the coupling parameters by fits to magnetic susceptibility shows that the increase of pressure implies an increase of  $\alpha$  and that the critical pressure is close to the calculated critical coupling ratio. As pressure is increased further, the plaquette gap may eventually close and the system is observed to order antiferromagnetically at 40 kbar with a high Neel temperature of 118 K. Shortly after the magnetic ordering, pressure produces a structural monoclinic distortion which relieves the next nearest neighbor frustration bringing  $\text{SrCu}_2(\text{BO}_3)_2$  beyond the original orthogonal dimer Shastry-Sutherland model.

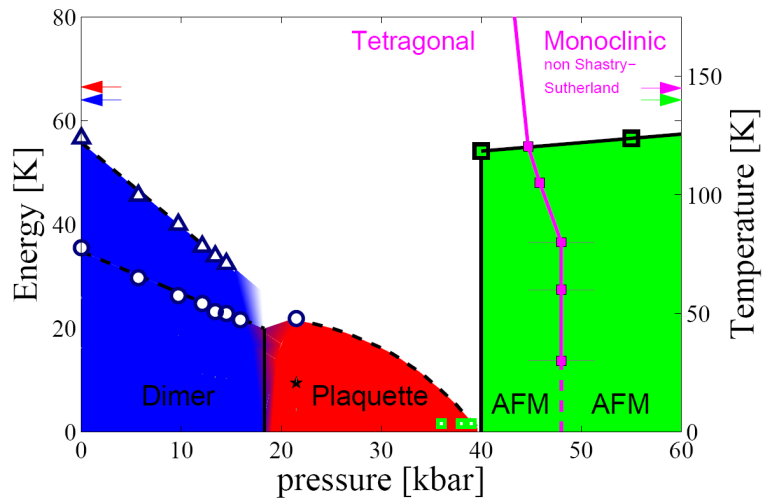


Figure 5.18: Experimental  $p$ - $T$  phase diagram of  $\text{SrCu}_2(\text{BO}_3)_2$ .  $\circ$ ,  $\Delta$ ,  $\star$  are  $\Delta_{Q=(2,0,L)}$ ,  $BT_{Q=(2,0,L)}$  and  $LE_{Q=(1,0,1)}$  respectively. The dimer phase is indicated in blue, the plaquette phase in red with indicative plaquette gap  $\Delta$  energy. The transition between these two phases happens in the shadowed region around 18 kbar. AFM order in green. Large full (small empty) squares indicate where  $Q=(1,0,0)$  peaks are (are not) observed. They are also observed continuously on the full quasi-vertical line at 40 kbar.

We finally present the  $p$ - $T$  phase diagram summarizing our results in Fig.5.18. Dotted lines indicate not sharp transitions, but the gap energy in the dimer and plaquette phases. For the latter, the line is only indicative and follows the theoretical plaquette gap calculation of Ref. [12]. The full vertical line at 18.3 kbar is the first order transition between the two disordered phases assuming  $\alpha_c=0.67$ . The quasi-vertical line at 40 kbar indicates the magnetic ordering transition. The  $(1,0,0)$  peaks are continuously seen along this line.

## 5.6. CONCLUSION ON THE PRESSURE INDUCED QUANTUM PHASES IN $\text{SrCu}_2(\text{BO}_3)_2$ 79

The magenta full line is the structural transition from the tetragonal to the monoclinic phase.





# Chapter 6

## Crystallographic study of $\text{SrCu}_2(\text{BO}_3)_2$

This chapter presents the structural study of  $\text{SrCu}_2(\text{BO}_3)_2$  as function of pressure and temperature. The crystal structure is resolved by neutron powder diffraction at 1.6 K, at ambient pressure, and at 37 and 66 kbar, ambient temperature. At 66 kbar  $\text{SrCu}_2(\text{BO}_3)_2$  is found to crystallize in the C2 monoclinic space group, where it cannot be topologically mapped to the Shastry-Sutherland model any longer. The monoclinic distortion is extracted as function of pressure and temperature by single crystal and powder X-ray diffraction. The neutron powder diffraction experiments were performed on the HRPT diffractometer at SINQ (Villigen) and X-ray diffraction at the synchrotron beam line ID9b of ESRF (Grenoble).

### 6.1 Temperature dependance of the crystal lattice

The ambient condition crystal structure of  $\text{SrCu}_2(\text{BO}_3)_2$  has been solved in the early 90's [24] before the compound was discovered to be a realization of the Shastry-Sutherland model [23].  $\text{SrCu}_2(\text{BO}_3)_2$  crystallizes in the tetragonal  $\bar{I}4_2m$  space group and it was later found that above 395 K a structural transition to the higher symmetry  $I4/mcm$  group occurs [25]. The low temperature structure however has remained unsolved until very recently and it was unclear whether or not another structural transition takes place upon

cooling. In 2009 Vecchini et al. [26] published the 2 K structure of  $\text{SrCu}_2(\text{BO}_3)_2$  and observed important changes upon entering the sin gap regime ( $T \simeq 35$  K). The  $I\bar{4}2m$  symmetry however is not modified. The results we present here are consistent with their study and show effects of spin-lattice coupling in  $\text{SrCu}_2(\text{BO}_3)_2$  at low temperatures.

The powder pattern were taken on HRPT operated at  $\lambda=1.89$  Å with oscillation of the He cryostat to reduce the effects of texture. The  $\text{SrCu}_2(\text{BO}_3)_2$  powder contains some impurity phases identified as CuO and  $\text{Sr}(\text{B}_2\text{O}_4)$ . Figure 6.1 presents a typical diffraction pattern corresponding to an exposition time of about half an our and refined using Rietveld method with Fullprof [98].

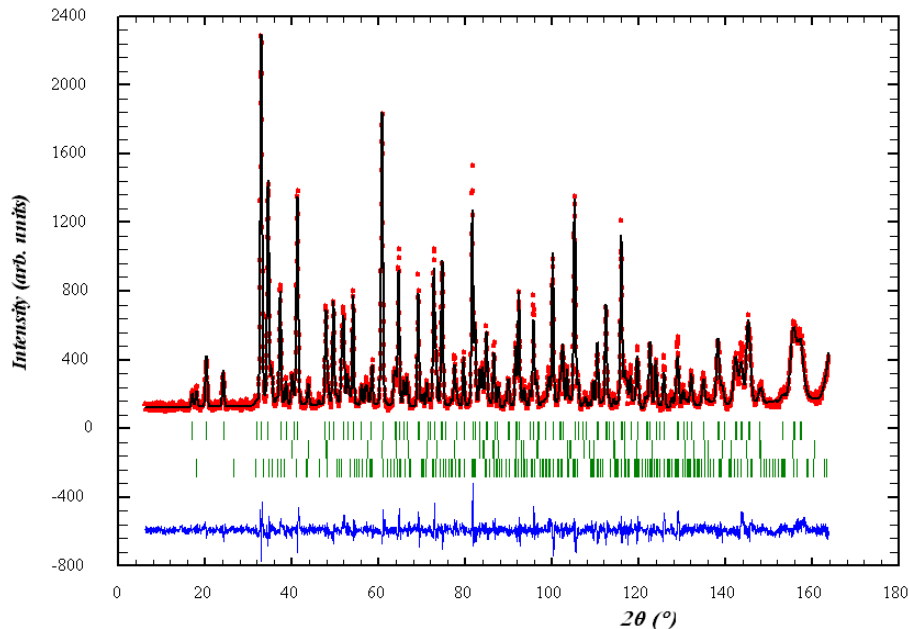


Figure 6.1: Diffraction pattern of  $\text{SrCu}_2(\text{BO}_3)_2$  at 78 K. The red points are experimental data and the black line the refinement fit. Green markers are the Bragg peak position of the main and the two impurity phases. The blue line on the bottom is the difference between the fit and the experimental data. (Bragg R-factor(%): 4.47).

The temperature dependent refinement allows to extract the lattice constants of  $\text{SrCu}_2(\text{BO}_3)_2$  with good accuracy. It can be seen in Fig.6.2 that the unit cell volume initially reduces upon cooling. Quite unusual however is the sudden increase of volume below  $\simeq 35$  K. This is manifested by a negative thermal expansion for the a and b axis (magnetic plane) while the c axis eventually contracts at a slightly lower temperature.

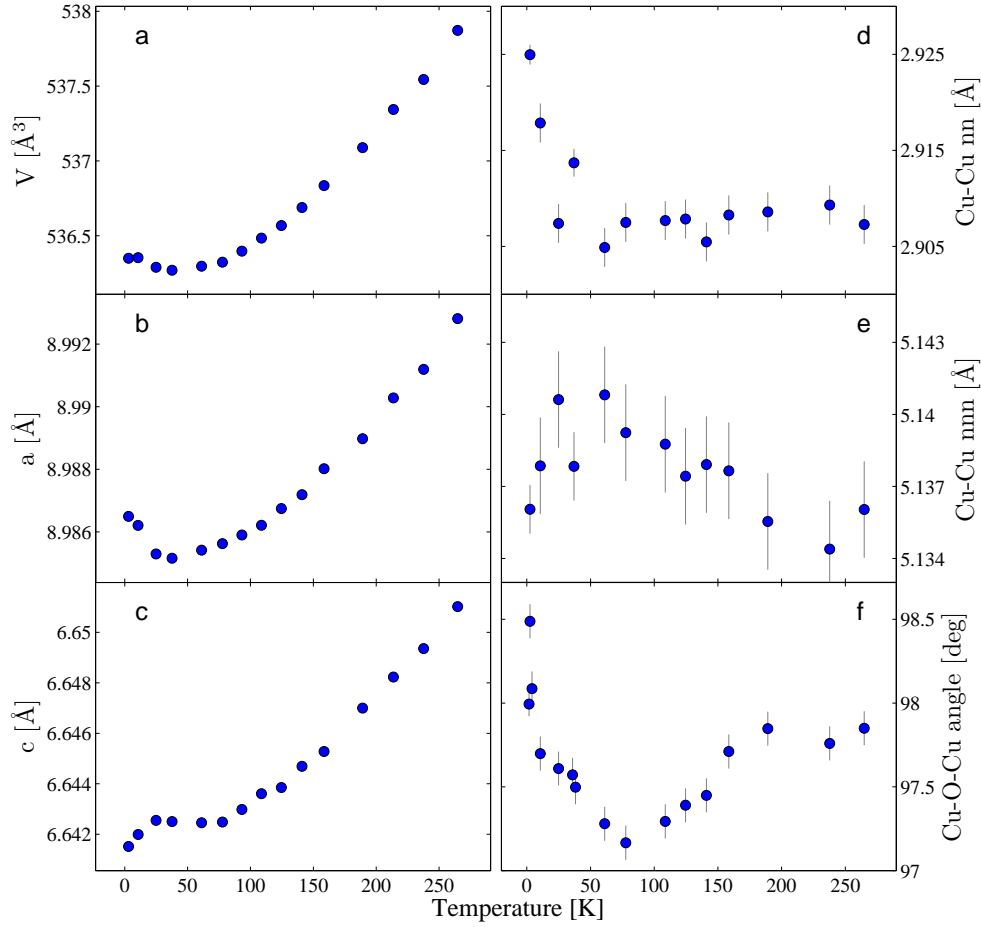


Figure 6.2: Temperature dependence of the crystal structure of  $\text{SrCu}_2(\text{BO}_3)_2$ . (a) Unit cell volume. (b) a-axis (the b-axis is identical by tetragonal symmetry). (c) c-axis. (d) Cu–Cu nearest neighbor distance (intra-dimer). (e) Cu–Cu next nearest neighbor distance (inter-dimer). (f) Cu–O–Cu angle.

The length of the magnetic Cu–Cu dimer increases in the spin gap regime together with the Cu–O–Cu angle. This suggests by Goodenough-Kanamori rules an increase of the coupling integral  $J$ . The next nearest neighbor distance on the other hand slightly reduces. Because of the shrinking of the c-axis the interlayer exchange  $J''$  is likely to be enhanced.

Figure 6.3 presents the structural refinement at  $T=1.6$  K. The position of the atoms and the statistical deviations are given in Table 6.1. Although many structural effects related to the spin-lattice coupling take place at low temperature, the powder spectrum can still be fitted to the  $I\bar{4}2m$  space group. The results we obtain are consistent with those of Ref.[26].

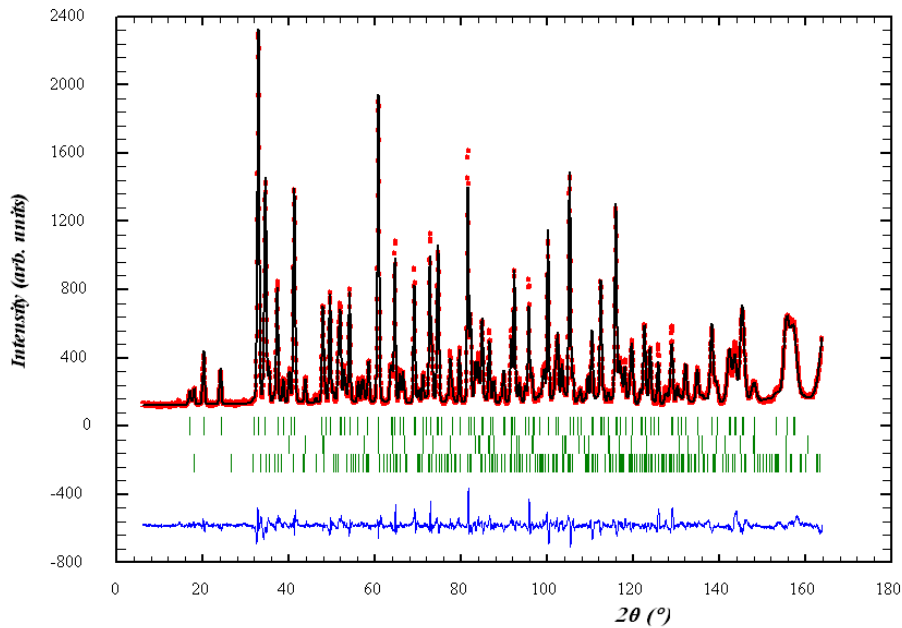


Figure 6.3: Diffraction pattern of  $\text{SrCu}_2(\text{BO}_3)_2$  at 1.6 K. The red points are experimental data and the black line the refinement fit. The blue line on the bottom is the difference between the fit and the experimental data. (Bragg R-factor(%): 3.42).

atom	Wyckoff pos.	x/a	y/b	z/c
Sr	4c	0	0.5	0
Cu	8i	0.11493(14)	0.11493(14)	0.29118(38)
B	8i	0.29524(19)	0.29524(19)	0.23940(38)
O <sub>1</sub>	8i	0.39994(21)	0.39994(21)	0.19982(54)
O <sub>2</sub>	16j	0.32900(16)	0.14657(23)	0.25680(65)

Table 6.1: Atomic position in  $\text{SrCu}_2(\text{BO}_3)_2$  at  $T=1.6$  K. The numbers in parenthesis give the statistical error.  $a=b=8.98734(5)$  Å,  $c=6.64155(6)$  Å. (The room temperature structure is given in Ref.[24])

## 6.2 High pressure crystal structure

The results obtained in Chap. 5 show that pressure affects the magnetic properties of  $\text{SrCu}_2(\text{BO}_3)_2$  by tuning its magnetic exchange parameters, making it enter a plaquette phase between  $\sim 18$  and 40 bar and order antiferromagnetically above that pressure. We shall now see how these magnetic properties relate to the high pressure crystal structure. High pressure neutron powder diffraction is challenging given the small sample sizes and the large sample environment. The structures cannot be resolved as accurately as at ambient conditions. This is particularly true for low symmetry phases such as monoclinic or even tetragonal where the total intensity is scattered among many small Bragg peaks. In the case of  $\text{SrCu}_2(\text{BO}_3)_2$ , no high pressure structure has been published so far. Loa

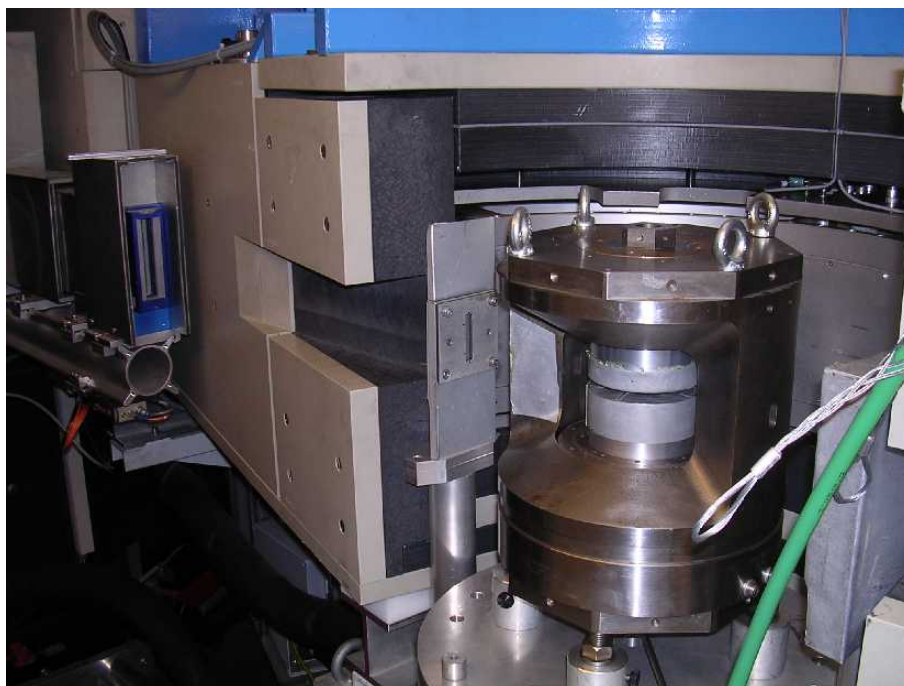


Figure 6.4: Paris-Edinburgh press on the HRPT diffractometer at SINQ PSI (Villigen).

et al. [28] observed by X-ray diffraction and Raman spectroscopy a monoclinic distortion at 47 kbar and another structural transition at 150 kbar, the two new phases however were not resolved. Thanks to the recent developments in high pressure neutron scattering at SINQ, we could obtain refinable powder patterns. The measurements were performed on the HRPT diffractometer ( $\lambda=1.89 \text{ \AA}$ ) with a Paris-Edinburgh press, using deuterated methanol-ethanol 4:1 as pressure medium, boron nitride anvils, and titanium zirconium

gaskets. The anvils provide an intrinsic collimation of the neutron beam through the large absorption of Boron. Titanium and zirconium with opposed scattering lengths produce no additional Bragg peaks in the diffraction pattern. Furthermore oscillating radial collimators (mylar-Gd-O) were placed on the spectrometer to eliminate the remaining Bragg reflections from the sample environment. Pressure is determined by the lattice constant of the sample following the equation of state for  $\text{SrCu}_2(\text{BO}_3)_2$  published in Ref. [28]. Figure 6.4 shows a picture of the setup we used, and Fig.6.5 the refined powder pattern measured at 37 kbar. The atomic positions are given in Table 6.2. The impurity phases coming from the sample environment contribute less than 1% after background subtraction.

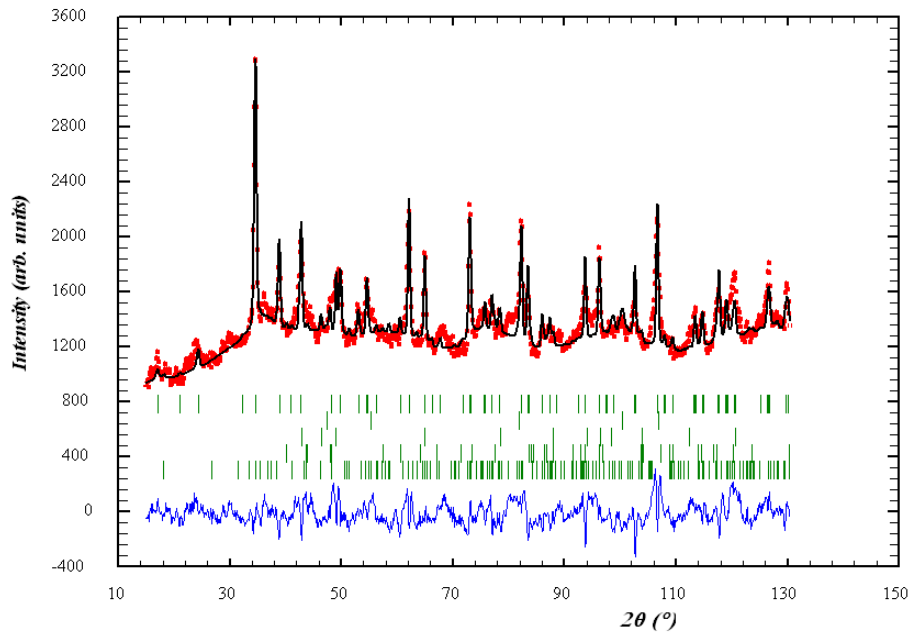


Figure 6.5: Diffraction pattern of  $\text{SrCu}_2(\text{BO}_3)_2$  at 37 kbar. The red points are experimental data and the black line the refinement fit. The blue line on the bottom is the difference between the fit and the experimental data. (Bragg R-factor(%): 25.3).

The refinement indicates that  $\text{SrCu}_2(\text{BO}_3)_2$  can still be assigned to the tetragonal  $\bar{I}42m$  space group at 37 kbar, suggesting no structural phase transition takes place at ambient temperature before the monoclinic distortion. The unit cell mostly contracts along the  $c$ -axis due to the layered structure of the compound. The dimer length is shortened from ambient 2.91 to 2.88 Å. The Cu–O–Cu angle reduces accordingly from 98 to  $\sim 95$  degrees

atom	Wyckoff pos.	x/a	y/b	z/c
Sr	4c	0	0.5	0
Cu	8i	0.1138(13)	0.1138(13)	0.2941(29)
B	8i	0.3013(12)	0.3013(12)	0.2671(45)
O <sub>1</sub>	8i	0.3985(17)	0.3985(17)	0.2608(62)
O <sub>2</sub>	16j	0.3206(14)	0.1474(14)	0.2497(43)

Table 6.2: Atomic position in SrCu<sub>2</sub>(BO<sub>3</sub>)<sub>2</sub> at p=37 kbar, T=300K. The numbers in parenthesis give the statistical error. a=b=8.94988(31) Å, c=6.33943(46) Å.

which is consistent with the decrease of  $J$  obtained by fits to the susceptibility. The experimental evidences of Chap. 5 suggest that  $J$  is still antiferromagnetic. Similar to what happens as function of temperature, the nnn distance (5.126 Å) is hardly modified. This can be related to the presence of a rigid BO<sub>3</sub> group on the nnn path. The shortest interlayer Cu–Cu distance at 37 kbar is 3.31 Å to be compared with 3.59 Å at ambient conditions, which may indicate that pressure enhances 3D effects in the compound. However due to the absence of a strong magnetic coupling path, even short Cu–Cu interlayer distances should not result in a large  $J''$ .

We now turn to the monoclinic phase that appears above 47 kbar [28]. Figure 6.6 shows the refined diffraction pattern at 66 kbar. The pattern cannot be assigned to a tetragonal space group any longer, and a clear splitting of Bragg peaks is observed. We find a solution in the C2 subgroup of  $I\bar{4}2m$ . Sr, Cu, B, and O<sub>1</sub> split into two non equivalent positions in C2 and O<sub>2</sub> into four. The two Sr atoms are on special positions with multiplicity 2 while all other atoms are on a general position. The mirror planes passing through the dimers in  $I\bar{4}2m$  are lost in C2. As a result there is no crystallographic symmetry which maintains the dimers orthogonal, nor the four next nearest neighbor coupling  $J'$  equivalent. The nearest neighbor intra-dimer coupling  $J$  on the other hand remains unique in C2. The atomic positions of our refinement are given in Table 6.3. A soft constrain of  $1.37 \pm 0.3$  Å on the B–O distance has been implemented in the fit in order to maintain reasonable BO<sub>3</sub> units.

We choose the conventional setting with unique b-axis for the C2 space group. The

transformation matrix to the new basis is given by

$$P = \begin{pmatrix} -1 & 0 & 1 \\ 0 & 1 & 0 \\ -1 & 0 & 0 \end{pmatrix} \quad (6.1)$$

and the new Miller indices in C2 ( $H_C, K_C, L_C$ ) are related to the old  $\bar{I}42m$  indices ( $H, K, L$ ) by ( $H_C = -H - L, K_C = K, L_C = H$ ). The unit cell at 66 kbar,  $a=10.32$ ,  $b=8.92$ ,  $c=8.90$  Å,  $\beta=143.5^\circ$  corresponds in the old setting to  $a=8.90$ ,  $b=8.92$ ,  $c=6.17$  Å and a monoclinic angle  $\beta=95.6^\circ$ .

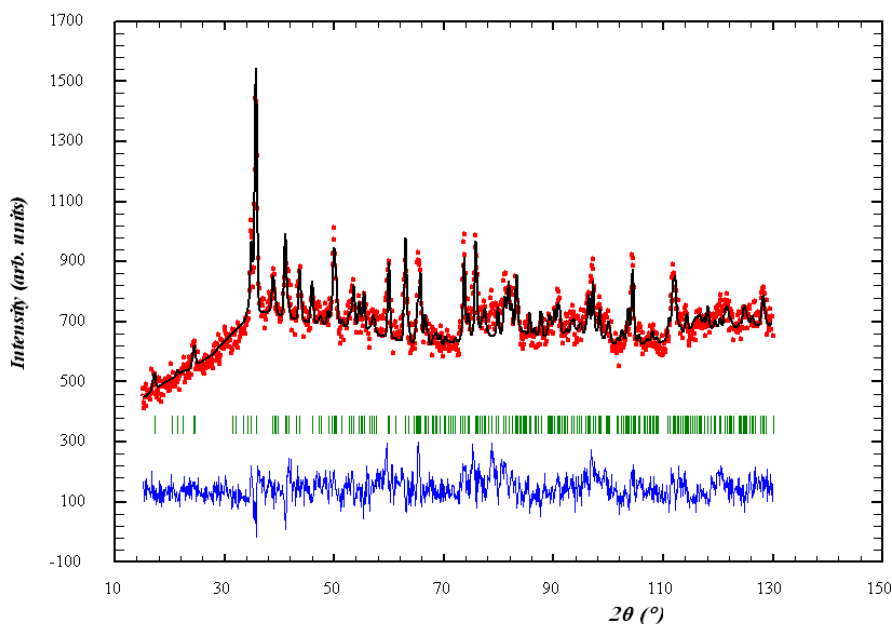


Figure 6.6: Diffraction pattern of  $\text{SrCu}_2(\text{BO}_3)_2$  at 66 kbar. The red points are experimental data and the black line the refinement fit. The blue line on the bottom is the difference between the fit and the experimental data. (Bragg R-factor(%): 29.7).

Figure 6.7 provides a view of the magnetic plane and of the layered structure of  $\text{SrCu}_2(\text{BO}_3)_2$  at 37 kbar at 66 kbar. The first observation regarding the structure beyond the monoclinic distortion is that the dimers although not constrained by symmetry, remain close to orthogonal. The dimer length is reduced to 2.76 Å. The  $\text{Cu}_2\text{O}_2$  dimer unit is distorted and there are two different Cu–O–Cu angles:  $93^\circ$  and  $83^\circ$ . The precise value of these angles depends on the B–O distances which had to be constrained in the fit. The before unique next nearest neighbor Cu distances splits into two shorter (5.02 and 5.09 Å) and two



atom	Wyckoff pos.	x/a	y/b	z/c
Sr <sub>1</sub>	2a	0	0.4692(135)	0
Sr <sub>2</sub>	2b	0.5	0.4866(135)	0.5
Cu <sub>1</sub>	4c	0.7119(63)	0.6209(131)	0.1117(80)
Cu <sub>2</sub>	4c	0.2771(54)	0.4023(129)	0.6589(81)
B <sub>1</sub>	4c	0.6916(59)	0.7706(128)	0.9310(69)
B <sub>2</sub>	4c	0.2714(61)	0.1986(126)	0.4594(78)
O <sub>1</sub>	4c	0.7382(104)	0.9124(136)	0.8348(125)
O <sub>2</sub>	4c	0.2522(85)	0.1422(137)	0.3726(103)
O <sub>3</sub>	4c	0.7262(73)	0.6430(132)	0.9110(97)
O <sub>4</sub>	4c	0.2678(77)	0.1929(137)	0.6321(94)
O <sub>5</sub>	4c	0.8143(76)	0.3933(127)	0.6245(101)
O <sub>6</sub>	4c	0.2252(84)	0.8508(136)	0.8603(108)

Table 6.3: Atomic position in SrCu<sub>2</sub>(BO<sub>3</sub>)<sub>2</sub> at p=66 kbar, T=300 K. The numbers in parenthesis give the statistical error. a=10.31871(77) Å, b=8.92385(45) Å, c=8.89855(62) Å,  $\beta=143.4606(33)^\circ$ .

longer (5.18 and 5.23 Å) distances. The coupling paths however are all different so that we consider this should lead to a spitting of  $J'$  into four different terms and not only two. The shortest Cu–Cu interlayer distance is now 3.02 Å.

Finally we present our results on the temperature dependence of the monoclinic distortion. It was extracted from single crystal and powder X-ray diffraction measurements using a diamond anvil cell at the high pressure beamline ID9b of the ESRF synchrotron in Grenoble. The setup is the one given in Table 5.1. We follow the splitting of Bragg peaks in the monoclinic phase as function of pressure in order to extract the critical pressure for the transition. Typical example of peak splitting are shown in the inset of Fig.6.8. The upper one corresponds to the splitting of  $Q=(2,1,1)$  tetragonal into four non equivalent peaks  $Q=(-3,1,2)$ ,  $(-1,1,2)$ ,  $(-2,2,1)$ ,  $(0,2,1)$  in the monoclinic phase for a powder sample and the lower one to the splitting of  $Q=(5,1,0)$  into two non equivalent reflections  $(-5,1,5)$  and  $(-1,5,1)$  in a single crystal sample. We obtain that the critical

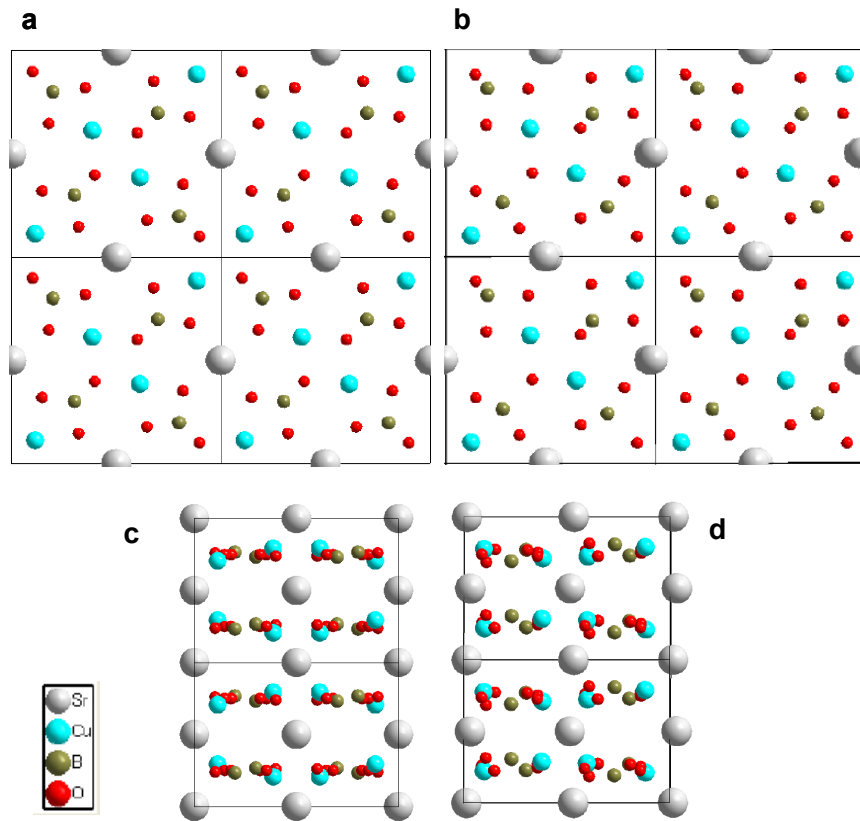


Figure 6.7: Views of the crystal structure at high pressure. (a)  $p=37$  kbar, magnetic plane. (b)  $p=66$  kbar, magnetic plane after the monoclinic distortion. (c)  $p=37$  kbar, interlayer view along the  $b$ -axis showing a cut through 4 magnetic planes in two unit cells. (d) Similar view at  $p=66$  kbar.

pressure remains confined between 40 and 50 kbar from ambient to base temperature. At low temperature the error bars are larger due to the smaller number of pressures measured<sup>1</sup>. The lowest critical pressure (43 kbar) is found at 200 K. It thus seem that the magnetic ordering discussed in Chap. 5 takes place relatively close to but still before the structural distortion.

<sup>1</sup>This is due to the inherent difficulty in increasing pressure at low temperatures when pressure transmitting medium and capillaries freeze.

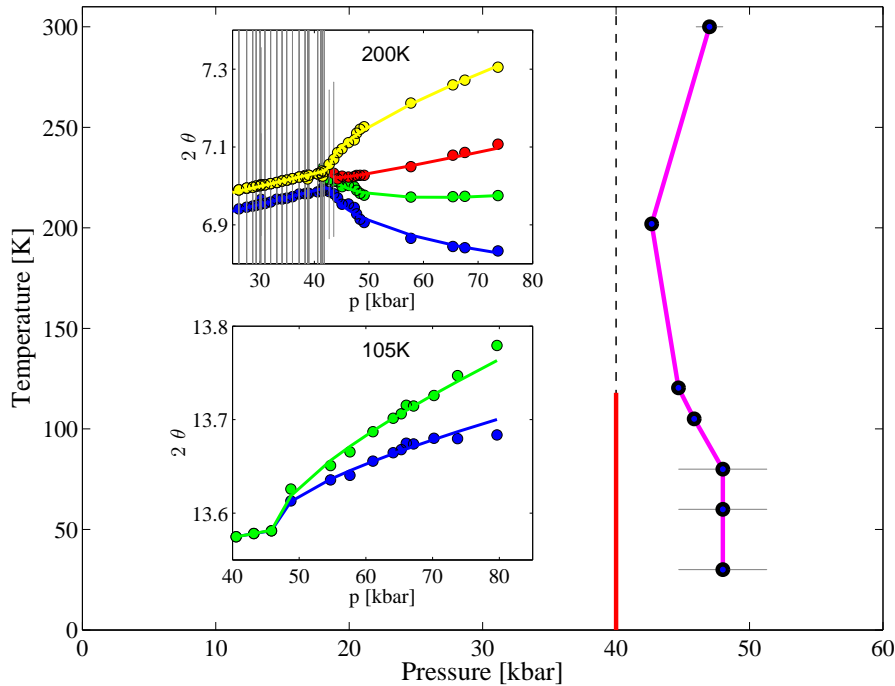


Figure 6.8: Monoclinic distortion as function of pressure and temperature. The symbols with horizontal error bars give the critical (p,T) determined by X-ray diffraction and they are connected by the magenta line. The inset shows the fits to the splitting of Bragg peaks from the original tetragonal into non equivalent monoclinic (see text). The red line at 40 kbar represents the onset of magnetic ordering.

### 6.3 Conclusion on the crystallographic study

In summary we have obtained important structural information on  $\text{SrCu}_2(\text{BO}_3)_2$  that will provide a better understanding of its magnetic properties. They could, for instance, be used for ab-initio calculations in order to quantify the magnetic couplings. The low temperature structure and the temperature dependence of the lattice have been obtained by neutron diffraction. They are in good agreement with the recent publication by Vecchini et al. [26] and clearly show spin-lattice coupling effects upon entering the spin gap regime. We have also studied the high pressure structure and were able to solve it in both the tetragonal and the monoclinic phases. The Cu–O–Cu angles reduce as function of pressure which seems consistent with the decrease of magnetic coupling obtained from fits to the susceptibility. The resolution of a complex monoclinic phase is, in itself, remarkable given the low symmetry implying a large number of non equivalent atoms in the

unit cell. This has been made possible by recent improvements in high pressure neutron diffraction. The monoclinic structure shows that  $\text{SrCu}_2(\text{BO}_3)_2$  cannot be described by the Shastry-Sutherland model at high enough pressure. The dimers although still close to being orthogonal, are connected to each other by four different next nearest neighbor couplings implying a relief of the perfect frustration existing at lower pressure. As a consequence one could expect a rapid magnetic ordering once the frustration starts to be lifted. The extraction of the critical monoclinic pressure as function of temperature, indicates that magnetic ordering at 40 kbar actually seems to take place just before the structural distortion. We thus explain it, in Chap. 5, by the Neel order expected from the original Shastry-Sutherland model. The magnetic structure in the monoclinic phase on the other hand may well be different.

# Chapter 7

## Conclusion and Outlook

This thesis has presented our results on the Shastry-Sutherland compound  $\text{SrCu}_2(\text{BO}_3)_2$  studied at different temperatures and pressures.

It was shown that it is possible to tune  $\text{SrCu}_2(\text{BO}_3)_2$  by application of hydrostatic pressure out of the exact dimer phase to a plaquette singlet state and eventually to an AFM ordered phase. The first transition occurs around 18 kbar and the second at 40 kbar. This brings a strong experimental evidence to the controversial theoretical issue of the intermediary phase in the Shastry-Sutherland model. This evidence is in favor of the existence of an intermediary plaquette phase on the plaquettes containing a diagonal bond .

The structural part of the work has confirmed the recently observed spin-lattice coupling in  $\text{SrCu}_2(\text{BO}_3)_2$  upon entering the spin gap regime. It has also provided the first structural information on this compound at high pressures. The tetragonal-monoclinic distortion has been traced as function of pressure and temperature.  $\text{SrCu}_2(\text{BO}_3)_2$  is found to crystallize in the C2 space group and the atomic positions have been determined. The dimers remain quasi-orthogonal but the next nearest neighbor couplings split into four non-equivalent  $J'$ .

On the technical side, it was also shown that these new high pressure phases can be studied by neutron scattering even though this requires a very challenging sample environment with reduced sample sizes: the plaquette phase was observed by INS with a 0.2 g single crystal at 21.5 kbar in a large pressure cell cooled down to  $T=0.5$  K, and the low symmetry

monoclinic phase with 44 atoms in the unit cell occupying 12 inequivalent positions could be refined at 66 kbar.

The INS study of the gap excitation as function of temperature has revealed that the excitation is damped, and can be modeled by a sharp and a broad component which exchange intensity as temperature varies between 0 and 10 K. This damping could be explained by a simple phenomenological model indicating that it is the simultaneous presence of two triplets in the same ‘region’ that causes the decay. The size of this region could be calculated and is about 21 unit cells.

Some open questions remain, as why is the Neel temperature of the ordered phase so high. Is the magnetic order in the monoclinic phase different than the one in the tetragonal phase. A theoretical study of a modified – not perfectly frustrated – Shastry-Sutherland Hamiltonian containing four different  $J'$  could bring an answer. Can a calculation reproduce our experimental observations in the plaquette phase, i.e. a plaquette ground state on the plaquettes containing a diagonal bond with the triplet excitation being lower in energy than the quadruplet at the actual coupling values of  $\text{SrCu}_2(\text{BO}_3)_2$ . We hope that this experimental work will trigger some interest from theorists to address such issues.

Finally we mention here the yet unpublished work by J. A. Larrea at the Laboratory for Quantum Magnetism at EPFL. High pressure specific heat measurements on  $\text{SrCu}_2(\text{BO}_3)_2$  have confirmed the neutron results and support the phase transition around 18 kbar as well as the existence of a new type of excitation. It further shows some intriguing magnetic field dependence in the new phase. This is certainly another issue to further investigate in the future.

# Appendix A

## The isolated dimer model

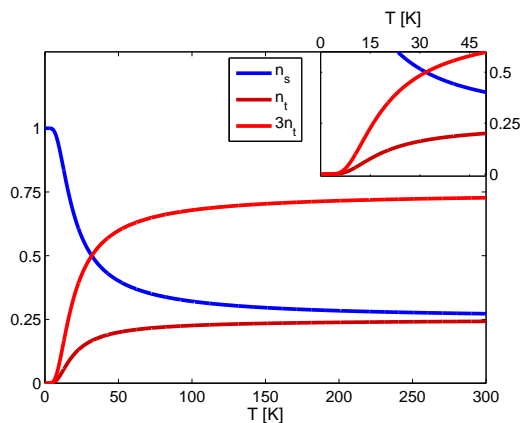


Figure A.1: Relative number of singlets  $n_s = 1/(1 + 3e^{-\beta\Delta})$  and triplets  $n_t = 1/(3 + e^{\beta\Delta})$  as function of temperature for isolated dimers with a 35 K gap. The inset is a zoom into the 0–50 K range.

A spin pair – a dimer – coupled antiferromagnetically gives the simplest example of a non-classical, non-magnetic singlet ground state. This simple system is important as dimers are often the basic units in frustrated magnets and the tendency to form dimer singlets appears to be quite a generic feature. For instance, the degenerate ground states of a spin  $s = 1/2$  triangle<sup>1</sup> can be viewed as a singlet plus a left alone spin, and those of a tetrahedra as a product of singlets on opposed bounds. When taking  $J'=0$  in the Shastry-Sutherland model one obtains isolated dimers, and even for  $\alpha \leq \sim 0.7$  the ground state of the Shastry-

---

<sup>1</sup>It is however now believed that the extended triangular lattice shows three-sublattice long range order and not an RVB state on the all dimer configurations as proposed earlier [99, 100].

Sutherland model is a product of singlets, and the triplet excitations remain localized to  $6^{\text{th}}$  order. Therefore, it is instructive to examine the properties of isolated dimers as a ‘zero<sup>th</sup> order’ approximation to the more complex Shastry-Sutherland model.

We will derive the specific heat, the magnetic susceptibility, and the neutron scattering structure factor. Most of the differences we shall find between the isolated dimer calculation and the real material, will be a manifestation of the frustration and the extended electron correlations neglected in the simplification.

Two antiferromagnetically coupled  $s = 1/2$  spins form a dimer described by the simple Hamiltonian:

$$H = J\vec{S}_1\vec{S}_2. \quad (\text{A.1})$$

The ground state is unique and separated by a gap  $\Delta = J$  to three excited states. The energies are

$$\begin{aligned} E_0 &= -3/4J \\ E_1 = E_2 = E_3 &= 1/4J, \end{aligned} \quad (\text{A.2})$$

and the eigenstates correspond to an  $s = 0$  ‘singlet’ for the ground state  $|\Psi_0\rangle$  with energy  $E_0$  and three  $s = 1$  ‘triplet’ states  $|\Psi_{1,2,3}\rangle$  with equal energies  $E_1 = E_2 = E_3$ :

$$\begin{aligned} |\Psi_0\rangle &= \frac{1}{\sqrt{2}}[|\uparrow\downarrow\rangle - |\downarrow\uparrow\rangle] \\ |\Psi_1\rangle &= |\downarrow\downarrow\rangle \\ |\Psi_2\rangle &= \frac{1}{\sqrt{2}}[|\uparrow\downarrow\rangle + |\downarrow\uparrow\rangle] \\ |\Psi_3\rangle &= |\uparrow\uparrow\rangle \end{aligned} \quad (\text{A.3})$$

In presence of a magnetic field  $\vec{B}$  the energy of the  $m = \pm 1$  triplet states  $|\Psi_{3,1}\rangle$  will shift by  $\mp g\mu_b B$ . The partition function is then given by

$$Z = e^{-\frac{1}{4}\beta\Delta}(e^{\beta\Delta} + 1 + 2\cosh(\beta g\mu_b B)) \quad (\text{A.4})$$



where  $\beta = 1/k_bT$  and the singlet and triplet populations in zero field by

$$n_s(T) = 1/(1 + 3e^{-\beta\Delta}) \quad (\text{A.5})$$

$$n_t(T) = 1/(3 + e^{\beta\Delta}). \quad (\text{A.6})$$

Figure A.1, shows the decay of the singlet population in the isolated dimer model as function of temperature: the gap value roughly corresponds<sup>2</sup> to 50% of singlets, while at high temperatures the singlet proportion tends to 25%. The situation will turn out to be very different for  $\text{SrCu}_2(\text{BO}_3)_2$  with inelastic neutron scattering intensity – in principle proportional to the number of singlets – decreasing in a more subtle manner as discussed in Chap. 4.

From (A.4) one can derive the thermodynamic quantities as the free energy  $F = -\frac{1}{\beta} \ln(Z)$ , the magnetization  $M = -n \frac{\partial F}{\partial B}$  and the susceptibility  $\chi = \frac{\partial M}{\partial H}$  for a volume dimer density  $n$ . In the limit where  $\chi \ll 1$  the susceptibility is given by a simple expression and is proportional to number of triplets divided by the temperature:

$$\chi = n\mu_0\beta \frac{2g^2\mu_b^2}{3 + e^{\beta\Delta}} \quad \propto \frac{1}{T}n_t \quad (\text{A.7})$$

Similarly, the specific heat  $c = T \frac{\partial S}{\partial T}$  is obtained from the entropy  $S = -\frac{\partial F}{\partial T}$ :

$$c = \frac{3k_b(\beta\Delta)^2 e^{-\beta\Delta}}{(1 + 3e^{-\beta\Delta})^2} \quad (\text{A.8})$$

At high temperatures, the susceptibility follows a  $1/T$  paramagnetic-like curve (Fig. A.2). For temperatures well below the gap, thermal excitation to the magnetic triplet states becomes unlikely and the susceptibility rapidly goes to zero as only non-magnetic singlets are left. Between these two extremes, susceptibility has a peak with a maximum around  $\sim 0.62\Delta$ . Specific heat has a sharper peak at  $\sim 0.35\Delta$ . This is a typical behavior for spin gap systems and it is also encountered in  $\text{SrCu}_2(\text{BO}_3)_2$ . The value of the isolated dimer susceptibility can be compared with the experimental results for  $\text{SrCu}_2(\text{BO}_3)_2$ , introducing a volume density for the dimers  $n \simeq 4.39 \cdot 10^{20} \text{cm}^{-3}$  and a number of Cu moles

<sup>2</sup>The singlet population is 50% when  $k_bT = \Delta/\ln(3) \simeq 0.91\Delta$ .

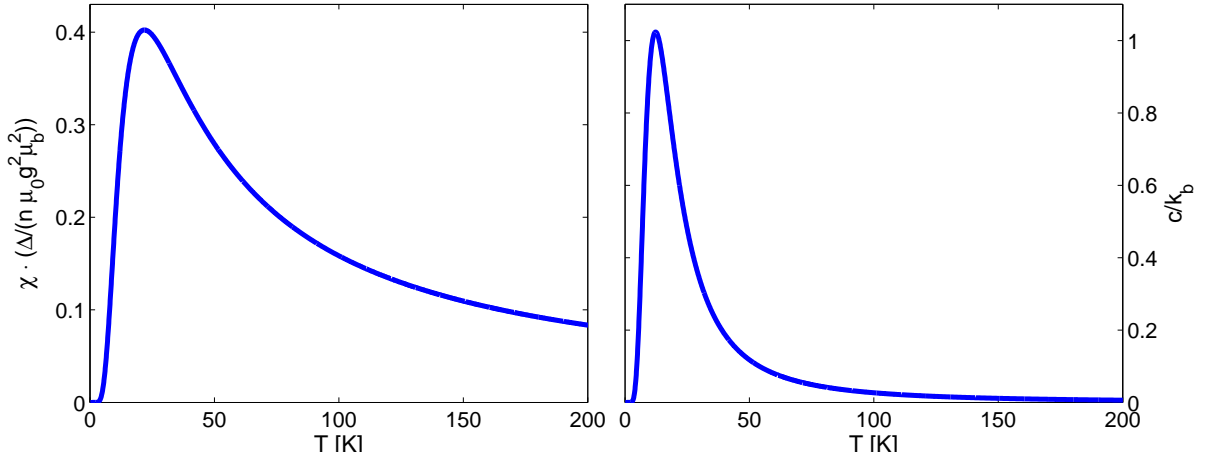


Figure A.2: Isolated dimer model with  $\Delta=35 \text{ K} \cdot k_b$  (a) Magnetic susceptibility, (b) Specific heat.

per  $\text{cm}^3 \simeq 0.0015$ . This is shown in Fig.A.3 where it can be seen that the peak maximum is strongly suppressed in the real material. The maximum is also located at a lower temperature (17 K) than for the isolated dimer (22 K). The differences can be attributed to the extended and frustrated interaction in  $\text{SrCu}_2(\text{BO}_3)_2$ <sup>3</sup>.

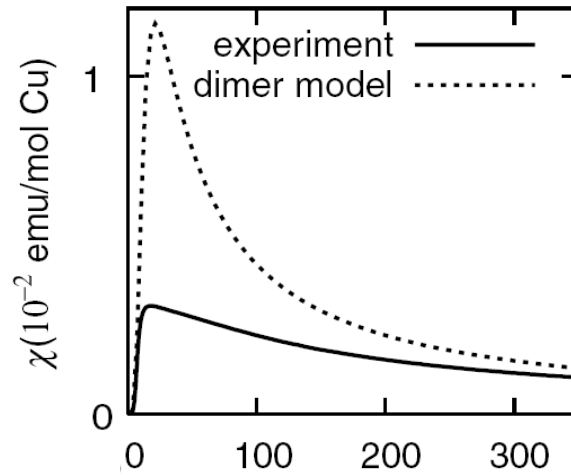


Figure A.3: Comparison between the susceptibility of  $\text{SrCu}_2(\text{BO}_3)_2$  (full line) and an isolated dimer susceptibility with  $\Delta=35 \text{ K}$ . Reproduced from [7].

The structure factor  $S(\vec{Q})$  is another important quantity to compute since it gives the momentum dependence observed in neutron scattering experiments. For a single dimer it

<sup>3</sup>Note that they are already responsible for the material having a gap  $\Delta=35 \text{ K}$ , while  $J$  is  $\sim 85 \text{ K}$ .

is given by<sup>4</sup> [101]

$$S(\vec{Q}) = \frac{1}{2}(1 - \cos(\vec{Q} \cdot \vec{d})) \quad (\text{A.9})$$

or averaged over random orientations:

$$\bar{S}(Q) = \frac{1}{2}(1 - \sin(Qd)/Qd) \quad (\text{A.10})$$

with  $\vec{d}$  the spatial vector connecting the two spins of the dimer. The first relation is relevant for a single crystal, while the second relates to a powder sample. To be more specific in the single crystal Q dependence, we use the geometry of  $\text{SrCu}_2(\text{BO}_3)_2$  with two orthogonal dimers oriented diagonally in a square unit cell with lattice constant  $8.99 \text{ \AA}$  and a distance of  $2.9 \text{ \AA}$  between the spins in each dimer (See Chap. 2).

$$S(\vec{Q}) = \sin^2(\zeta(Q_h - Q_k)) + \sin^2(\zeta(Q_h + Q_k)) \quad (\text{A.11})$$

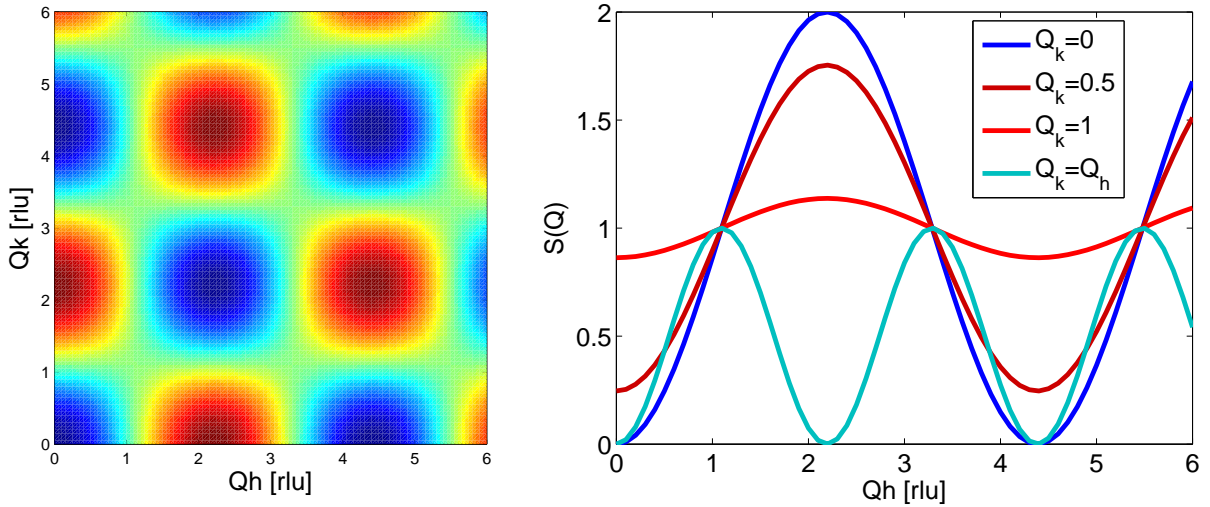


Figure A.4: Structure factor for two isolated dimers with  $\text{SrCu}_2(\text{BO}_3)_2$  geometry, Eq.A.11. Intensity scale for the color map (left): low intensity in dark blue to high intensity in dark red.

with the constant  $\zeta=0.7166$  and  $Q_{h,k}$  in reciprocal lattice units. The Q dependence of the susceptibility can also be computed [86] and is plotted in Fig.A.5.

<sup>4</sup>The structure factor is given by specializing the dynamical structure factor (Eq.3.20) to the singlet-triplet transition.

$$\chi(\vec{q}) \propto \frac{2}{\Delta} A(\vec{q})(1 - e^{-\beta\Delta}) + 2\beta B(\vec{q})e^{-\beta\Delta}, \quad (\text{A.12})$$

$$A(\vec{q}) = \frac{\sin^2(\zeta(q_h - q_k)) + \sin^2(\zeta(q_h + q_k))}{4(1 + 3e^{-\beta\Delta})} \quad (\text{A.13})$$

$$B(\vec{q}) = \frac{\cos^2(\zeta(q_h - q_k)) + \cos^2(\zeta(q_h + q_k))}{4(1 + 3e^{-\beta\Delta})} \quad (\text{A.14})$$

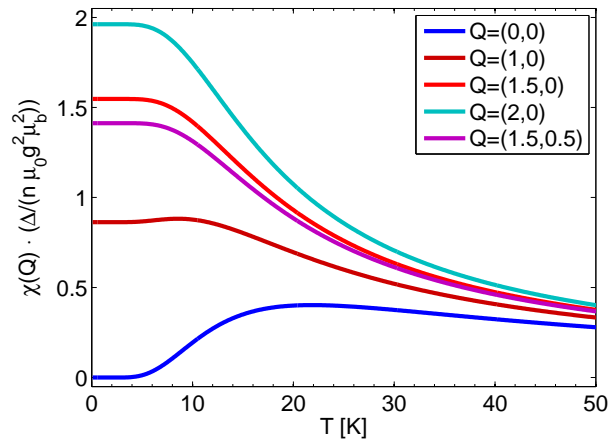


Figure A.5: Q-dependent susceptibility with  $\text{SrCu}_2(\text{BO}_3)_2$  geometry, Eq.A.12.

# Appendix B

## Four spins plaquette

We analyze here the energy spectrum and the neutron scattering structure factor for an isolated four spins plaquettes. The high pressure study of  $\text{SrCu}_2(\text{BO}_3)_2$  has shown (Chap. 5) that the excitation spectrum is strongly modified at 21.5 kbar with a new type of excitation appearing at 1 meV. This excitation has a structure factor peaking around  $Q=(1,0,0)$  and is accompanied by another excitation at 2 meV which displays a structure factor identical to the singlet-triplet gap of the low pressure dimer phase. The plaquettes considered for the calculations are displayed in Fig.B.1. They correspond to position of the  $\text{Cu}^{2+}$  ions  $\text{SrCu}_2(\text{BO}_3)_2$ . We distinguish between ‘void’ plaquettes with no diagonal bond and ‘full’ plaquettes containing a diagonal bond. For each type they are two possible orientations. In the  $\text{SrCu}_2(\text{BO}_3)_2$  geometry the full plaquettes are strongly elongated while the void are almost squares.

The Hamiltonian for the void and full plaquettes (with diagonal bond taken between spins 1 and 3) are given by:

$$H_{\text{void}} = J'(\vec{S}_1\vec{S}_2 + \vec{S}_2\vec{S}_3 + \vec{S}_3\vec{S}_4 + \vec{S}_1\vec{S}_4) \quad (\text{B.1})$$

$$H_{\text{full}} = J'(\vec{S}_1\vec{S}_2 + \vec{S}_2\vec{S}_3 + \vec{S}_3\vec{S}_4 + \vec{S}_1\vec{S}_4) + J(\vec{S}_1\vec{S}_3). \quad (\text{B.2})$$

The eigenstates can be fully characterized (Table B.1) by the value of the total spin  $s^{\text{tot}}$  and the values of the total spin on the two diagonals  $s^{1,3}$  and  $s^{2,4}$  [102]:

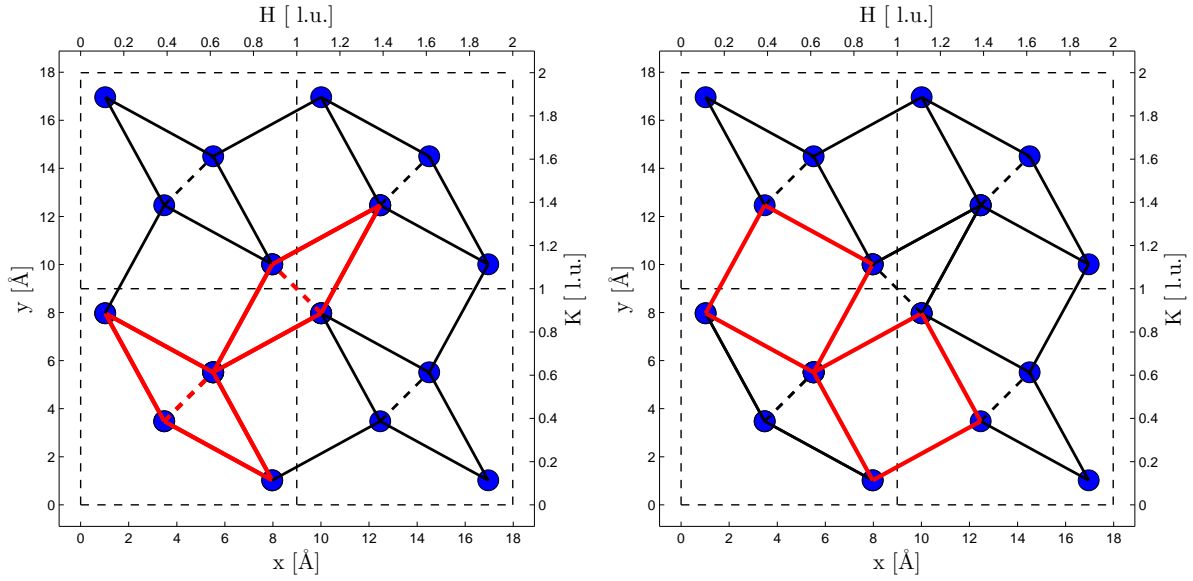


Figure B.1: Geometry of the full (left) and void (right) plaquettes in  $\text{SrCu}_2(\text{BO}_3)_2$ . The positions of the sites refer to ambient crystal structure.

For  $J'/J \geq 1/2$  the ground state is a singlet with energy  $E_0$ . For  $J'/J \geq 1$  the first excited state is a triplet with energy  $E_1$ , while for  $1 \geq J'/J \geq 1/2$ , the first excited state is  $E_{2a,b}$ . The energies  $E_{2a}$  (singlet) and  $E_{2b}$  (triplet) are degenerated and form a quadruplet. The  $E_{2a,b}$  quadruplet corresponds to a singlet on the diagonal plus two free spins. For the void plaquette ( $J=0$ )  $E_{2a,b}$  and  $E_3$  are further degenerate and form a septuplet.

We now compute the neutron scattering structure factor for the transitions between the  $E_0$  ground state and the first two excited states on the void and full plaquette.

The structure factor is given by specializing (3.20) to a specific transition:

$$S^{\alpha,\beta}(\vec{Q}) = \sum_{a,b} e^{i\vec{Q}\cdot(\vec{R}_a - \vec{R}_b)} \sum_{\lambda_f} \langle \lambda_i | S_a^\alpha | \lambda_f \rangle \langle \lambda_f | S_b^\beta | \lambda_i \rangle \quad (\text{B.3})$$

with  $|\lambda_i\rangle$  the unique ground state and  $|\lambda_f\rangle$  the degenerate excited states, and where  $\alpha, \beta = x, y, z$ .

Figure B.3, shows the structure factors ( $S^{x,x} + S^{y,y} + S^{z,z}$ ) for one of the two possible full plaquette orientations. The other plaquette is simply obtained by mirror symmetry along  $Q_k$ . The important result is that the singlet-triplet  $E_0 \rightarrow E_1$  transition peaks just

	Energy	$s^{tot}$	$s^{1,3}$	$s^{2,4}$
$E_0$	$-2J' + J/4$	0	1	1
$E_1$	$-J' + J/4$	1	1	1
$E_{2a}$	$-3J/4$	0	0	0
$E_{2b}$	$-3J/4$	1	0	1
$E_3$	$-J/4$	1	1	0
$E_4$	$J' + J/4$	2	1	1

Table B.1: Energies and eigenstates for the four spins plaquette.

above  $Q_h=1$  and the singlet-quadruplet transition  $E_0 \rightarrow E_2$  has a structure factor strictly identical to the dimer singlet-triplet structure factor.

In Fig.B.4, we compute the sum of the structure factors for the two possible orientations of the full plaquettes. The  $E_0 \rightarrow E_1$  transition has some high intensity regions as around  $Q=(2,2,0)$ . By symmetry, the results are the same as before along the  $Q=(H,0,0)$  line. The  $E_0 \rightarrow E_2$  transition has a structure factor strictly identical to that of the two orthogonal dimers in the  $\text{SrCu}_2(\text{BO}_3)_2$  geometry (shown in Fig.A.4).

Figure B.5 shows  $S(\vec{Q})$  for one of the two possible orientations of the void plaquette. The other orientation is obtained by symmetry along  $Q_h=Q_k$ . The  $E_0 \rightarrow E_1$  transition has a structure factor similar to the one obtained for the full plaquette but the intensity peaks in the magnetic plane have more circular shapes denoting the smaller distortion of the void plaquettes. Along the  $Q=(H,0,0)$  line however, the structure factors for all the four types of plaquettes considered are identical.

The transition to the second excited state is now  $E_0 \rightarrow [E_2E_3]$  since  $E_2$  and  $E_3$  are degenerate.  $S(\vec{Q})$  is in general very different than the singlet-triplet excitation of a dimer. Along the  $Q=(H,0,0)$  line, the void plaquettes display a triple peak structure between  $Q_h=0$  and  $Q_h=4$ , where the dimer has a single peak. The sum over the two void plaquettes orientations is given in Fig.B.6.

The conclusion of this analysis is that the isolated four spins plaquette containing a diagonal bond catches the main features observed experimentally in  $\text{SrCu}_2(\text{BO}_3)_2$  at 21.5 kbar. The ground state is a non magnetic singlet, there is a gap – which is actually expected to

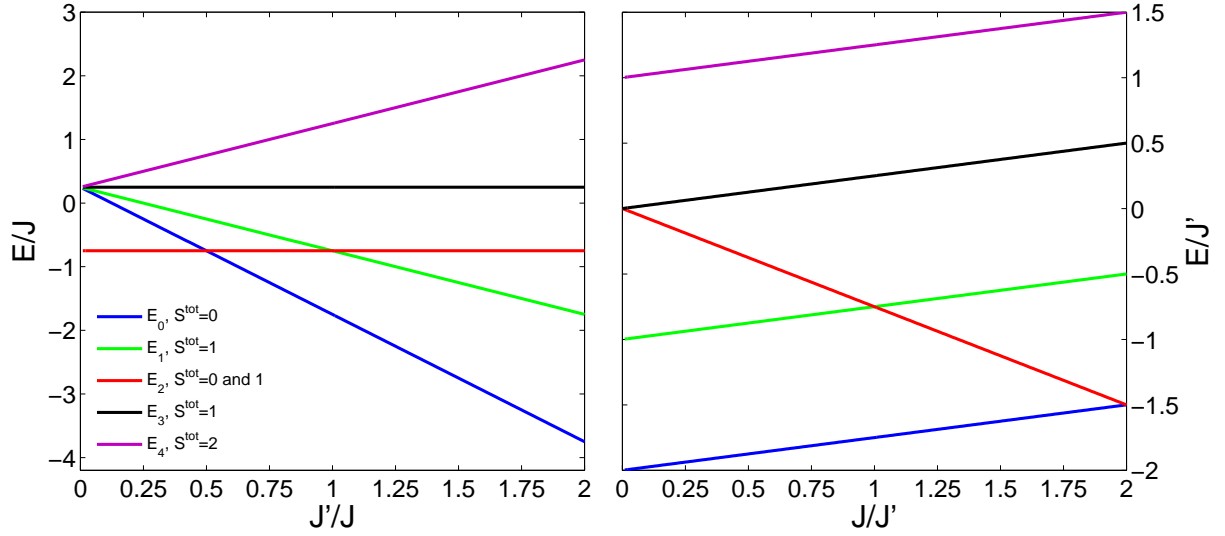


Figure B.2: Energy spectrum for the full plaquette. Left: As a function of  $J'/J$ . Right: as a function of  $J/J'$ . The void plaquette spectrum is obtained along the  $J/J'=0$  line on the right panel.

survive on the extended plaquette system [92] – and they are two low lying excited states that are observable by INS. The crossover between these two states is at  $J'/J=1$  for the isolated plaquette, but can turn out to be at very different values on the extended frustrated lattice. Our experimental evidence shows the lowest triplet has a structure factor peaking just above  $Q_h=1$  on the  $Q=(H,0,0)$  line, which is the case for the  $E_0 \rightarrow E_1$  transition discussed above. The second excited state at 21.5 kbar has the same structure factor than  $\Delta$  the ambient pressure gap. The  $E_0 \rightarrow E_2$  transition for the full plaquette shows exactly this behavior, while for the void plaquette  $S(\vec{Q})$  is different. We thus favor the interpretation that the new discovered phase in  $\text{SrCu}_2(\text{BO}_3)_2$  corresponds to the formation of a plaquette state on the plaquettes containing a diagonal bond.



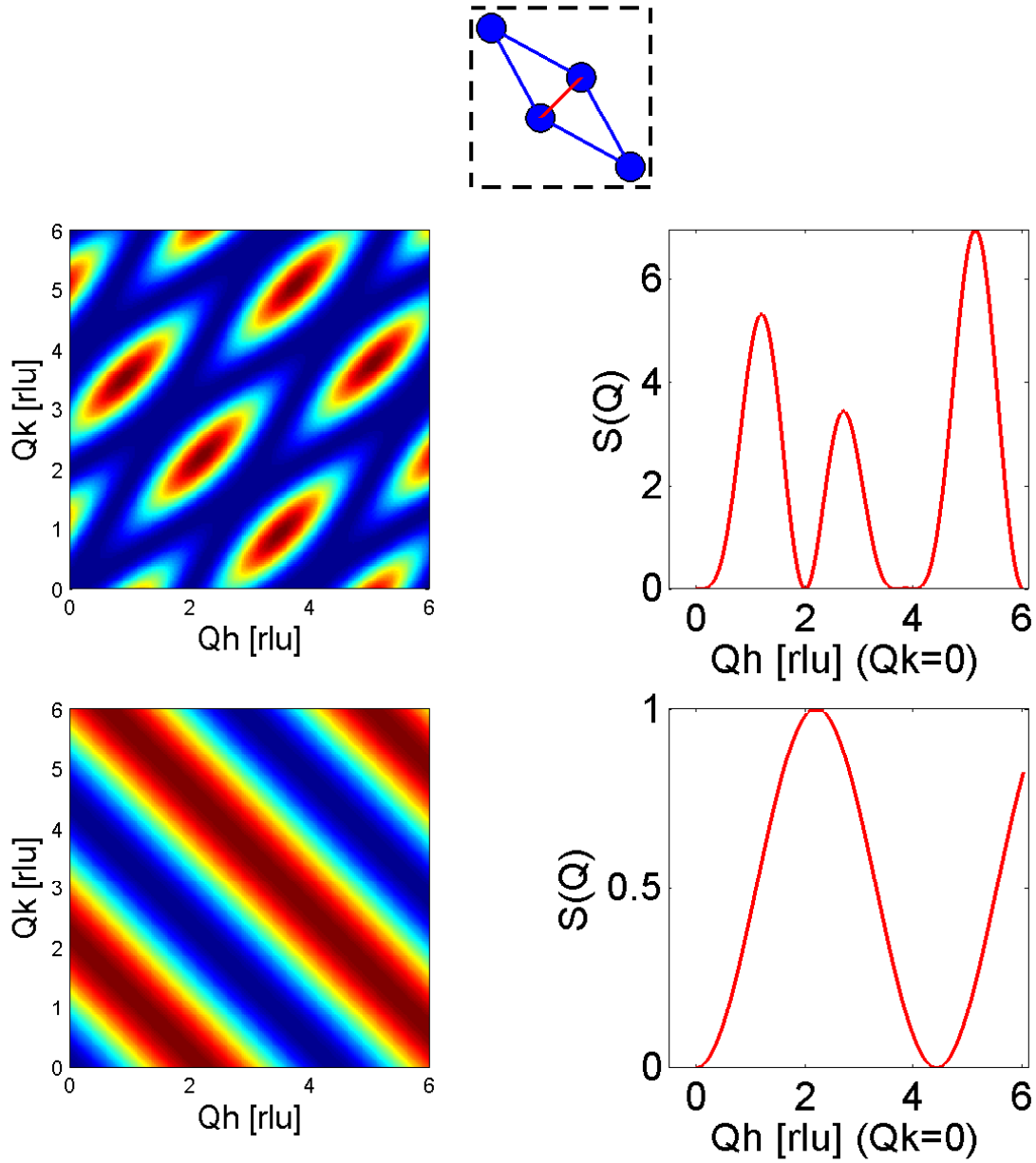


Figure B.3: Sum of the structure factors ( $S^{x,x} + S^{y,y} + S^{z,z}$ ) for one full plaquette orientation displayed on the upper panel. The middle panel shows the transition  $E_0 \rightarrow E_1$  and the lower panel the transition  $E_0 \rightarrow E_2$ . Intensity scale for the color map: low intensity in dark blue to high intensity in dark red.

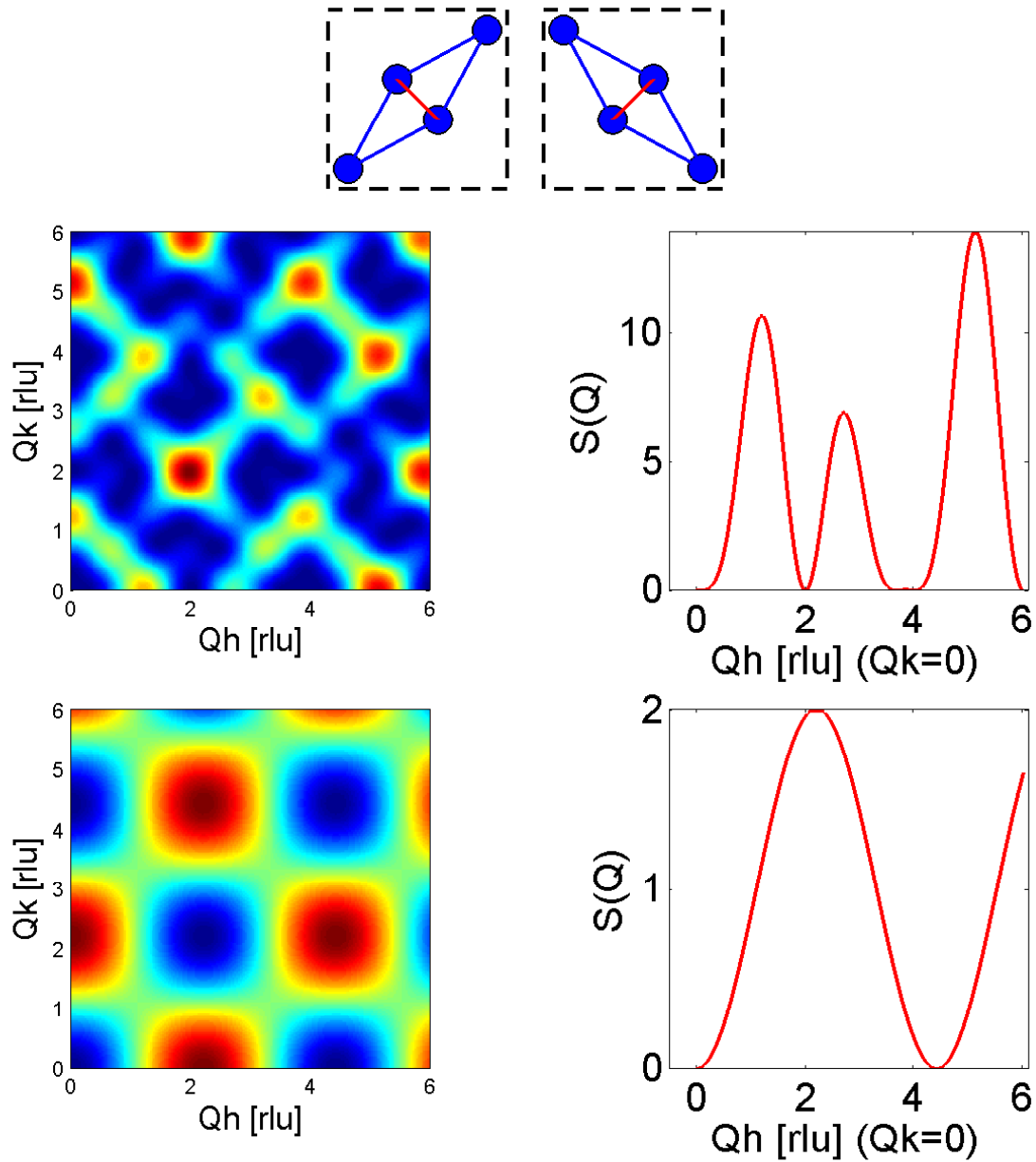


Figure B.4: Sum of the structure factors ( $S^{x,x} + S^{y,y} + S^{z,z}$ ) for the two orientations of full plaquettes displayed in the upper panel. The middle panel shows the transition  $E_0 \rightarrow E_1$  and the lower panel the transition  $E_0 \rightarrow E_2$ .

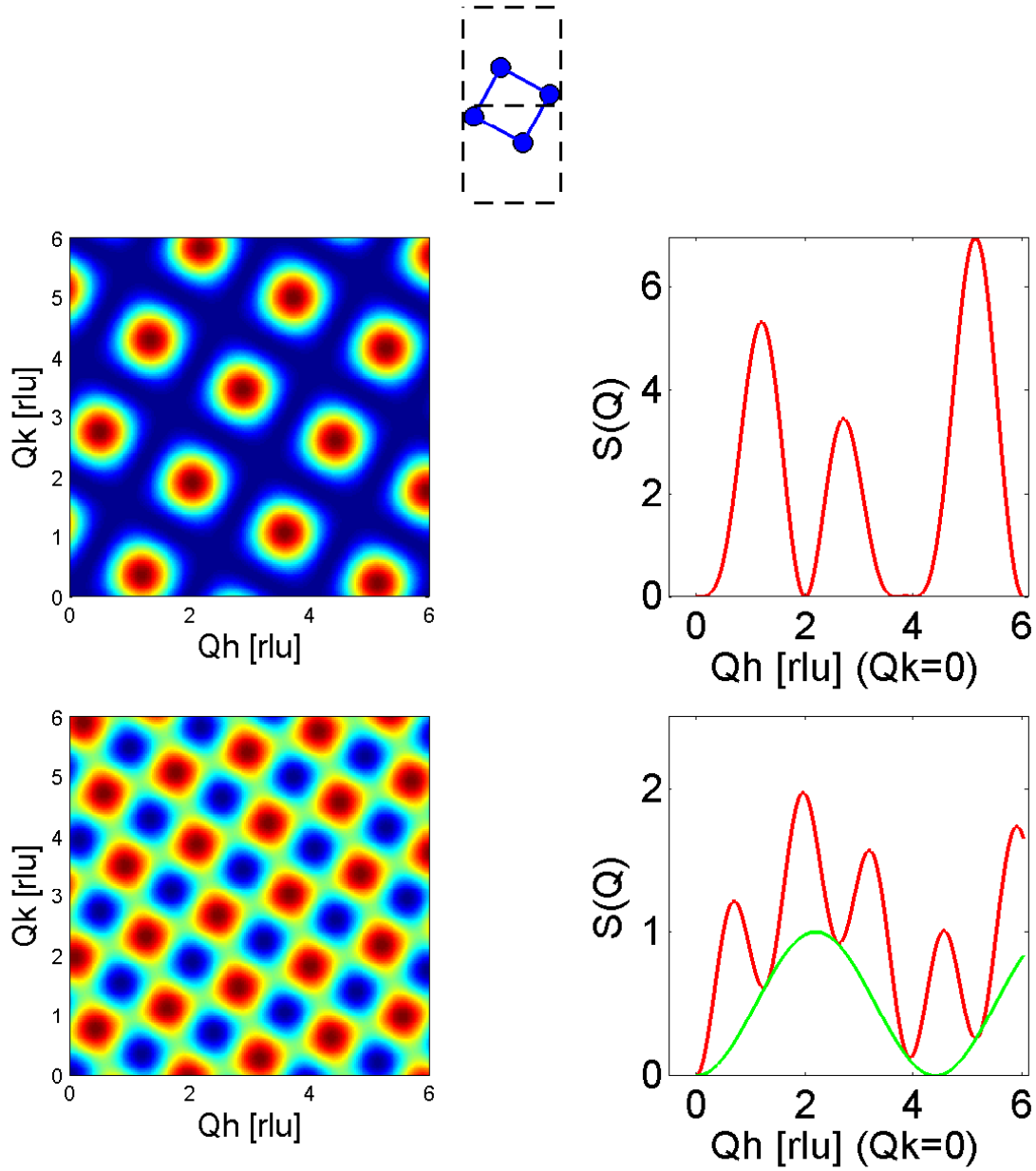


Figure B.5: Sum of the structure factors ( $S^{x,x} + S^{y,y} + S^{z,z}$ ) for one void plaquette orientation displayed in the upper panel. The middle panel shows the transition  $E_0 \rightarrow E_1$  and the lower panel the transition  $E_0 \rightarrow [E_2, E_3]$ . The green line is the dimer singlet-triplet structure factor (Eq.A.11).

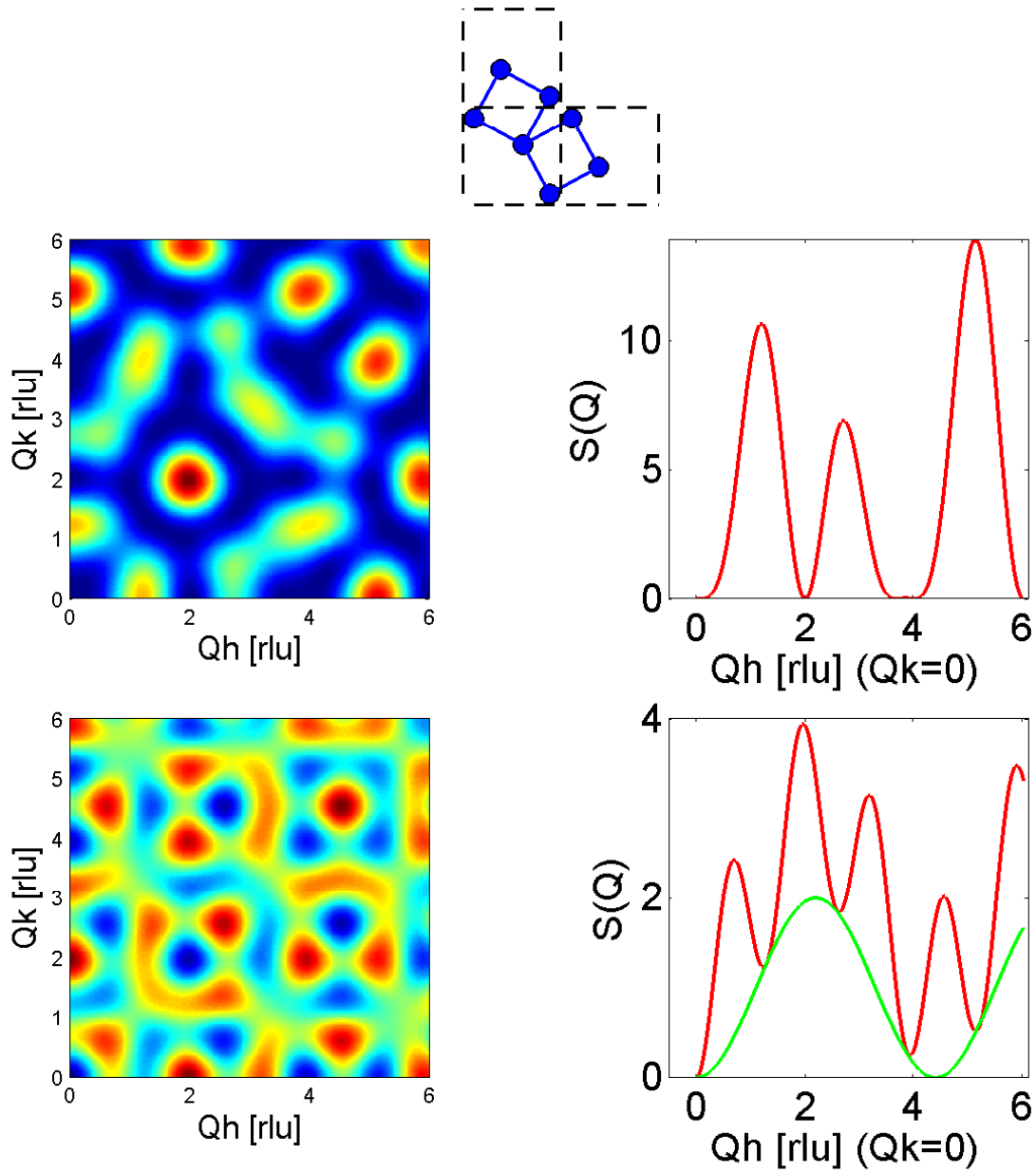
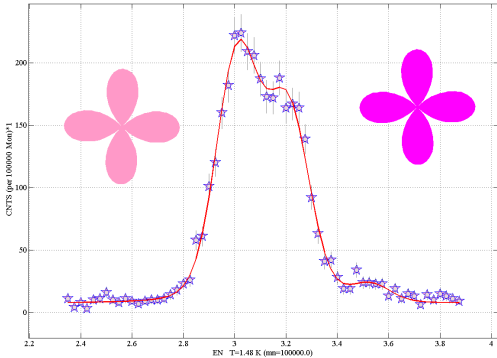


Figure B.6: Sum of the structure factors ( $S^{x,x} + S^{y,y} + S^{z,z}$ ) for the two orientations of void plaquettes displayed in the upper panel. The middle panel shows the transition  $E_0 \rightarrow E_1$  and the lower panel the transition  $E_0 \rightarrow [E_2, E_3]$ . The green line is the dimer singlet-triplet structure factor (Eq.A.11).

# Acknowledgement

First and starting in chronological order, I would like to thank Prof. Joel Mesot for giving me the opportunity to realize this thesis and to enter the world of neutron scattering. Then, of course, my supervisor Prof. Henrik Rønnow who has guided me through out this work from the beginning at the Laboratory for Neutron Scattering at PSI until the end at the Laboratory for Quantum Magnetism at EPFL. It is with him that I have learned the basics of neutron scattering and I profited a lot from his constant novel ideas. I am also grateful to Dr Christian Rüegg who has accompanied me to most of the experiments and has pushed this project forward. As with Henrik, I have learned a lot through his presence with me at the various neutron sources across Europe. I would also like to acknowledge Prof. Manfred Sigrist for accepting to take the official supervision of this doctoral work and his prompt help for in final steps. Then I would like to thank Katja Pomjakushina, Kazimierz Conder, and Marian Stingaciu for both them growing the  $\text{SrCu}_2(\text{BO}_3)_2$  crystals and their immense patience after we brake them in high pressure experiments, Thierry Strässle, Stefan Klotz and Gerard Hammel for all the support for high pressure equipment, all the instruments responsible and the technical teams at SINQ, ILL, FRM2, ESRF and LLB where I had the occasion to perform experiments. A thank to Volodja Pomjakushin who has helped me a lot for the analysis of the diffraction patterns and to Bastien Dalla Piazza and Jérôme Egger for their help with the Matlab code for the structure factor. I also thank all my colleagues during the time in Villigen and Lausanne Marc, Beni, Gelu, Kruno, Konradin, Yasmine, Julia, Nikolay, Gøran, Julian, Julio, Neda, Bastien, Saba, Martin with whom I have shared office, time, coffees, and more. Finally a thank to my family, my parents who have supported me all these year, my wife, my little princess and my little boy who was born during this PhD time, I am looking forward to having more



A fit directed by my little princess, a much nicer way to present data :).

time for you now that this work is over.

# Bibliography

- [1] U. Schollwöck, J. Richter, D. J. J. Farnell, and R. F. Bishop (Eds.), *Quantum Magnetism*, Vol. 645 (Springer-Verlag, Berlin, 2004)
- [2] J. Sadoc and R. Mosseri, *Geometrical Frustration* (Cambridge Univ. Press, UK, 1999)
- [3] J. Villain, R. Bidaux, J. P. Carton, and R. Conte, *J. Phys.* **41**, 1263 (1980)
- [4] C. Majumdar and D. Ghosh, *J. Math. Phys.* **10**, 1388 (1969)
- [5] B. S. Shastry and B. Sutherland, *Physica B* **108**, 1069 (1981)
- [6] A. Koga, *J. Phys. Soc. Japan* **69**, 3509 (2000)
- [7] S. Miyahara and K. Ueda, *J. Phys.: Condens. Matter* **15**, 327 (2003)
- [8] M. Albrecht and F. Mila, *Europhys. Lett.* **34**, 145 (1996)
- [9] S. Miyahara and K. Ueda, *Phys. Rev. Lett.* **82**, 3701 (1999)
- [10] Z. Weihong, J. Oitmaa, and C. J. Hamer, *Phys. Rev. B* **60**, 6608 (1999)
- [11] E. Müller-Hartmann, R. R. P. Singh, C. Knetter, and G. S. Uhrig, *Phys. Rev. Lett.* **84**, 1808 (2000)
- [12] A. Koga and N. Kawakami, *Phys. Rev. Lett.* **84**, 4461 (2000)
- [13] Z. Weihong, J. Oitmaa, and C. J. Hamer, *Phys. Rev. B* **65**, 014408 (2002)
- [14] A. Läuchli, S. Wessel, and M. Sigrist, *Phys. Rev. B* **66**, 014401 (2002)

- [15] K. Kodama, J. Yamazaki, M. Takigawa, H. Kageyama, K. Onizuka, and Y. Ueda, *J. Phys.: Condens. Matter* **14**, L319 (2002)
- [16] J. Dorier, K. P. Schmidt, and F. Mila, *Phys. Rev. Lett.* **101**, 250402 (2008)
- [17] G. Jorge, R. Stern, M. Jaime, N. Harrison, J. Bonea, S. El Shawish, C. D. Batista, H. A. Dabkowska, and B. D. Gaulin, *Phys. Rev. B* **71**, 092403 (2005)
- [18] T. Momoi and K. Totsuka, *Phys. Rev. B* **61**, 3231 (2000)
- [19] K. Schmidt, J. Dorier, A. Läuchli, and F. Mila, *Phys. Rev. Lett.* **100**, 090401 (2008)
- [20] B. S. Shastry and B. Kumar, *Prog. of Theor. Phys. Suppl.* **145**, 1 (2002)
- [21] T. Kimura, K. Kuroki, R. Arita, and H. Aoki, *Phys. Rev. B* **69**, 054501 (2004)
- [22] B. J. Yang, Y. B. Kim, J. Yu, and K. Park, *Phys. Rev. B* **77**, 104507 (2008)
- [23] H. Kageyama, K. Yoshimura, R. Stern, N. Mushnikov, K. Onizuka, M. Kato, K. Kosuge, C. Slichter, T. Goto, and Y. Ueda, *Phys. Rev. Lett.* **82**, 3168 (1999)
- [24] R. W. Smith and D. A. Keszler, *J. Solid State Chem.* **93**, 430 (1991)
- [25] K. Sparta, G. J. Redhammer, P. Roussel, G. Roth, P. Lemmens, A. Ionescu, M. Grove, G. Güntheodt, F. Hüning, H. Lueken, H. Kageyama, K. Onizuka, and Y. Ueda, *Eur. Phys. J.* **19**, 507 (2001)
- [26] C. Vecchini, O. Adamopoulos, L. C. Chapon, A. Lappas, H. Kageyama, Y. Ueda, and F. Zorko, *J. Solid State Chem.* **182**, 3275 (2009)
- [27] A. Lappas and F. Zorko, *ISIS Experimental Report* 15281(2004)
- [28] I. Loa, F. X. Zhang, K. Syassen, P. Lemmens, W. Crichton, H. Kageyama, and Y. Ueda, *Physica B* **359-361**, 980 (2005)
- [29] H. Kageyama, K. Onizuka, Y. Ueda, N. V. Mushnikov, T. Goto, K. Yoshimura, and K. Kosuge, *J. Phys. Soc. Japan* **67**, 4304 (1998)
- [30] H. Nojiri, H. Kageyama, K. Onizuka, Y. Ueda, and M. Motokawa, *J. Phys. Soc. Japan* **68**, 2906 (1999)



- [31] H. Nojiri, H. Kageyama, K. Onizuka, Y. Ueda, T. Asano, Y. Ajiro, and M. Motokawa, *J. Phys. Soc. Japan (Suppl.)* **69**, 2291 (2000)
- [32] H. Nojiri, H. Kageyama, Y. Ueda, T. Asano, and M. Motokawa, *J. Phys. Soc. Japan* **69**, 3243 (2003)
- [33] H. Kageyama, M. Nishi, N. Aso, K. Onizuka, T. Yosihama, K. Nukui, K. Kodama, K. Kakurai, and Y. Ueda, *Phys. Rev. Lett.* **84**, 5876 (2000)
- [34] B. D. Gaulin, S. H. Lee, S. Haravifard, J. P. Castellan, A. J. Berlinsky, H. A. Dabkowska, Y. Qiu, and J. R. D. Copley, *Phys. Rev. Lett.* **93**, 267202 (2004)
- [35] K. Kakurai, K. Nukui, N. Aso, M. Nishi, H. Kadowaki, H. Kageyama, Y. Ueda, L. P. Regnault, and O. Cepas, *Prog. Theor. Phys. Suppl.* **159**, 22 (2005)
- [36] A. Fukaya, Y. Fudamoto, I. M. Gat, T. Ito, M. I. Larkin, A. T. Savici, Y. J. Uemura, P. P. Kyriakou, G. M. Luke, M. T. Rovers, H. Kageyama, and Y. Ueda, *Physica B: Condensed Matter* **326**, 446 (2003)
- [37] A. Lappas, A. Schenck, and K. Prassides, *Physica B: Condensed Matter* **326**, 431 (2003)
- [38] H. Kageyama, H. Suzuki, M. Nohara, K. Onizuka, H. Takagi, and Y. Ueda, *Physica B* **281-282**, 667 (2000)
- [39] S. Zherlitsyn, S. Schmidt, B. Wolf, H. Schwenk, B. Luthi, H. Kageyama, K. Onizuka, Y. Ueda, and K. Ueda, *Phys. Rev. B* **62**, R6097 (2000)
- [40] B. Wolf, S. Zherlitsyn, S. Schmidt, B. Luthi, H. Kageyama, and Y. Ueda, *Phys. Rev. Lett.* **86**, 4847 (2001)
- [41] P. Lemmens, M. Grove, M. Fischer, G. Güntherodt, H. Kageyama, K. Onizuka, and Y. Ueda, *Physica B* **281-282**, 656 (2000)
- [42] P. Lemmens, M. Grove, M. Fischer, G. Güntherodt, V. N. Kotov, H. Kageyama, K. Onizuka, and Y. Ueda, *Phys. Rev. Lett.* **85**, 2605 (2000)

- [43] K. Kodama, M. Takigawa, M. Horvatic, C. Berthier, H. Kageyama, Y. Ueda, S. Miyahara, F. Becca, and F. Mila, *Science* **298**, 395 (2002)
- [44] T. Waki, Karai, M. Takigawa, Y. Saiga, Y. Uwatoko, H. Kageyama, and Y. Ueda, *J. Phys. Soc. Japan* **76**, 073710 (2007)
- [45] H. Kageyama in: *Frontiers in Magnetic Materials* (Springer, Heidelberg, 2005) p. 611. Ed. A. N. Narlikar
- [46] O. Cepas, K. Kakurai, L. P. Regnault, T. Ziman, J. P. Boucher, N. Aso, M. Nishi, H. Kageyama, and Y. Ueda, *Phys. Rev. Lett.* **87**, 167205 (2001)
- [47] Y. F. Cheng, O. Cépas, P. W. Leung, and T. Ziman, *Phys. Rev. B* **75**, 144422 (2007)
- [48] T. C. Ozawa, T. Taniguchi, Y. Kawaji, Y. Nagata, Y. Noro, H. Samata, and S. Takayanagi, *Physics Letters A* **337**, 130 (2005)
- [49] H. K. and Y. Ueda Y, Y. Narumi, K. Kindo, M. Kosaka, and Y. Uwatoko, *Prog. Theor. Phys. Suppl.* **145** (2002)
- [50] M. S. Kim, M. C. Bennett, and M. C. Aronson, *Phys. Rev. B* **77**, 144425 (2008)
- [51] S. Yoshii, T. Yamamoto, M. Hagiwara, T. Takeuchi, A. Shigekawa, S. Michimura, F. Iga, T. Takabatake, and K. Kindo, *J. Magn. Magn. Mater.* **310**, 1282 (2007)
- [52] A. Kikkawa, K. Katsumata, Y. Narumi, K. ichi Suga, T. Fukui, T. Sugaya, K. Kindo, F. Iga, and S. Michimura, *J. Phys. Soc. Japan* **76**, 024711 (2007)
- [53] R. Watanuki, H. Mitamura, T. Sakakibara, G. Sato, and K. Suzuki, *Physica B* **378-380**, 594 (2006)
- [54] S. Michimura, A. Shigekawa, F. Iga, M. Sera, T. Takabatake, K. Ohoyama, and Y. Okabe, *Physica B* **378-380**, 596 (2006)
- [55] S. Yoshii, T. Yamamoto, M. Hagiwara, A. Shigekawa, S. Michimura, F. Iga, T. Takabatake, and K. Kindo, *J. Phys.: Conf. Ser.* **51**, 59 (2006)
- [56] M. Moliner, D. C. Cabra, A. Honecker, P. Pujol, and F. Stauffer, *J. Phys.: Conf. Ser.* **145**, 012053 (2009)

- [57] <http://www.ill.eu/reactor-environment-safety/high-flux-reactor/technical-characteristics/>
- [58] <http://www.frm2.tum.de/en/technik/reactor/neutron-flux-density/index.html>
- [59] <http://sinq.web.psi.ch/>
- [60] <http://www.ill.eu/instruments-support/instruments-groups/instruments/in14/characteristics/>
- [61] <http://www.ill.eu/instruments-support/instruments-groups/instruments/in8/characteristics/>
- [62] G. L. Squires, *Introduction to the Theory of Thermal Neutron Scattering* (Dover Publications, 1997)
- [63] S. W. Lovesey, *Theory of Neutron Scattering from Condensed Matter*, International Series of Monographs on Physics, Vol. 72 (Oxford Science Publications, 1984 reprinted 2003)
- [64] A. Furrer, J. Mesot, and T. Strässle, *Neutron Scattering in Condensed Matter Physics*, Series on Neutron Techniques and Applications, Vol. 4 (World Scientific Publishing, 2009)
- [65] ILL neutrons for Science, A J Dianoux and G Lander (Eds.), *Neutron Data Booklet, Second Edition* (Old City Publishing, 2003)
- [66] S. Haravifard, S. R. Dunsiger, S. El Shawish, B. D. Gaulin, H. A. Dabkowska, M. T. F. Telling, T. G. Perring, and J. Bonča, *Phys. Rev. Lett.* **97**, 247206 (2006)
- [67] R. Norrestam, S. Carlson, and A. Sjödin, *Acta Cryst.* **C50**, 1847 (1994)
- [68] P. W. Bridgman, *The Physics of High Pressure* (Bell, London, 1931)
- [69] P. F. McMillan, *Nature Materials* **4**, 715 (2005)
- [70] I. F. Bailey, *Z. Kristallogr.* **218**, 84 (2003)
- [71] S. Klotz, *Z. Kristallogr.* **216**, 420 (2001)
- [72] A. Jayaraman, *Rev. Sci. Instrum.* **57**, 1013 (1986)

- [73] J. Kohlbrecher, A. Bollhalder, R. Vavrin, and G. Meier, *Rev. Sci. Instrum.* **78**, 125101 (2007)
- [74] W. F. Kuhs, E. Hensel, and H. Bartels, *J. Phys.: Condens. Matter* **17**, S3009 (2005)
- [75] M. Zayed, Ch. Rüegg, H. M. Rønnow, E. Pomjakushina, M. Stingaciu, K. Conder, J. Stahn, T. Strässle, D. McMorrow, and J. Mesot, *SINQ Experimental Report* 20050341(2005)
- [76] N. Aso, Y. Uwatoko, T. Fujiwara, G. Motoyama, S. Ban, Y. Homma, Y. Shiokawa, K. Hirota, and N. K. Sato, *AIP Conf. Proc. (LOW TEMPERATURE PHYSICS: 24th International Conference on Low Temperature Physics - LT24)* **850**, 705 (2006)
- [77] N. Aso, T. Fujiwar, Y. Uwatoko, H. Miyano, and H. Yoshizawa, *J. Phys. Soc. Japan (Suppl. A)* **76**, 228 (2008)
- [78] D. B. McWhan, D. Bloch, and G. Parisot, *Rev. Sci. Instrum.* **45**, 643 (1974)
- [79] W. Utsumi, H. Kagi, K. Komatsu, H. Arima, T. Nagai, T. Okuchi, T. Kamiyama, Y. Uwatoko, K. Matsubayashi, and T. Yagi, *Nuclear Instruments and Methods in Physics Research Section A: Accelerators, Spectrometers, Detectors and Associated Equipment* **600**, 50 (2009)
- [80] J. Abe, M. Arakawa, T. Hattori, H. Arima, H. Kagi, K. Komatsu, A. Sano-Furukawa, Y. Uwatoko, K. Matsubayashi, S. Harjo, A. Moriai, T. Ito, K. Aizawa, M. Arai, and W. Utsumi, *Rev. Sci. Instrum.* **81**, 043910 (2010)
- [81] I. N. Goncharenko, *High Pressure Research* **24**, 193 (2004)
- [82] I. N. Goncharenko, *High Pressure Research* **27**, 183 (2007)
- [83] V. A. Sidorov and R. A. Sadykov, *J. Phys.: Condens. Matter* **17**, S3005 (2005)
- [84] Private communication by the company 3M producing Fluorinert<sup>TM</sup>
- [85] C. L. Bull, M. Guthrie, S. Klotz, J. Philippe, T. Strässle, J. Richard, Nelmes, J. S. Loveday, and G. Hamel, *High Pressure Research* **25**, 229 (2005)

- [86] S. E. Shawish, J. Bonča, and I. Sega, Phys. Rev. B **72**, 184409 (2005)
- [87] B. Fåk and B. Dorner, Physica B **234-236**, 1107 (1997)
- [88] H. M. Rønnow, L. P. Regnault, K. Kakurai, and A. Stunault, ILL Experimental Report 4-03-1431(2004)
- [89] N. Aso, H. Kageyama, K. Nukui, M. Nishi, H. Kadowaki, Y. Ueda, and K. Kakurai, J. Phys. Soc. Japan **74**, 2189 (2005)
- [90] K. Kakurai, N. Aso, K. Nukui, M. Nishi, H. Kageyama, Y. Ueda, H. Kadowaki, and O. Cepas, in *Quantum Properties of Low-Dimensional antiferromagnets (Proc. of French-Japanese Symposium)*, edited by Y. Aijiro and J. P. Boucher (Kyushu University Press, 2001)
- [91] V. F. Correa, M. Jaime, N. Harrison, C. Batista, G. Jorge, R. Stern, J. Bonca, S. E. Shawish, H. A. Dabkowska, and B. Gaulin, National High Magnetic Field Laboratory Research Report(2004)
- [92] Y. Takushima, A. Koga, and N. Kawakami, J. Phys. Soc. Japan **70**, 1369 (2001)
- [93] M. A. Hajj and J. P. Malrieu, Phys. Rev. B **72**, 094436 (2005)
- [94] H. Kageyama, N. V. Mushnikov, M. Yamada, and Y. U. T Goto, Physica B **329-333**, 1020 (2003)
- [95] T. Sakurai, M. Tomoo, S. Okubo, H. Ohta, K. Kudo, and Y. Koike, J. Phys.: Conf. Ser. **150**, 042171 (2009)
- [96] C. Knetter, A. Buhler, E. Müller-Hartmann, and G. S. Uhrig, Phys. Rev. Lett. **85**, 3958 (2000)
- [97] A. Ralko, D. Poilblanc, and R. Moessner, Phys. Rev. Lett. **100**, 037201 (2008)
- [98] "FULLPROF: A Program for Rietveld Refinement and Pattern Matching Analysis", by J. Rodriguez-Carvajal, at the Satellite Meeting on Powder Diffraction of the XV IUCr Congress, 127 (1990)

- [99] P. W. Anderson, Mater. Res. Bull. **8**, 153 (1973)
- [100] B. Bernu, C. Lhuillier, and L. Pierre, Phys. Rev. Lett. **69**, 2590 (1992)
- [101] J. T. Haraldsen, T. Barnes, and J. L. Musfeldt, Phys. Rev. B **71**, 064403 (1991)
- [102] A. Koga, K. Okunishi, and N. Kawakami, Phys. Rev. B **62**, 5558 (2000)

# Curriculum Vitae

Name : Mohamed Zayed

Date of birth: 22.06.1974

Nationality: Swiss and Egyptian

1989-1993 High school: Gymnase Français de Bienne

Diploma: Maturité scientifique (1993)

1993-1999 University: École polytechnique fédérale de Lausanne (EPFL), diploma work at EPFL and King's College London

Diploma: Diplôme d'ingénieur physicien (1999)

2005-2010: Phd student at ETH Zurich affiliated to the Laboratory of Neutron Scattering at the Paul Scherrer Institute in Villigen and the Laboratory for Quantum Magnetism at EPFL Lausanne

Professional experience

1999 Federal office of Metrology Wabern

2000-2001 Sunrise

2001-2005 Consulting

2005 University of Fribourg